Optimizing Optical-sectioning Microscopy Techniques for Diverse Biomedical Applications

Ye Chen

A dissertation

submitted in partial fulfillment of the

requirements for the degree of

Doctor of Philosophy

University of Washington

2019

Reading Committee:

Jonathan T.C. Liu, Chair

Eric J. Seibel

Joshua C. Vaughan

Program Authorized to Offer Degree:
Mechanical Engineering

University of Washington

Abstract

Optimizing Optical-sectioning Microscopy Techniques for Diverse Biomedical Applications

Ye Chen

Chair of the Supervisory Committee:
Jonathan T.C. Liu
Mechanical Engineering

Optical-sectioning microscopes are powerful tools that can be used by biomedical scientists and clinicians to visualize and monitor subcellular features in thick tissues at relatively large depths (up to hundreds of microns). In clinical settings, such technologies could play a transformative role in detecting early-stage cancer and guiding the surgical resection of tumors. This dissertation focuses on optimizing optical-sectioning microscopes that utilize off-axis illumination and collection architectures to spatially filter out-of-focus and multiply-scattered photons. In particular, we will focus on overcoming certain challenges with using dual-axis confocal (DAC) microscopy and light-sheet microscopy to image biological specimens, such as mitigating resolution degradation caused by refractive heterogeneities within tissues and achieving rapid microscopic pathology of large clinical specimens. In the case of DAC microscopy, tissue-imaging performance is highly sensitive to the effects of refractive-index heterogeneities within biological

specimens, which cause beam steering and distortion artifacts that lead to misalignment of the off-axis illumination and collection beam paths of a DAC microscope. Since the propagation-invariant and self-reconstructing features of Bessel beams have been shown to benefit microscopy of specimens with refractive heterogeneities, Bessel-beam illumination has been explored as a means to alleviate resolution degradation that occurs when performing tissue-imaging with DAC microscopy. Results indicate that DAC microscopy with Bessel illumination exhibits reduced resolution degradation from microscopic tissue heterogeneities compared to DAC microscopy with conventional Gaussian illumination. In the context of light-sheet microscopy, an open-top light-sheet (OTLS) microscope along with a novel fluorescent analog of hematoxylin and eosin (H&E) staining, has been developed and optimized for robust intraoperative pathology of lumpectomy margins. OTLS images of the surfaces of fresh breast samples were compared to gold-standard H&E histological images to showcase that the image quality of OTLS microscopy can approximate that of archival H&E histology of formalin-fixed paraffin-embedded tissues. In addition, preliminary results suggest that OTLS microscopy is compatible with downstream archival H&E histology and immunohistochemistry (IHC) analyses, which are currently relied upon for definitive clinical diagnoses. These results facilitate the clinical translation of OTLS microscopy for intraoperative guidance of breast conserving surgery as well as other surgical oncology procedures.

TABLE OF CONTENTS

LIST OF FIGURES

LIST OF TABLES

ACKNOWLEDGEMENTS

In September 2009, I started the journey of studying in the United States. Over the past 10 years, I have received many encouragement, support, guidance, assistance and suggestions from a group of people who raised me from a freshman striving for English fluency to a doctoral candidate pursuing professional development. I feel great pleasure in expressing my profound and sincere gratitude to everyone.

First and foremost, I would like to thank my advisor, Professor Jonathan Liu, for his reply to an email I sent in 2011, offering me the opportunity to learn and work in the Molecular Biophotonics Lab. I am grateful for the time and patience he devoted to carefully correcting my English writing, helping me overcome challenges, and training me to become a better independent thinker. It would not have been possible to complete the entire dissertation research without his support and guidance.

I would also like to thank my dissertation committee members: Professor Joshua Vaughan, Professor Eric Seibel, and Professor Ruikang Wang, for their valuable comments and suggestions, which have significantly improved this dissertation.

From the east coast to the west coast, I have grown up along with the Molecular Biophotonics Lab. I want to thank our previous and current lab members for their support and enthusiasm, which have made every moment joyful while working in the lab. In particular, I am grateful for Dr. Danni Wang and Dr. Steven Leigh, who have always been great mentors inside/outside of the lab and have remained as precious friends of mine. In addition, I am thankful to Dr. Adam Glaser, Dr. Nicholas Reder and Dr. Suzanne Dintzis (University of Washington

School of Medicine, Department of Pathology) for providing professional insights and discussions at various stages of the light-sheet microscopy project.

Besides, I would like to express my sincerest appreciation to Northwest BioSpecimen, the tissue resource center at the University of Washington, and a special group of people - they were the patients who consented tissue donation for our research. Their support is vital for us to strive towards one goal, which is to make a difference in the lives of countless individuals in the future.

Last but certainly not least, I am extremely grateful for my wonderful friends and my beloved family. They have always been the ones who keep me going when facing all the challenges. I want to thank my parents and grandpa for their love and encouragement. I hope I have made them proud. Finally, I am grateful to have found my dear husband, Hannan. His patience, trust, respect, support and love mean everything to me. I look forward to many more great days, years and decades to come with him.

Chapter 1. INTRODUCTION: THE CHALLENGES FACING LIGHT MICROSCOPY OF BIOLOGICAL TISSUES

When performing microscopy of biological tissues, there is a common trade-off between imaging depth and spatial resolution (**Figure 1.1**) [1]. In general, the ability to image deep within tissues necessitates the sacrifice of spatial resolution. Depending on a particular microscopy application, the designs of different optical imaging systems, such as confocal microscopy [2-8], nonlinear microscopy [9-11], selective plane illumination microscopy (SPIM) [12, 13], structured-illumination microscopy (SIM) [14, 15], optical coherence tomography (OCT) [16, 17], strive to balance resolution, contrast, speed, cost as well as other performance features.

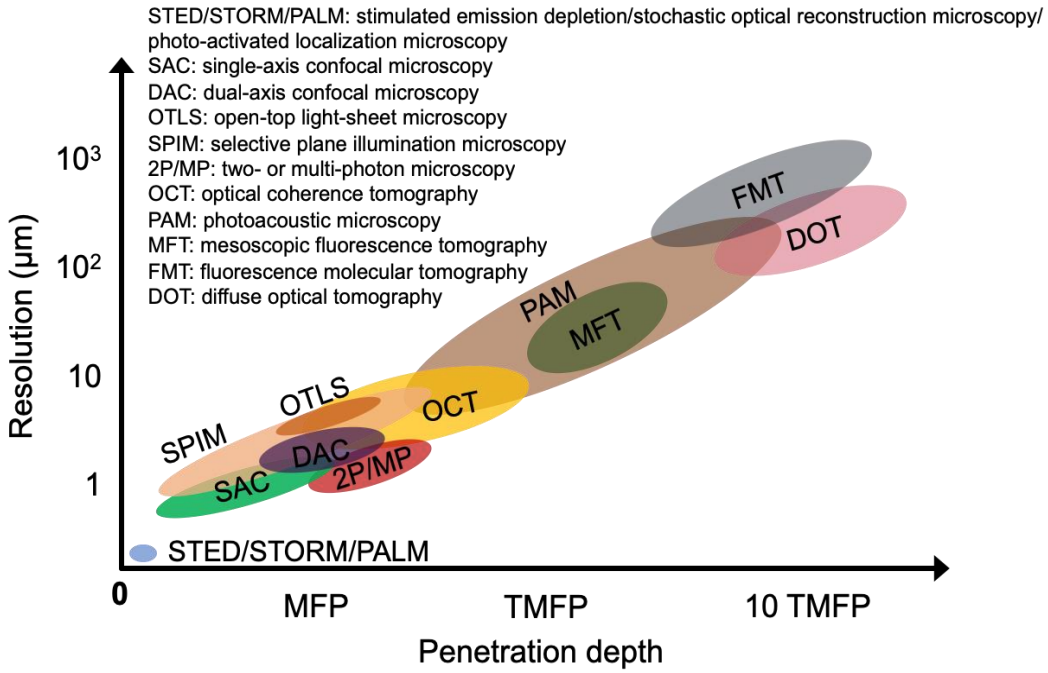

Figure 1.1. The trade-off between imaging depth and spatial resolution in different optical imaging modalities, modified from Ntziachristos in *Nature Methods* 2010 [1]. The approximate ranges on imaging depth and resolution are plotted for stimulated emission depletion microscopy (STED), stochastic optical reconstruction microscopy (STORM), photo-activated localization microscopy (PALM), single-axis confocal microscopy (SAC), dual-axis confocal microscopy (DAC), open-top light-sheet microscopy (OTLS), selective plane illumination microscopy (SPIM), two- or multi-photon microscopy, optical coherence tomography (OCT), photoacoustic microscopy (PAM), mesoscopic fluorescence tomography (MFT), fluorescence molecular tomography (FMT), diffuse optical tomography (DOT).

Over the past decades, many different novel optical imaging techniques have been developed to push microscopy beyond conventional limits. In the case of resolution enhancement, super resolution microscopy techniques, such as stimulated emission depletion (STED) [18], photo-activated localization microscopy (PALM) [19] and stochastic optical reconstruction microscopy (STORM) [20], achieve highly localized signal by focusing efforts on the manipulation of excitation light pattern [18] or on the development of photoswitchable fluorescent probes [19, 20]. In addition, laser beam shaping techniques, such as sectioned-Bessel illumination [21], Airy beam illumination [22] or Lattice illumination [23] have been implemented with SPIM to accomplish high resolution microscopy while minimizing the background from out-of-focus excitation.

On the other hand, various approaches have been developed to optimize image contrast in optical microscopy, which are beneficial for applications where the imaging depth is of primary concern. For example, two-or multi-photon microscopy exploits nonlinear excitation to generate a confined focal volume with minimal out-of-focus and multiply-scattered background signal [9-11], which thereby enables a larger depth of imaging in thick specimens. Recently, there has been growing interest in exploring the use of tissue-clearing techniques [24-26] to enhance the optical transparency of biological samples. By homogenizing the refractive-index heterogeneities within tissues, optical clearing approaches have shown promise for performing deep-tissue imaging of large specimens.

This dissertation focuses on optimizing optical-sectioning microscopes that utilize off-axis illumination and collection configurations to spatially reject out-of-focus and multiply-scattered photons, such as dual-axis confocal (DAC) microscopy and light-sheet microscopy (LSM). In particular, we seek to overcome certain challenges facing laser-scanning microscopy of biological

samples. This chapter describes two of these challenges, which are 1) mitigating resolution degradation caused by refractive index variations within tissues and 2) achieving rapid microscopic pathology of lumpectomy specimens. The entire dissertation consists of three independent studies. First (Chapter 2), Monte-Carlo simulations have been utilized to evaluate the performance trade-offs of different confocal microscope configurations, providing a benchmark for designing miniature confocal microscopes for *in vivo* imaging applications, such as oral cancer detection and guiding brain tumor resection. Second (Chapter 3), Bessel-beam illumination, which shows better positional stability and beam quality than Gaussian-beam illumination when propagating through tissues, has been utilized in a point-scanned DAC microscope for high resolution imaging of biological samples. Third (Chapter 4), an open-top light-sheet (OTLS) microscope, along with a novel fluorescent analog of H&E staining, has been developed and optimized for comprehensive microscopic investigation of fresh, unfixed surgically excised breast tissues. In the end, Chapter 5 provides discussions of these studies and lists the opportunities for future improvements.

1.1 TISSUE-HETEROGENEITY-INDUCED RESOLUTION DEGRADATION

When performing laser-scanning microscopy of biological specimens, the image resolution and contrast are often hampered by refractive index variations within the whole sample. Biological tissues are mostly composed of water, proteins, lipids as well as other biomolecules [27]. These cellular and subcellular components have various refractive indices, which perturb the light-tissue interactions. **Table 1.1** has listed the absolute refractive indices of various common organic and inorganic components within biological tissues [28]. For example, collagen has a considerably high refractive index of ~ 1.55 [28]; cytoplasm has a refractive index of ~ 1.35 [28], which is close

to the refractive index of water (~ 1.33); and lipids have a refractive index of ~ 1.48, which is higher than the surrounding cytoplasm [28]. As light travels through tissues, scattering is introduced by the discontinuities in refractive index [29]. In addition to scattering, when performing microscopy of large specimens or organs, the refractive-index variations existing among different tissue types, for example, epithelial tissue and smooth muscle tissue, or among different micro-architectural structures, such as glands and vasculature, can cause spatial changes of the beam foci in terms of position (beam steering) and shape (aberrations / distortions) [30]. These light beam artifacts and distortions are likely to deteriorate the image resolution of laser-scanned microscopes designed to interrogate cellular and subcellular structures in thick tissues at a large depth [30]. **Table 1.2** has shown the refractive indices of several commonly imaged biological tissues and organs [31]. Previous studies have observed a significant degradation in spatial resolution when performing light microscopy of human skin tissues with sub-cellular resolution [32, 33].

Table 1.1. The refractive indices of various organic and inorganic components common to biological tissues [28].

	Absolute refractive index	Reference
Calcite	1.57	CRC Handbook of Chemistry and Physics
Quartz	1.55	CRC Handbook of Chemistry and Physics
Cell membrane	1.46–1.60	Quinby-Hunt & Hunt (1988)
Cell membrane	1.46–1.54	Meyer (1979)
Collagen	1.55	Chapman (1976)
Cytoplasm	1.35	Charney & Brackett (1961)
Lipids	1.48	Beuthan *et al.* (1996)
Silica	1.39–1.42	Aas (1981)
Mitochondria	1.40	Beuthan *et al.* (1996)

Amongst different microscopy modalities, Chapter 2 in this dissertation describes dual-axis confocal microscopy, in which tissue-imaging performance is highly sensitive to positional changes and distortions of the off-axis illumination and collection beams, making it susceptible to

the effects of refractive heterogeneities [34]. To overcome this limitation, we have explored the use of Bessel-beam illumination to mitigate tissue-heterogeneity-induced resolution degradation (Chapter 3) [30, 34]. The diffraction-free and self-reconstructing characteristics of Bessel beams have been shown to benefit optical microscopy of specimens with refractive heterogeneities in different studies [30, 35-39]. Results have indicated that Bessel beams maintain better pointing accuracy and beam quality than Gaussian beams when propagating within tissues [30]. Therefore, Bessel beams can be conducive to preserve resolution in DAC microscopy [34].

Table 1.2. The refractive indices of commonly imaged organs and tissues [31].

Organ/Tissue	R. I.	Magnified Scale
Spleen —	1.443 + .002	443
Liver	1.448 + .002	448
Kidney :		
Cortex —	1.444 + .002	444
Medulla	1.438 + .002	438
Pancreas	1.435 + .002	435
Intestinal wall	1.436 + .002	436
Fat	1.472 + .002	472
Bone	1.556 + .002	556
Cartilage	1.492 + .002	492
Muscle	1.431 + .002	431
Lung	1.342 + .002	342
Gall bladder wall	1.35 + .002	35
Blood (uncoagulated)		
Serum	1.33	33
Formed elements	1.432 + .003	432
Coagulated blood	1.465 + .003	465
Gray matter	1.395 + .002	395
White matter	1.467 + .002	467
Cerebellum	1.470 + .002	470

1.2 INTRAOPERATIVE GUIDANCE OF LUMPECTOMY

Another challenge facing many optical imaging techniques is to provide intraoperative guidance of different surgical oncology procedures. For example, substantial amounts of efforts have focused on advancing optical imaging for guiding breast cancer lumpectomy [6, 16, 40-46].

For the ~ 200,000 women who are diagnosed with early-stage invasive breast cancer or carcinoma *in situ* each year in the United States, breast-conserving surgery (BCS, a.k.a. partial

mastectomy or lumpectomy) has replaced whole-breast mastectomy as the preferred form of surgical intervention [47, 48]. Numerous clinical studies have shown that there is no difference in overall survival or disease-free survival between patients treated with mastectomy vs. BCS with postoperative radiation when complete tumor resection is achieved [49, 50]. However, a significant challenge for BCS is to ensure that tumors are completely resected, as this is highly correlated with the rate of local recurrence [51, 52]. Unfortunately, recent studies have reported that 20-40% of lumpectomy patients require additional surgery if post-operative pathology reveals that the resection margins are "positive" for tumor [53-55]. Re-excision surgeries are often uncomfortable and expensive for patients [53-55]. In addition, these surgeries may cause delayed initiation of adjuvant therapies with inferior patient outcomes [53-55].

In the past, studies have generally defined the resection margins as "positive" when tumor has been found at the inked surface [51, 56-58], "close" when tumor has been found within 1 to 3 mm of the inked surface of the specimen [51, 56-58], and "negative" when no tumor has been found within a "safe distance" (e.g. between 1 and 3 mm) from the inked surface [51, 56-58]. If tumor has been spotted within the 1- to 3-mm "safety margin", patients were often subjected to re-excision surgeries [53-55].

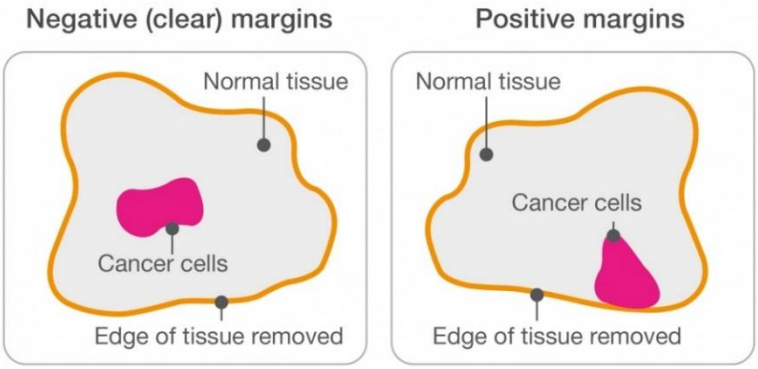

Figure 1.2. The difference between positive and negative lumpectomy margins, adopted from www.breastcancercare.org.uk. In 2014, the Society of Surgical Oncology (SSO) and the American Society for Radiation Oncology (ASTRO) published consensus guideline on margins for breast-conserving surgery with whole-breast irradiation, which defined negative margins as "no ink on tumor" [59].

In 2014, the Society of Surgical Oncology (SSO) and the American Society for Radiation Oncology (ASTRO) published consensus guideline on margins for BCS with whole-breast irradiation, which defined negative margins as "no ink on tumor" (**Figure 1.2**) [59]. Recent studies have shown that using conservative criteria (e.g. the 1- to 3-mm "safety distance") for margin evaluation does not significantly reduce local recurrence compared with "no ink on tumor" [59-64]. This indicates a superficial imaging approach (such as the OTLS microscopy described in Chapter 4) may provide the same level of improvement in decreasing the re-excision rate for lumpectomy in comparison to a depth-resolved imaging approach.

Chapter 4 in this dissertation discusses the current solutions for guiding lumpectomy, including slide-based histology [65-69], which has served as the "gold standard" for disease diagnosis over the past century, as well as other alternative technologies that have been in different stages of research development or clinical acceptance, such as frozen section histology [53, 70, 71], touch preparation cytology [72, 73], ultrasound [74-76], specimen radiography [77, 78], radiofrequency spectroscopy [79, 80], and intraoperative microscopy [6, 16, 40-45, 81]. To address some of the technical limitations encountered by these current approaches (e.g. limited surface sampling, spatial resolution and contrast), an OTLS microscope along with a robust fluorescent analog of H&E staining, has been developed and optimized for rapid and comprehensive surface imaging of lumpectomy margins (Chapter 4) [81]. An image atlas comparison with conventional H&E histology has been presented to showcase that the OTLS technique provides surface images that surpass the quality of frozen sectioning and approximate the quality of gold-standard histopathology [81]. Further, preliminary results have suggested that the OTLS staining and imaging methods were reconcilable with downstream archival H&E histology and IHC data [81], which can catalyze the clinical adoption of OTLS microscopy for surgical guidance.

Chapter 2. CHARACTERING AND OPTIMIZING THE IMAGING PERFORMANCE OF CONFOCAL MICROSCOPES VIA MONTE-CARLO SCATTERING SIMULATIONS

2.1 SINGLE-AXIS CONFOCAL (SAC) VS. DUAL-AXIS CONFOCAL (DAC) MICROSCOPES

The basic principle of confocal microscopy is to selectively collect the photons originating from a localized focal volume while minimizing the collection of background signals from out-of-focus regions [82, 83]. A typical approach to obtain a confocal image is by scanning the focal volume in two dimensions over a sample and constructing an image point-by-point. Confocal microscopy utilizes point illumination and pinhole detection to efficiently reject out-of-focus and multiply-scattered photons, providing superior tissue-imaging performance than conventional wide-field microscopy [82, 83]. As a non-destructive optical imaging technique, instead of physically sectioning the tissues, confocal microscopy obtains consecutive thin optical slices from thick specimens through spatially filtering undesirable background signals at each focal plane [82, 83]. These “optical biopsies” introduce minimal disruption of native tissue architecture and display similar structural information that can be obtained from traditional physical biopsies [82, 83].

A conventional confocal microscope is generally designed to image cellular or subcellular features within tissues, which requires a spatial resolution of a few microns. Typically, a bulky objective lens with a high numerical aperture (NA) is necessary to obtain high image resolution. Unfortunately, high-NA optics often lead to limited working distances due to geometric constraints, which introduces several limitations for *in vivo* imaging applications, such as oral cancer detection & guiding brain tumor resection. For example, the scanning mechanism (e.g.

mirror) must be positioned prior to the objective lens [84, 85]. Pre-objective beam scanning can cause off-axis aberrations that must be alleviated using multiple corrective lenses, which increases the size of the objective as well as the complexity of the optics [84, 85]. Further, since the illumination and collection beams travel a common path in a conventional confocal microscope, the photons scattered along the illumination path outside of the focal volume, indicated by the blue region in **Figure 2.1 (a)**, have a high probability to be fully collected as background signals by the same high-NA objective. These background signals decrease the imaging contrast (signal-to-background ratio, SBR) and limit the maximum-achievable imaging depth.

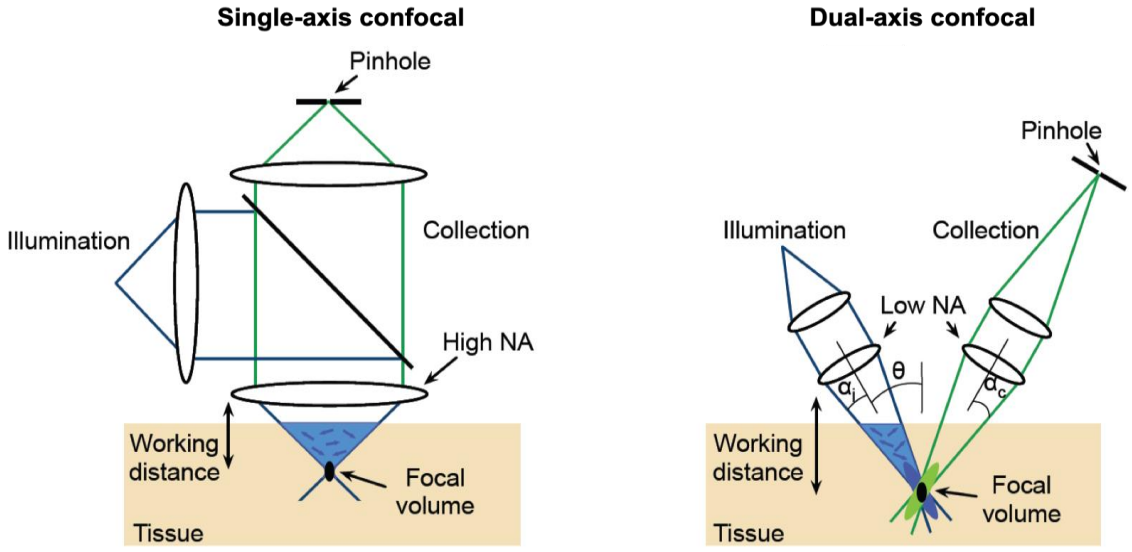

Figure 2.1. Schematic of single-axis vs. dual-axis microscope architectures. (a) The conventional single-axis configuration utilizes a single high-NA objective to illuminate and collect signals from a well-localized focal volume within scattering tissues. Some out-of-focus background is unavoidable due to this common-path arrangement. In addition, the short working distance of the high-NA objective necessitates pre-objective beam scanning, which introduces off-axis aberrations that must be compensated for. (b) The dual-axis configuration utilizes two low-NA beams for illumination and collection. Spatial separation of the beam paths enables high-contrast imaging with minimal out-of-focus background. The use of low-NA optics provides a long working distance, which allows for post-objective beam scanning with minimal off-axis aberrations when performing laser-scanning microscopy over a large field of view. This figure was published in [86].

In a DAC architecture, as shown in **Figure 2.1 (b)**, two low-NA beams are positioned such that they only intersect at their tiny foci with a crossing angle 2θ. The point spread function (PSF) of the low-NA illumination beam is represented by the dark blue oval, which has a narrow

transverse but long axial dimension [84, 85]. The PSF of the collection beam has a similar shape, as represented by the green oval in **Figure 2.1 (b)**. The overall PSF of a DAC system (black oval) is equivalent to the product of the PSFs of the two off-axis beams [84, 85].

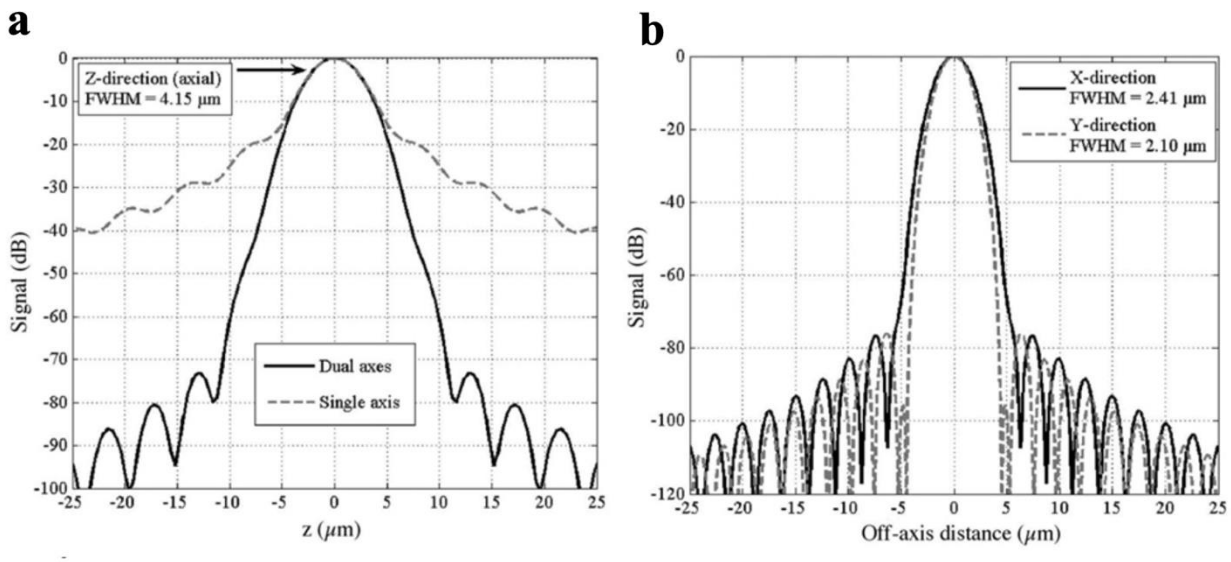

Figure 2.2. Theoretical axial response (a) and transverse response (b) to a point reflector for a dual-axis and single-axis confocal microscopes with equivalent axial resolutions. This figure was originally published in [85].

The DAC microscopy demonstrates several advantages over the conventional SAC microscopy for deep-tissue imaging: (i) the DAC configuration provides a spatial resolution that is relatively isotropic in all three dimensions, while the axial resolution of SAC microscopy is often significantly worse than its lateral resolution (due to the use of high-NA optics); (ii) the long working distance of low-NA optics allows for a scanning mirror to be placed on the beam-focusing side of the objective (post-objective side), which is advantageous for optical imaging over a large field of view; (iii) low-NA optics are easier to fabricate and are less sensitive to off-axis aberrations compared to high-NA optics; (iv) when the illumination and collection beams are separated, the out-of-focus and multiply-scattered photons existing in the illumination path (blue region in **Figure 2.1 (b)**) are less likely to be detected by the off-axis collection beam, providing a better

SBR and a longer depth of optical sectioning. Diffraction-theory calculations [84, 85] have been performed to show that the DAC configuration provides superior rejection of background signals compared to a conventional SAC architecture (**Figure 2.2**).

2.2 POINT-SCANNED (PS) VS. LINE-SCANNED (LS) MICROSCOPES

In a point-scanned (PS) confocal microscope, the focused point is scanned within tissues in two dimensions and an image is reconstructed pixel-by-pixel. Point-scanning provides high image contrast and resolution, but its imaging speed is typically slow (~ a few Hertz), which makes the microscope performance to be highly sensitive to motion artifacts, especially when performing *in vivo* optical imaging [32, 87-90].

In a line-scanned (LS) confocal microscope, the focal line, which is generated by cylindrical focusing optics, is scanned through tissue only in one dimension and an image is reconstructed line-by-line. Instead of a point detector, a LS confocal microscope utilizes an array detector to image the entire line of pixels simultaneously [32, 87-90]. Although the line-scanning approach sacrifices a modest level of imaging resolution and contrast due to the loss of confocality along one axis [32, 87-90], it provides the following advantages compared to the point-scanning approach: (i) since a line of pixels is imaged simultaneously, line-scanning can theoretically gain an n times improvement in imaging speed, where n is the number of pixels per line; (ii) since only one dimension of scanning is required to generate a two-dimensional image, line-scanning simplifies the scanning mechanism and enables significant cost savings compared to the use of a bi-axial scanning mirror [32, 87-90].

2.3 MONTE-CARLO SIMULATIONS

To fully evaluate the performance tradeoffs of different confocal microscope configurations, we utilized FRED software (Photon Engineering, Tucson, AZ) to perform Monte-Carlo simulations. This study has been published in [91, 92]. Reprint permissions have been obtained from the publishers.

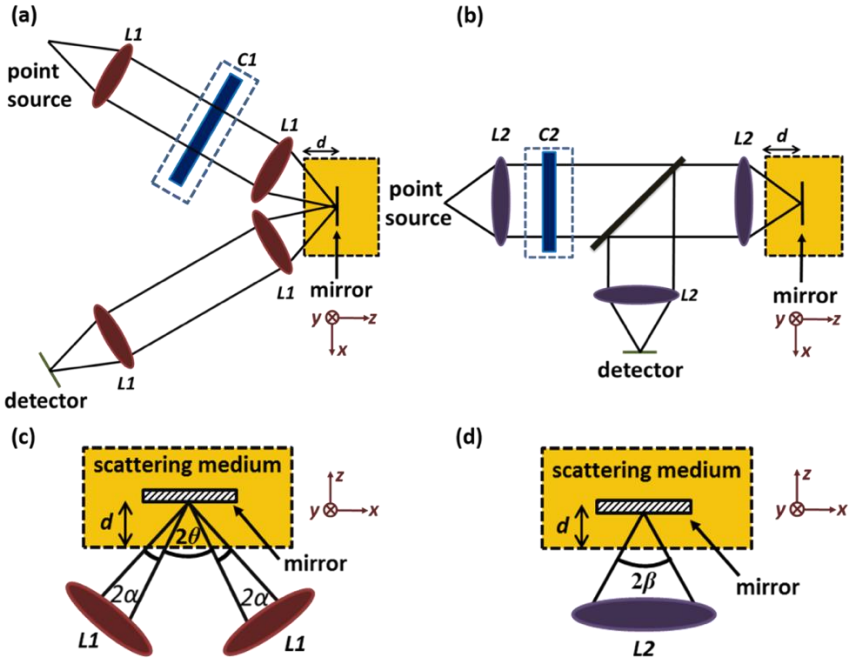

Figure 2.3. a) DAC and (b) SAC microscope designs used for Monte Carlo simulations. The focal regions were shown in (c) and (d) for the DAC and SAC, respectively. This figure was originally published in [92].

The FRED software performed Monte-Carlo ray tracing based on a Henyey-Greenstein approximation of Mie scattering theory [93]. The tissue model used in these simulations had a scattering coefficient, μ_s, of 30 mm^{-1} and an anisotropy factor, g, of 0.81. These values were intended to model the scattering parameters measured with human skin at around 633 nm to 810 nm [94]. To eliminate aberrations and reflections created at the air-tissue interfaces and to simplify the model, the index of refraction of the scattering media, n, was set as unity [91, 92]. These Monte-

Carlo simulations were designed to assess tissue imaging performance for various confocal configurations (both point-scanned and line-scanned SAC and DAC microscopes) in reflectance mode but do not account for polarization, diffraction and absorption [92]. Furthermore, these simulations did not reflect other scattering events in real tissue, such as refractive beam steering and lensing effects introduced by heterogeneous tissue structures that have sizes larger than the operating wavelength of light (785 nm in this study) [91, 92]. Nevertheless, Monte-Carlo simulations have provided a good first order approximation of optical-sectioning performance in tissues and have been successfully validated via experiments with homogeneous scattering phantoms such as intralipid [84, 95].

The geometric models used for simulation were presented in **Figure 2.3** [92]. In the DAC setup, two off-axis Gaussian beams were aligned such that the illumination and collection beams intersect at their focus with a crossing half angle, θ, of 30 degrees. Each individual beam had a $1/e^2$ focusing half angle, α, of 0.11 rad and the lens (*L1*) used in the DAC had a focal length of 25.6 mm. Based on diffraction theory, the SAC was designed to have the same full width at half maximum (FWHM, -3 dB) axial resolution as the DAC. Thus, the $1/e^2$ focusing half angle, β, of the SAC was calculated as 0.42 rad. For the SAC microscope, a custom aspheric lens (*L2*) with a focal length of 16.8 mm was designed in ZEMAX to produce a diffraction-limited focus and was imported into FRED. To generate a focal line for LS configurations, a cylindrical lens was added into both the DAC and SAC models. The focal lengths of these cylindrical lenses were chosen to yield a focal line that was roughly 500 µm long at the imaging plane (focal length for *C1* = 300 mm and *C2* = 1000 mm).

In our simulations [92], the detector plane had a grid spacing of 0.5 µm. Since the DAC and SAC architectures utilized beams with different NAs, the diffraction-limited focal spot sizes

were different. Therefore, in each microscope setup, a detector pinhole of an appropriate focal spot size was created by binning the pixels at the center of the detector. For the DAC configuration, a 7 x 7 bin of detector pixels, corresponding to a physical pinhole size of 3 x 3 µm, was utilized. This pinhole size was found to provide an optimal signal-to-background ratio (SBR) in our simulations and was slightly larger than the diffraction-limited spot size of a beam with a $1/e^2$ NA = 0.11. For the SAC configuration, a 3 x 3 bin of detector pixels, corresponding to a physical pinhole size of 1 x 1 µm, was chosen. This also yielded an optimal SBR in our simulations and was slightly larger than the diffraction-limited spot size of a beam with a $1/e^2$ NA = 0.42. Here, we defined the $1/e^2$ NA = n sin (γ), where n was the index of refraction of the medium and γ was the half angle of a focused Gaussian beam measured to the $1/e^2$ intensity point ($\gamma = \alpha$ for the DAC and $\gamma = \beta$ for the SAC).

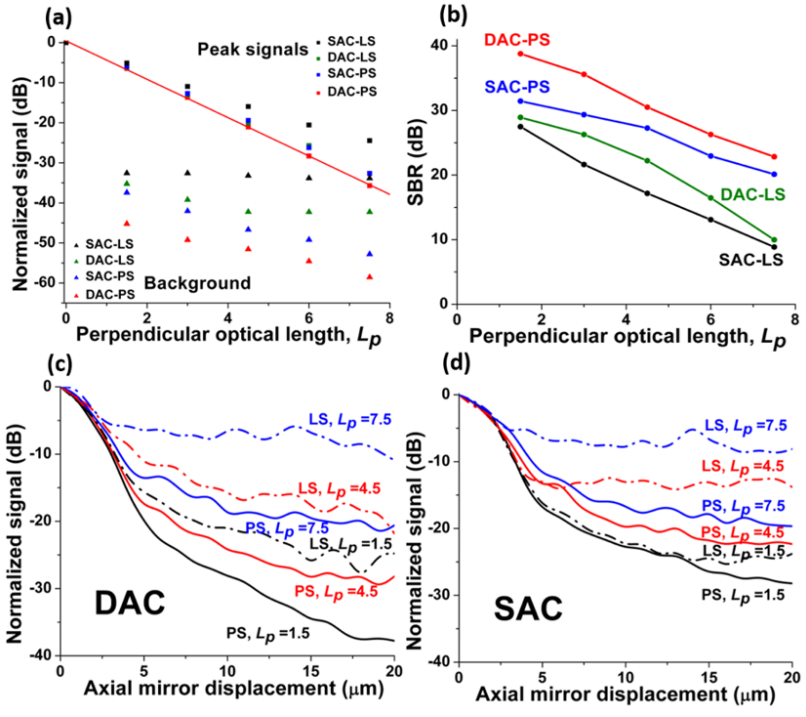

Figure 2.4. (a) The simulated peak signal from a mirror at the focus, and the scattering background (no mirror), as a function of imaging depth (L_P) for all confocal microscope architectures. A linear fit of the DAC-PS peak signal was also shown above. (b) The signal-to-background ratio (SBR) for all configurations. The axial responses of the DAC (c) and SAC (d) configurations with L_P = 1.5, 4.5 and 7.5. This figure was originally published in [92].

We first simulated the peak signal obtained by different confocal microscope architectures (point-scanned DAC, line-scanned DAC, point-canned SAC, and line-scanned SAC) with a 100% reflective mirror placed at the focal plane [92]. These peak signals were dominated by ballistic (non-scattered) photons while contained a small amount of background signals. Theoretically, according to the Beer-Lambert Law [84, 85], this peak signal should decay as an exponential function of imaging depth within tissue. **Figure 2.4 (a)** confirmed that the normalized peak signals, plotted logarithmically in dB, do obey the Beer-Lambert relation. In **Figure 2.4 (a)**, imaging depth was expressed as a non-dimensional quantity, the "perpendicular optical length," L_P. This is the total number of mean free paths travelled by ballistic (non-scattered) photons in a perpendicular roundtrip path between the tissue surface and the mirror, $2\mu_s d$. The background signal was calculated by removing the mirror from the simulation. The maximum signal-to-background ratio, calculated from the data in **Figure 2.4 (a)**, was plotted in **Figure 2.4 (b)**. Next, axial scans were simulated at various depths within the homogenous scattering medium. In this case, a flat mirror was translated axially away from the microscope's focal plane to determine the axial response of the microscope as a function of imaging depth. The axial responses for all architectures were presented in **Figures 2.4 (c) and (d)**.

For simulating transverse knife-edge scans, we exploited a reflective target consisting of a 0.1% reflective surface adjacent to a 100% reflective surface (30 dB contrast). This knife edge was placed at the focal plane of the microscopes. For PS configurations, this knife edge was translated along the focal plane in the *y* direction (**Figure 2.3**). For LS configurations, this knife edge was kept stationary, and the focal line extended in the *y* direction across the knife edge. The transverse responses for all confocal microscope architectures were shown in **Figure 2.5**.

Simulations [92] suggested that the DAC configuration produced a higher SBR than the SAC configuration when comparing their respective point-scanning and line-scanning modes. Axial-response simulations (**Figures 2.4 (c) and (d)**) showed that the DAC microscope had a lower background floor than the SAC microscope through up to L_P = 7.5 within a homogenous scattering medium. This agrees with previous experimental data on the ability of the DAC configuration to reject out-of-focus and multiply scattered light in tissues [84, 85]. However, this contrast improvement was not as pronounced at deep imaging depths. For instance, in **Figure 2.4 (b)**, the SBR at larger imaging depth (L_P = 7.5) was not significantly better for the DAC compared with the SAC in both PS and LS modes.

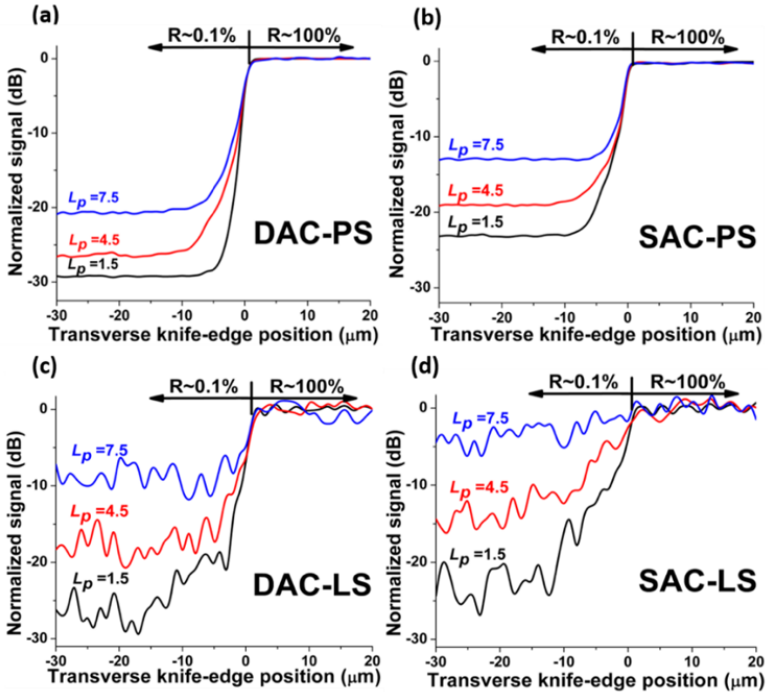

Figure 2.5. Transverse responses to a knife-edge reflective target at various imaging depths, L_P =1.5, 4.5, 7.5, for the DAC-PS (a), SAC-PS (b), DAC-LS (c) and SAC-LS (d) architectures. This figure was originally published in [92].

As described in Chapter 2.2, many investigators have been interested in line-scanned confocal microscopy because of its potential to achieve high-speed imaging with the reduced complexity of only requiring beam scanning in one direction [92]. However, a primary limitation

of line-scanning approaches was that the lack of confocality in one-dimension results in greater photon crosstalk and diminished rejection of out-of-focus and multiply scattered background light. We simulated the transverse response to evaluate this crosstalk [92]. In **Figure 2.5**, we observed that pixel crosstalk degrades image contrast in both the DAC-LS (**Figure 2.5 (c)**) and SAC-LS (**Figure 2.5 (d)**) configurations compared to their respective PS counterparts (**Figures 2.5 (a) and (b)**). This crosstalk also caused the transition length at the knife edge to increase for the LS microscopes. For example, when comparing **Figures 2.5 (b)** and **(d)**, it was apparent that the LS-SAC showed a much slower transition in signal at the knife edge compared to the PS-SAC. However, **Figures 2.5 (a)** and **(c)** showed that this crosstalk-induced degradation at the knife edge was less obvious for the DAC. A direct comparison between **Figures 2.5 (c)** and **(d)** suggested that the DAC architecture was better than the SAC for line scanning, resulting in superior contrast as well as transverse spatial definition at perpendicular optical lengths of up to $L_P = 7.5$.

In summary, Monte-Carlo simulations [92] showed that spatial resolution was maintained in all microscope architectures at shallow depths. The axial resolution was defined by the FWHM (-3 dB) points and transverse resolution was defined by the 10% to 90% transition width. These simulations were performed with a homogenous scattering medium. Real biological tissues which contain heterogeneities could result in degraded spatial resolution as a function of depth. In both PS and LS modes, the DAC was superior to the SAC, especially at shallow imaging depths. In particular, we found that for line scanning, the DAC showed less degradation in contrast and spatial definition compared to the SAC. This suggests that the combination of a DAC architecture and line scanning could provide an optimal balance between imaging speed, depth, resolution, contrast, and cost for certain *in vivo* imaging applications, such as oral cancer detection and guiding brain tumor resection.

2.4 Optimizations of DAC microscopes

Contrast and spatial resolution are two crucial performance parameters to consider when developing and designing microscopes for different applications. Previous diffraction theory studies [84, 85] have indicated that spatial resolution of a DAC microscope depended on both the crossing half angle of the dual-axis beams, θ, and the focusing NA of the individual beams, α. It has been generally recognized that tissue-imaging contrast of a DAC microscope is a function of θ and α. However, this relationship has not yet been well studied. Since diffraction theory did not model any scattering events, Monte Carlo simulations were utilized here to describe the tissue-imaging performance (contrast) of PS-DAC and LS-DAC configurations in reflectance mode as a function of θ and α [91]. As mentioned in Chapter 2.3, tissue-imaging contrast in this study was defined as the ratio between the in-focus signal in an image and the background signal due to out-of-focus and multiply scattered light: the signal-to-background ratio (SBR). Furthermore, to provide a comprehensive guide for the design of these devices, we also included diffraction theory calculations of spatial resolution as a function of θ and α [91]. This study has been published in [91]. Reprint permission has been obtained from the publisher.

The FRED software inputs and geometric models were kept consistent with previous simulation setup [92]. We varied θ and α in the simulations to analyze their effects on contrast and resolution. Based on the experience in building DAC microscope systems, we limited our analysis to a range of practical values: 0.1 rad < α < 0.25 rad; and 15º < θ < 35º. To investigate the effect of each variable independently, α was fixed at 0.11 rad when θ was changed. Similarly, θ was kept at 30º when α was varied [91]. Varying α changed the diffraction-limited spot size at the detector. Therefore, the pinhole size at the detector must be adjusted as α is altered [91]. For instance, when α = 0.1 rad, we chose a pinhole size of 3 x 3 μm, which was slightly larger than the spot size

calculated by diffraction theory. Since the diffraction-limited spot size scaled with 1/α, if α increased to 0.2 rad, the pinhole changed to 1.5 x 1.5 µm. In all simulations, our detector plane was oriented perpendicularly to the collection beam and was consisted of pixels separated by 0.1 µm. Thus, a 3 x 3 µm pinhole corresponded to a 31 x 31 bin of detector pixels, whereas a 1.5 x 1.5 µm pinhole corresponded to a 16 x 16 bin of detector pixels [91].

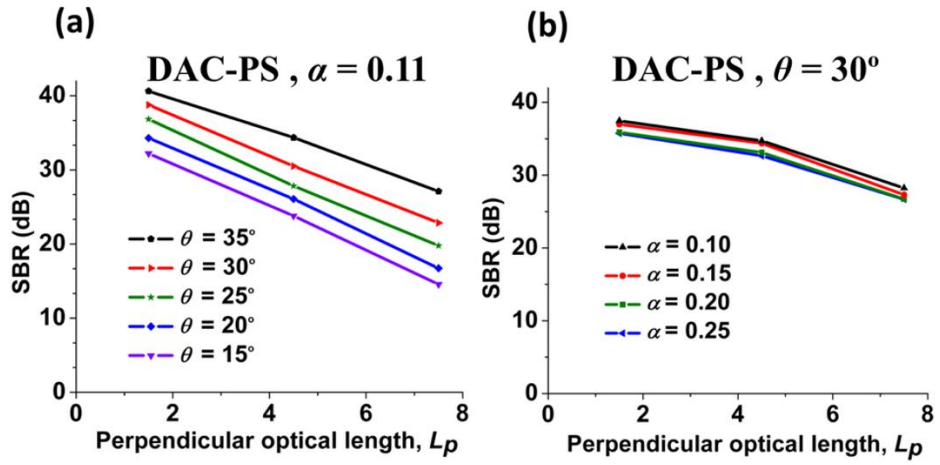

Figure 2.6. The signal-to-background ratio for the DAC-PS configuration as a function of imaging depth, L_p, when (a) varying θ with α fixed at 0.11 rad and (b) varying α with θ fixed at 30°. This figure was published in [91].

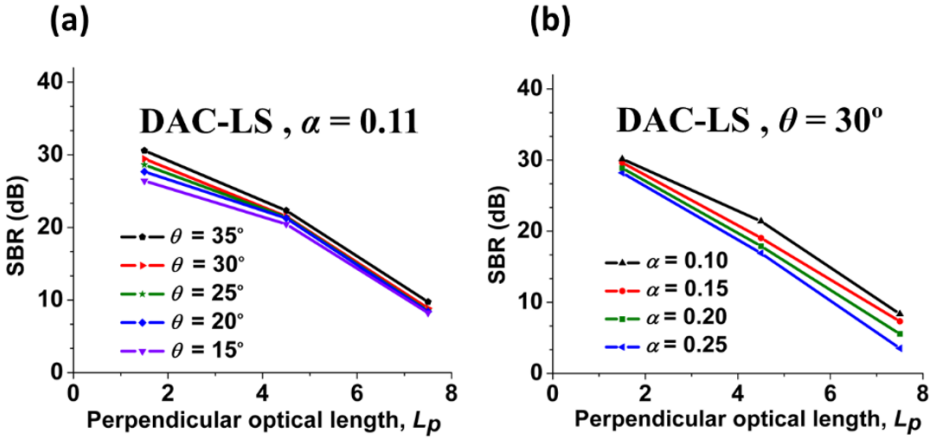

Figure 2.7. The signal-to-background ratio (SBR) for the DAC-LS configuration as a function of imaging depth, L_p, when (a) varying θ with α fixed at 0.11 rad and (b) varying α with θ fixed at 30°. This figure was originally published in [91].

Simulation results [91] indicated that the effects of θ and α on contrast and resolution were quite different for the PS-DAC vs. LS-DAC architectures. For PS-DAC configuration, a plot of SBR vs. imaging depth (L_P) for the PS-DAC configuration was shown in **Figure 2.6**. In **Figure 2.6 (a)**, when α was fixed, increasing θ resulted in improved SBRs for all depths. However, **Figure 2.6 (b)** showed that SBR was not sensitive to variations in α. These results indicated that maximizing θ was important for achieving high contrast (i.e., rejecting as much out-of-focus and multiply scattered light as possible) for the PS-DAC design while varying α was not as important [91]. For LS-DAC configuration, a plot of SBR vs. imaging depth (L_P) for the DAC-LS configuration was shown in **Figure 2.7**. **Figure 2.7** indicated that increasing θ was not as important, compared to the PS-DAC configuration, for improving SBR; but increased θ did make a slight difference in improving the contrast at shallow depths. **Figure 2.7 (b)** suggested that varying α played a minor role in improving contrast. Note that for the LS-DAC configuration, overall SBR performance was worse than for the PS-DAC. Therefore, the DAC-LS would likely be utilized only for imaging at shallow depths [91].

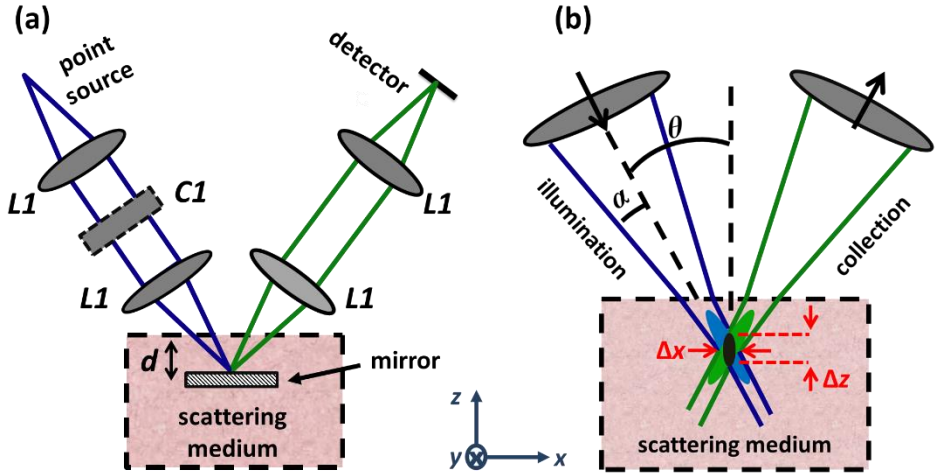

Figure 2.8. (a) The DAC model used for Monte-Carlo simulations (b) The focal region of a DAC microscope. In the DAC architecture, the illumination and collections beams intersected at a focal volume (black) with spatial resolution Δx and Δz. This figure was originally published in [91].

In previous study [84, 85, 96], the FWHM spatial resolution was calculated from diffraction theory:

$$\Delta x = \frac{0.466\lambda}{n(\pi/2\cdot\alpha)\cos\theta}, \quad \Delta y = \frac{0.466\lambda}{n(\pi/2\cdot\alpha)}, \quad \Delta z = \frac{0.466\lambda}{n(\pi/2\cdot\alpha)\sin\theta} \tag{1}$$

For the DAC-PS configuration (**Figure 2.8**), Δy only depended on the focusing NA of the individual beams, α, and was not a function of crossing angle, θ. For the LS-DAC configuration, since the focal line extended in the y direction, Δy was determined by how fully the linear array sampled the line according to the Nyquist sampling criteria. Here, we focused our analysis on the spatial resolution in the x and z directions, which were functions of both θ and α, as seen in Eq. (1). In order to apply these calculations for all wavelengths, a non-dimensional resolution was reported by normalizing against wavelength, λ: $\Delta x/\lambda$ and $\Delta z/\lambda$. These diffraction results applied for both the PS-DAC and LS-DAC designs [91].

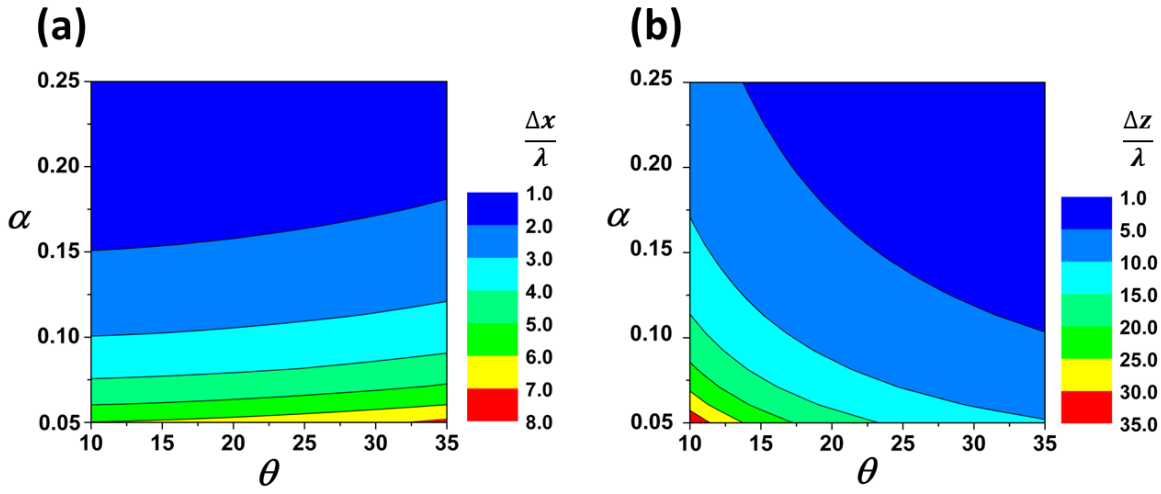

Figure 2.9. Contour plots for non-dimensional spatial resolution: (a) $\Delta x/\lambda$ and (b) $\Delta z/\lambda$. This figure applies to both the DAC-PS and DAC-LS configurations. This figure was originally published in [91].

The contour plots in **Figure 2.9** were utilized to assess the effect of θ and α on spatial resolution (x and z direction). **Figure 2.9 (a)** implied that α contributes more than θ in determining

Δx. In particular, for a fixed θ, high NA beams (large α) helped to ensure high resolution in the x direction. However, for a fixed α, increasing θ only slightly improved Δx resolution. **Figure 2.9 (b)** indicated that, in order to achieve good resolution in the z direction, maximizing both θ and α was necessary.

Both Monte-Carlo simulations and diffraction theory calculations [91] suggested that the optimization of DAC configurations may require very different design parameters, depending upon the biomedical application of interest.

First, the dependencies of contrast on θ and α were evaluated by Monte-Carlo simulations [91]. According to **Figure 2.6**, SBR for PS-DAC was more sensitive to θ rather than α. In particular, increased θ resulted in better SBR. An explanation for this result was that the illumination and collection paths moved closer to each other when their half crossing angle, θ, decreased. As the two beams moved closer to each other, the out-of-focus and multiply scattered photons generated by the illumination beam were more likely to scatter into the collection beam. Therefore, increasing θ improved the SBR (contrast). When the focusing NA of each individual beam, α, increased, the illumination and collection beams also moved closer to each other, which should worsen the SBR. However, since the diffraction-limited spot size at the detector was reduced when α is increased, the correspondingly smaller pinhole improved the rejection of out-of-focus and multiply scattered background light. These two effects balanced each other; which ultimately caused the DAC-PS to be relatively insensitive to changes in α. **Figure 2.7** displayed the effect of varying θ and α on the contrast of the LS-DAC configuration [91]. At shallow depths, maximizing θ resultd in a slight improvement in SBR, but this contrast improvement in the LS-DAC architecture was much less than in the PS-DAC architecture. We hypothesized that this may be due to photon crosstalk serving as the dominant source of background in the LS-DAC

configuration. The lack of confocality in one dimension for the line-scanned approach created crosstalk between pixels along the focal line at the detector. This crosstalk diminished the LS-DAC architecture's ability to reject out-of-focus and multiply scattered background light, and thereby limited the achievable contrast (SBR) of the line-scanned DAC.

Although diffraction theory [91] did not account for scattering events, it allowed us to express spatial resolution as a function of θ and α. Monte-Carlo simulations along with diffraction theory calculations provided a comprehensive guide to optimize the DAC-PS and DAC-LS microscopes for various imaging applications. For a DAC-PS microscope, optimization should seek to balance both contrast and spatial resolution. Since increasing θ was more important than α for obtaining highest contrast for a DAC-PS microscope, optimizing the DAC-PS design should prioritize the beam crossing half angle, θ. Moreover, according to diffraction theory, given a maximized θ, increasing α would be also preferred for maintaining good Δx and Δz resolution. Increasing α would only slightly reduce contrast for the DAC-PS design. For the DAC-LS design, since contrast was not overly sensitive to variations in either θ or α, its optimization should focus on obtaining high spatial resolution (x and z direction). In the x direction, good resolution required maximizing α. In the z direction, increasing both θ and α improved resolution.

In practice, one's choice of θ or α is often limited by pragmatic concerns such as working distance, device size, as well as the position and size of the scanning mechanism. Generally, large crossing angles, θ, imply larger device sizes and shorter working distances. Large crossing angles, θ, and beam numerical apertures, α, together may create additional challenges for aberration-corrected optics and the index-matching of beams into tissues [97-99].

2.5 A TABLE-TOP LS-DAC MICROSCOPE OPTIMIZED FOR VIDEO-RATE *IN VIVO* IMAGING

Although microscopy of *ex vivo* tissues provides valuable information for biological investigations and clinical diagnoses, key insights into dynamic processes, such as blood cells trafficking within capillary networks, can only be obtained under *in vivo* settings [100-103]. Video-rate microscopy (defined here as >15 frames-per-second, fps) at frame rates of up to 30 fps, has shown utility for monitoring these cellular-level dynamics [88]. In addition, high frame rates are useful for mitigating motion artifacts due to respiration or due to mechanical jitter when a human operator holds a handheld or endoscopic microscope [7, 104-107]. Previous feasibility studies, with a slow stage-scanned line-scanned LS-DAC microscope [108], have demonstrated that LS-DAC microscopy was capable of imaging tissues with subcellular resolution and high contrast at moderate depths of up to several hundred microns. However, the sensitivity and performance of a video-rate LS-DAC imaging system, with low-numerical aperture optics, have not yet been verified. Exploiting a state-of-the-art sCMOS camera and a galvanometric line-scanning mirror, we have demonstrated the ability to perform sensitive *in vivo* video-rate LS-DAC fluorescence microscopy of anesthetized mice and *ex vivo* tissues (mouse and human) at 12 fps (FOV ~ 500 x 500 µm) or 30 fps (FOV ~ 150 x 500 µm). This study has been published in [88]. Reprint permission has been obtained from the publisher.

Figure 2.10 [88] provided a schematic of the optical setup of the LS-DAC microscope, which was a modified version of a previous system [108]. A singlemode fiber-coupled diode laser (658-nm from Coherent Inc., 488-nm from Coherent Inc., or 405-nm from SFOLT Co., Ltd) was collimated and focused to a ~500-µm-long (FWHM) line in the sample without magnification (Gaussian NA ~ 0.12). A solid immersion lens (SIL) was used to index match the illumination and

collection beams into the sample, increasing the NA of the illumination beam from ~ 0.12 to ~ 0.17 [84, 85]. The light from the sample was collected off-axis from the illumination path (with a half-crossing angle of 30 degrees), transmitted through a long-pass fluorescence filter (Semrock, FF01-496/LP-25) and imaged with 5x magnification (*L2*) onto a sCMOS camera (ORCA flash 4.0 v2, Hamamatsu). A galvanometric scanning mirror (Cambridge Technologies), driven by a custom LabVIEW program (National Instruments), was used to scan the confocal line along the *x* axis. Individual confocal image frames were stitched together line-by-line using a custom MATLAB script (Mathworks) and the image stacks were rendered into videos using ImageJ (NIH).

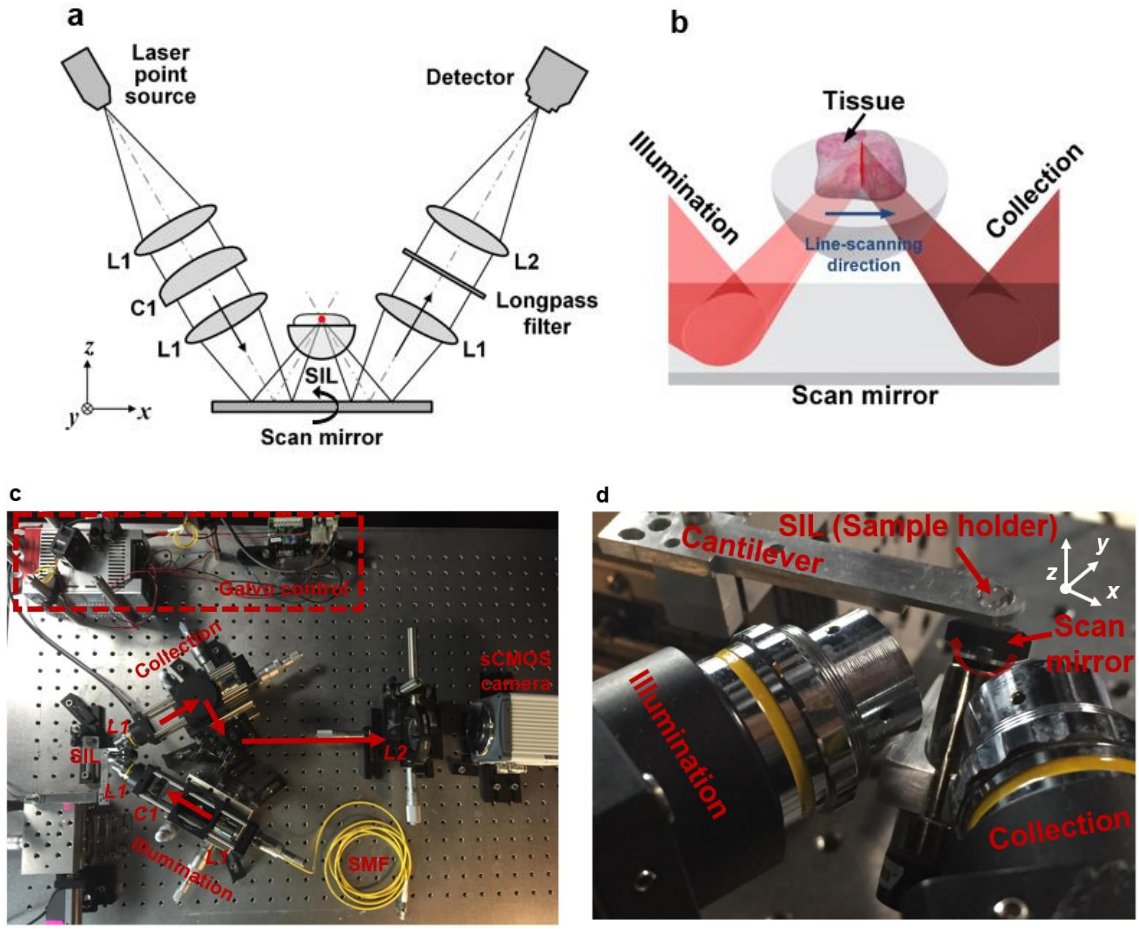

Figure 2.10. (a) Schematic of the video-rate LS-DAC microscope. The scan mirror rotated about the *y* axis and scanned the confocal line in the *x* direction. *C1*: cylindrical lens. (b) Zoomed-in view of the video-rate LS-DAC microscope near the sample. (c) Photograph of the LS-DAC tabletop implementation. SMF: single-mode fiber (d) Photograph of the LS-DAC microscope near the focus. This figure was originally published in [88].

The sCMOS camera used as a detector in this study was able to acquire ~ 5000 to 6000 raw acquisitions (confocal lines) per second (~ 167 to 200 µs exposure time) for a thin rectangular region of interest (ROI) of 32 by 2048 pixels [88]. The center 3-pixel width of this strip corresponded to an imaging dimension of ~ 2.7 µm in the tissue sample (slightly larger than the width of our diffraction-limited focal line) and was binned to create a digital confocal slit. For each 2D image, the scanning mirror was programmed to scan the focal line in the *x* direction (**Figure 2.10**). Serially acquired confocal lines were stitched together, enabling a confocal imaging rate of 12 fps over a ~500 x 500 µm FOV, or a 30-fps video imaging rate over a small ~150 x 500 µm FOV. A consistent sampling pitch of 1.1 µm per pixel was utilized in the *x* direction. According to diffraction theory, the FWHM width of the focal line in tissues should be 1.4 µm. Therefore, we were slightly under-sampling the *x* direction (per Nyquist criteria). The sampling density in the *y* direction was determined by the pixel pitch in the sCMOS camera, which is 6.5 µm. Taking into account the magnification of the SIL sample holder (~1.45), as well as the magnification of the collection-side optics (5x), the sampling pitch within tissue was approximately 0.9 µm per pixel. The diffraction-limited FWHM resolution in the *y* direction was 1.2 µm. Therefore, we were slightly under-sampling the *y* direction per Nyquist.

For *in vivo* imaging, fluorescein isothiocyanate (FITC)-conjugated dextran (Sigma Aldrich, FD2000S, 2000 kDa, 10 mg/mL) was injected retro-orbitally into anesthetized mice to highlight their brain vasculature [88]. The mice were anesthetized with a ketamine/xylaxine cocktail (10 mg/mL ketamine, 1 mg/mL xylaxine) via intraperitoneal injection at 10 mL/kg body mass. The animals were placed on a custom platform that allowed for the imaging of the vasculature in their ears. The animals remained under anesthesia during the imaging experiments and were immediately sacrificed upon the completion of the experiments. In order to image blood

cells trafficking within the capillaries of mouse at various depths beneath the ear skin surface, a computer-controlled actuator (Newport Corporation, CMA-12CCCL) was used to translate the sample stage along the *z*-axis in 25 μm/sec steps (**Figure 2.10)**. Three-dimensional images of mouse-ear vasculature were constructed by acquiring a stack of horizontal image sections (**Figures 2.11 (a) and (b)**).

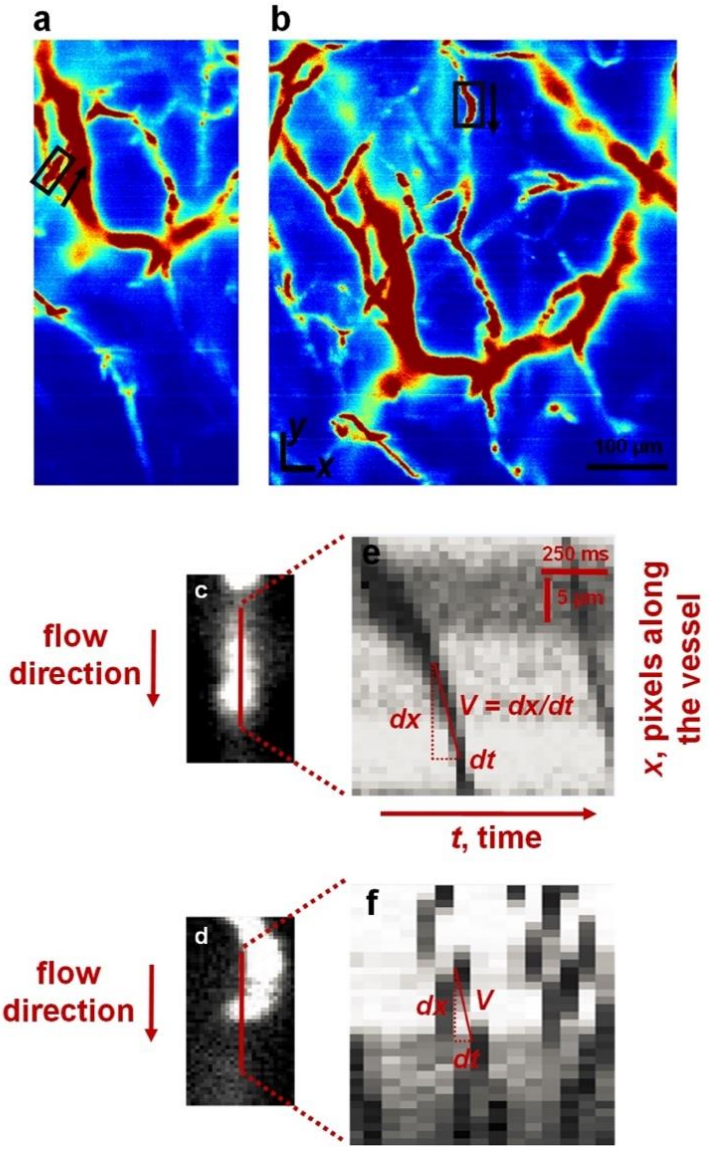

Figure 2.11. LS-DAC microscopy of mouse blood flow at a frame rate of (a) 30 fps over a FOV of 250 x 500 μm and (b) at 15 fps over a FOV of 500 x 500 μm. Panels (c) and (d) were single-vessel images cropped from (a) and (b). The red lines indicated the locations where line-profile data were analyzed in panels (e) and (f) to quantify the velocity of the erythrocytes. The arrows indicated the direction of flow. This figure was originally published in [88].

Figure 2.11 [88] displayed the *z* projection of all the images collected at 30 fps (FOV of 250 x 500 μm) at depths of approximately 125 μm to 200 μm beneath the surface of the mouse ear skin. Blood flow within individual capillaries in the mouse ear can be visualized. Intravenously injected FITC-dextran illuminated the blood plasma while red blood cells can be observed as shadows trafficking through the capillaries. Serially acquired images obtained at a fixed depth were analyzed to determine the velocity of the erythrocytes within individual vessels (**Figures 2.11 (c)** and **(d)**). With a FOV of 500 x 500 μm, the imaging frame rate was decreased to 15 fps (**Figure 2.11 (b)**). However, red blood cells trafficking in the capillaries (0.1 to 2 mm/s [109]) were still visualized and quantified (**Figures 2.11 (d)** and **(f)**). From **Figures 2.11 (e)** and **(f)**, the red blood cells velocities in single capillaries of a live mouse ear were estimated to be ~ 0.1 mm/s (**Figure 2.11 (e)**) and ~0.135 mm/s (**Figure 2.11 (f)**).

To show that the camera exposure times utilized for the *in vivo* imaging experiments could also provide sufficient sensitivity to image tissues topically stained with an exogenous fluorescent contrast agent, excised mouse tongue tissues were topically stained with an FDA-approved agent, methylene blue and used for the *ex vivo* imaging experiment [88]. The *ex vivo* image shown in **Figure 2.12** (captured at 167-μm line-acquisition rate, or 12-fps imaging rate) displayed similar detail and contrast compared to previously published data where a 1-ms line-acquisition rate was utilized [108].

To further validate the flexibility of video-rate LS-DAC microscopy for clinical applications [88], human brain tumor specimens (glioma) were obtained during surgery and imaged with our device. Prior to surgery, 5-aminolevulinic acid (5-ALA), a pro-drug currently in clinical trials (phase II) for image-guided resection of malignant brain tumor, was orally administered to glioma patients at the Barrow Neurological Institute in Phoenix, AZ under an IRB-

approved protocol and IND approval for the use of 5-ALA. 5-ALA can be intracellularly metabolized by the mitochondria to form protoporphyrin IX (PpIX), which has been shown to preferentially accumulate in various tumor cells (including glioma cells). Low-grade gliomas typically do not generate enough PpIX to enable detection using wide-field low-resolution fluorescence imaging, but optical-sectioning confocal microscopy has the resolution and sensitivity to visualize the sparse and punctate PpIX expression in these low-grade tissues. We showed that LS-DAC fluorescence microscopy at 12 fps possessed adequate sensitivity to visualize sub-cellular PpIX expression in thick (un-sectioned) glioma tissues (405-nm excitation and 625-nm collection), as shown in **Figure 2.13**, with good correlation to fluorescence histopathology. Previous studies [110-112] have already indicated the potential benefit of intraoperative confocal microscopy for guiding glioma resections. However, the frame rates of previously developed devices have been insufficient to mitigate motion artifacts during handheld intraoperative use. Therefore, a miniature LS-DAC microscope, with a fast frame rate of 12 fps or higher, would be beneficial.

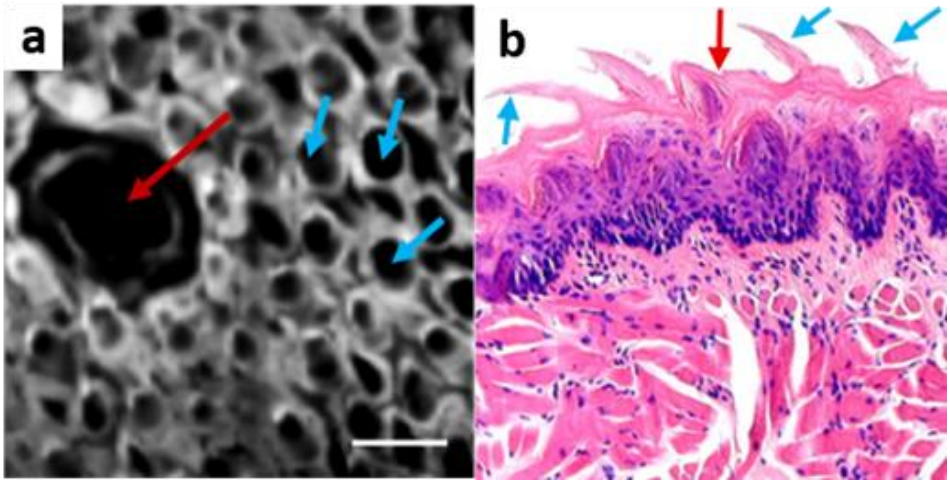

Figure 2.12. (a) Excised mouse tongue stained with methylene blue and fluorescently imaged at 15 fps over a FOV of ~500 x 500 µm). (b) H&E stained histology cross section of a mouse tongue. Scale bar = 100 µm. This figure was initially published in [88].

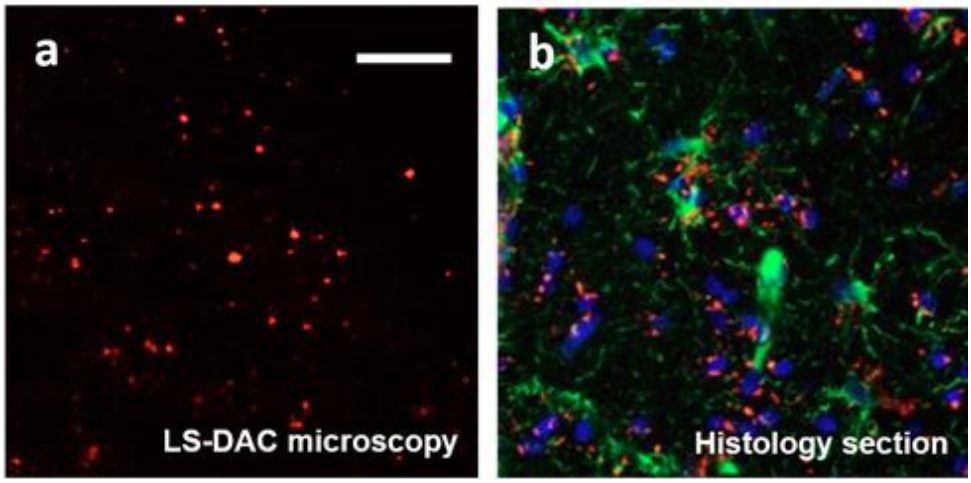

Figure 2.13. (a) Surgically resected glioma (brain tumor) specimen fluorescently imaged at 15 fps over a FOV of ~ 500 x 500 µm. The patient was administered 5-ALA prior to surgery. (b) A histological section of a glioma specimen from a patient administered with 5-ALA prior to surgery. This image has showed DAPI-stained nuclei (blue), 5-ALA-induced PpIX fluorescence (red), and the expression of glial fibrillary acidic protein (GFAP, green). Scale bar = 100 µm. This figure was initially published in [88].

In this study [88], video-rate imaging at 30 fps was achieved with a LS-DAC microscope with sufficient speed, contrast, and sensitivity to visualize *in vivo* blood cell dynamics. In addition, high-speed LS-DAC microscopy at 15 fps has shown sufficient sensitivity and contrast to visualize cellular details in tissues topically stained with a fluorescent contrast agent, methylene blue, as well as the sub-cellular expression of fluorescent PpIX in glioma tissues from patients administered with 5-ALA prior to surgery. No significant photobleaching was noted during the *in vivo* and *ex vivo* experiments [88]. This was the first demonstration of *in vivo* video-rate imaging at 15 to 30 fps with a tabletop LS-DAC device [88], which has provided an important benchmark for a miniature handheld LS-DAC microscope under development in our lab [113, 114]. The results of this study [88] has indicated that LS-DAC microscopy has the potential to provide valuable functional and morphological information for point-of-care cancer diagnostics and intraoperative guidance of tumor-resection procedures [113, 114].

Chapter 3. BESSEL-BEAM ILLUMINATION IN DUAL-AXIS CONFOCAL MICROSCOPY MITIGATES RESOLUTION DEGRADATION CAUSED BY REFRACTIVE HETEROGENEITIES

3.1 FUNDAMENTALS OF BESSEL BEAMS

In recent decades, there has been a renewed interest in exploiting Bessel beams as an illumination approach for deep-tissue laser-scanning microscopy [35-39]. The intensity profile of an ideal Bessel beam can be expressed by a zero-order Bessel function of the first kind where the narrow main lobe of a Bessel beam is encircled by a decaying set of "side-lobe" rings (**Figure 3.1**) [22]. The different approaches to generate a Bessel beam mainly include the use of an axicon lens [115], spatial light modulation [116], or a spiral phase plate [117].

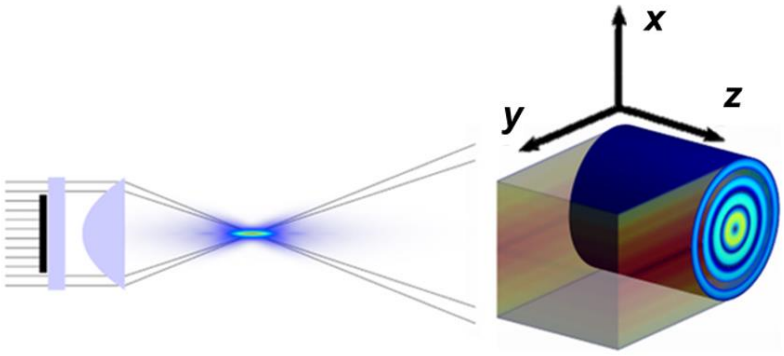

Figure 3.1. The axial and transverse profiles of a Bessel beam [22].

There are two well-known characteristics of a Bessel beam: its "non-diffracting" and "self-reconstructing" properties [35-39]. These characteristics are beneficial for laser-scanning microscopy in large specimens with micro-architectural heterogeneities, such as cell clusters or embryos [35-39]. The "non-diffracting" property of a Bessel beam means the light beam can travel over a long distance along the optical axis without exhibiting any broadening or bending of its main lobe [22]. The "self-reconstructing" property means this main lobe of a Bessel beam can

propagate through highly heterogeneous media, even when there are obstacles blocking or distorting the main lobe temporarily [22]. This self-healing behavior has been supported by the fact that each side lobe of a Bessel beam carries approximately the same amount of energy as the main lobe and continuously serves to reconstruct the main lobe as it propagates [118-120]. Unfortunately, these side lobes have also contributed out-of-focus background that can decrease image contrast, which becomes a trade-off when implementing Bessel beams in various optical microscopy applications [30, 35-39].

In particular, many groups have explored implementing Bessel illumination in light-sheet-based microscopy [21, 23, 36, 38, 39]. When performing light-sheet microscopy with Gaussian illumination in tissues, the field of view (FOV) where the thickness of the light sheet was fairly uniform, was limited and can be approximated by the confocal parameter, or twice the Rayleigh range of the Gaussian beam [22, 30]. Tissue-heterogeneity-induced light-sheet distortions have been demonstrated to decrease the contrast and resolution in Gaussian light-sheet-based microscopy [21, 22, 36]. The "non-diffracting" and "self-reconstructing" characteristics of a Bessel beam have shown promise in addressing these limitations. For example, some have explored utilizing the "non-diffracting" property of Bessel beams to achieve an extended FOV, which can be useful for imaging relatively large biological specimens such as whole embryos [23, 38]. Others have exploited the "self-reconstructing" property of Bessel beams to enhance image contrast and resolution for deep-tissue optical imaging within highly heterogeneous samples [36, 39]. Many of these groups have also explored different approaches, such as structured illumination [21, 121], confocal line detection [122, 123], as well as two-photon excitation [124, 125], to mitigate the background caused by the diffraction side lobes of Bessel beams, providing further improvements for deep-tissue imaging with Bessel light-sheet microscopy.

3.2 CHARACTERIZING THE MOTION AND DISTORTION OF LIGHT BEAMS FOCUSED IN TISSUES

The basic physical principles of Bessel beams have previously been well studied (Chapter 3.1). However, there is a need to quantitatively evaluate the "self-reconstructing" property of Bessel beams compared to conventional Gaussian beams in tissues. We have developed an experimental strategy and a quantitative metric to assess the motion (heterogeneity-induced beam steering) of focused Gaussian and Bessel beams in water, heterogeneous phantoms, and mouse esophagus tissues [30]. In addition, we have developed a second quantitative metric to measure the distortion (heterogeneity-induced beam distortion) of focused Gaussian and Bessel beams in these same media [30]. While recognizing the presence of diffraction side lobes, which must be alleviated to achieve high image contrast, we have concentrated the characterization of Bessel beams on their main lobes alone. This study has been published in [30]. Reprint permission has been obtained from the publisher.

Figure 3.2 displayed the imaging system used in our study [30]. Both Gaussian and Bessel illumination utilized a diode-pumped solid-state laser (Coherent Laser, Inc.) at 550 nm as the light source. For Gaussian illumination, a low-NA Gaussian beam with a pre-SIL (solid immersion lens) NA = 0.12 was imaged without magnification into different samples (water, heterogeneous phantoms containing silica beads of various concentrations, and fresh mouse esophagus tissues) though a pair of matched aspheric lenses (*L1* and *L2*) with a 25-mm focal length (NT49-660, Edmund Optics, Barrington, NJ). For Bessel illumination, an axicon with a 20-deg base angle (Thorlabs AX2520-A) was utilized instead of the second aspheric lens (*L2*) in the illumination path. The FWHM spot size at the sample was 1.2 μm for the Gaussian beam waist and 1.0 μm for the main lobe of the Bessel beam. The samples were placed on a SIL with a refractive index of *n*

= 1.45, which provided index matching to allow the focused beams to enter into tissue-like samples with minimal aberrations. A 100x microscope objective objective (Nikon, PN: 79235, NA=0.9, WD = 1 mm) was utilized to image the beam foci onto a CCD camera (PointGrey, GRAS-14S5M-C with 6.45-µm pixel spacing). An alignment mirror was utilized to direct the beam foci to the same detector region for all measurements (i.e. the same group of CCD pixels), which confirmed a uniform detector response for the CCD. In order to fill the 8-bit dynamic range of the CCD for each experiment and to minimize the effects of detector background, we deliberately altered the laser power for each experimental condition. Experiments were performed in a dark room to eliminate the ambient background. In the absence of light, the dark background count from the CCD was less than 1 count out of 256. Therefore, no background subtraction was necessary [30].

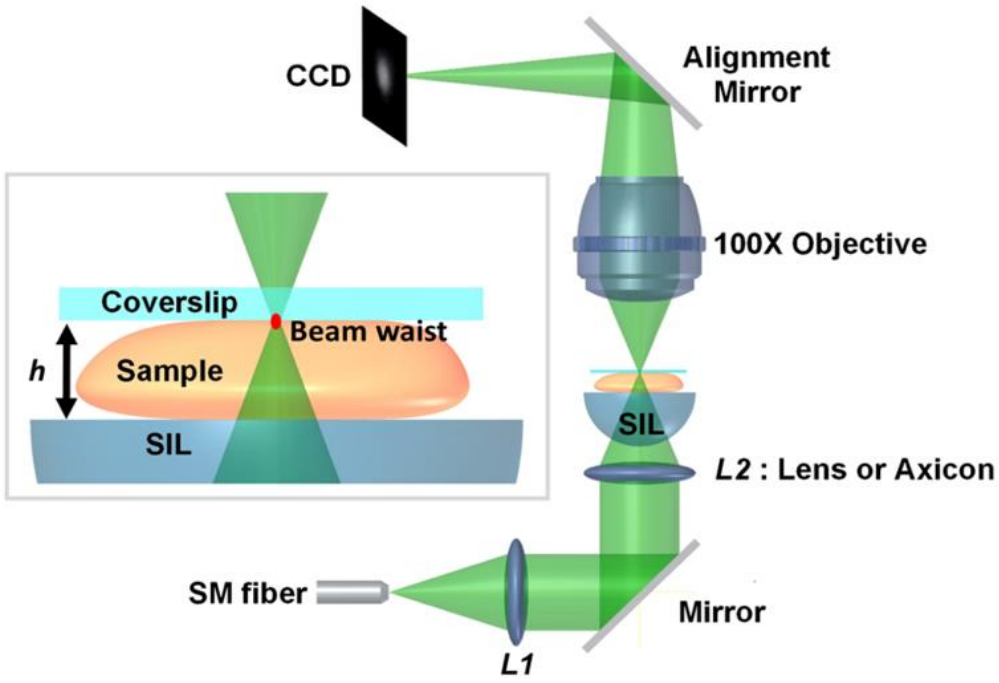

Figure 3.2. The imaging system for quantifying both beam steering and distortion of Gaussian and Bessel beams focused in heterogeneous media. The beam focus (and CCD imaging plane) was positioned at the coverslip interface at the top (far end) of each sample. The distance between the coverslip and the SIL (solid immersion lens), *h*, was 250 µm. This figure was initially published in [30].

In order to gain an insight into the beam-steering phenomenon, and to explain certain aspects of our experimental setup, we performed basic simulations using FRED ray-tracing software (Photon Engineering, Tucson, AZ) [30]. These simulations utilized the same Gaussian illumination conditions that were applied in the imaging experiments and involved placing a single silica bead (10-µm radius) at different locations (x_{bead} = 0, 2, 4… 50 µm; z_{bead} = 10, 200 µm) near the focus (z = 0) of a diffraction-limited Gaussian beam (**Figure 3.3**) [30].

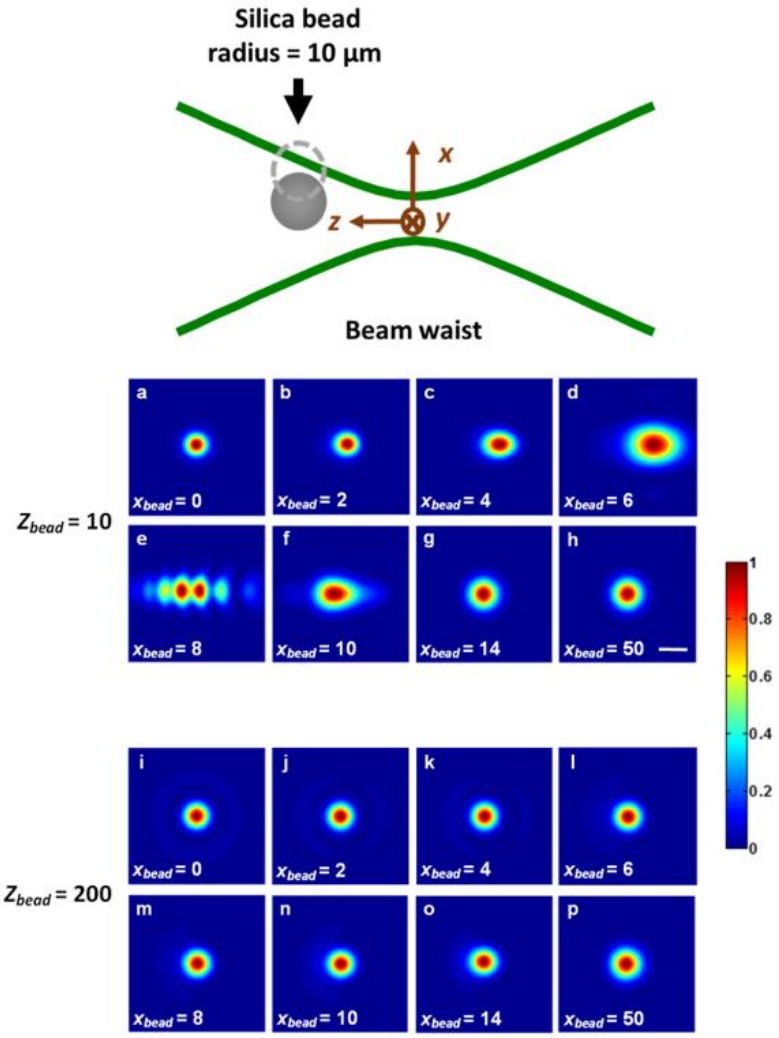

Figure 3.3. Normalized lateral irradiance profiles at the focus (z = 0) of a Gaussian beam (diffraction-based simulations) when a single silica bead with a 10-µm radius was placed at various locations (x_{bead} = 0, 2, 4… 50 µm; z_{bead} = 10, 200 µm) near the focus of the beam. Significant beam steering and distortion of the Gaussian beam focus was observed when the bead was positioned near the focus (z_{bead} = 10 µm); however, negligible beam steering and distortion were observed when the bead was positioned further from the focus (z_{bead} = 200 µm). The scale bar measures 1 µm. This figure was initially published in [30].

As shown in **Figure 3.3**, the magnitude of beam steering and distortion was maximized when the beads were positioned near the focus of the beam: z_{bead} = 10 instead of z_{bead} = 200 µm. Therefore, we needed to image and quantify beam motions and distortions near the beam focus, which was achieved by positioning the focus (as well as CCD imaging plane) at the coverslip interface at the top (far end) of each sample, as shown in the inset of **Figure 3.2**. If the beam focus was located beyond the sample (within or above the coverslip), the measured motion and distortion of the focus was significantly reduced due to a lack of heterogeneities near the focus. If, on the other hand, the beam focus was located deep within the sample (well below the coverslip interface), then the CCD would not be able to accurately image the beam focus due to light scattering (in tissues) between the focus and the camera.

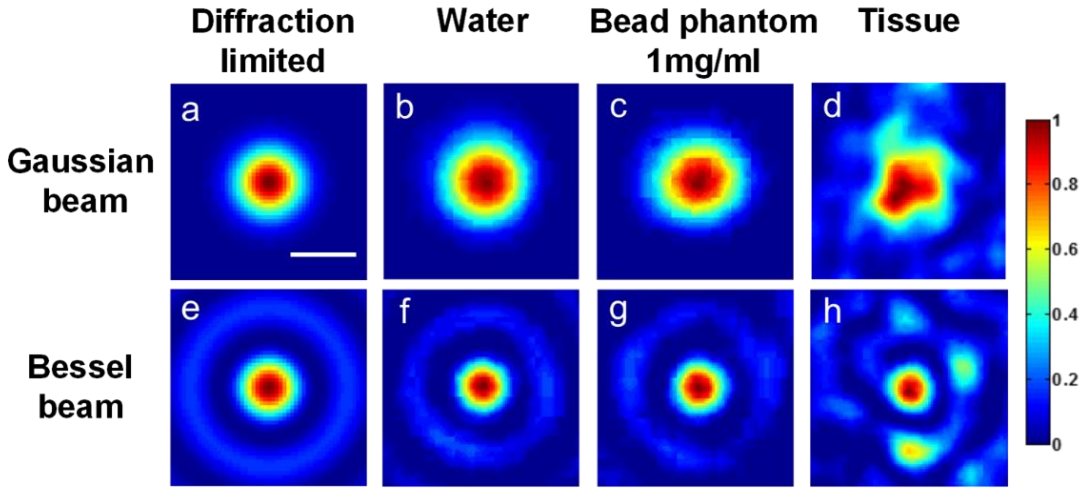

Figure 3.4. The normalized irradiance of focused Gaussian and Bessel beams. From left to right, the columns represent: (a & e) simulations of diffraction-limited beam foci, (b & f) beam foci imaged in water, (c & g) beam foci imaged in bead phantoms (1 mg/ml concentration), and (d & h) beam foci imaged in fresh mouse esophagus tissues. The scale bar measures 1 µm. This figure was initially published in [30].

Figure 3.4 displayed the images of Bessel or Gaussian beam foci in different media (water, heterogeneous phantoms containing silica beads of various concentrations, and fresh mouse

esophagus tissues) [30]. The freshly isolated mouse esophagus tissues, which have a large number of micro-architectural heterogeneities, created more severe beam distortion than the silica-bead phantoms. However, the Bessel beams exhibited less heterogeneity-induced distortions compared to the Gaussian beams in all cases.

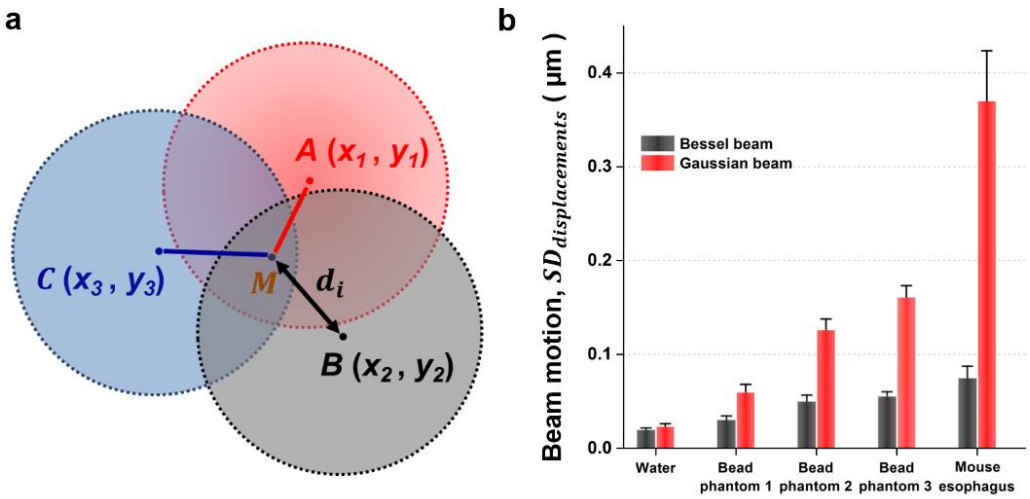

Figure 3.5. Quantification of beam motion. (a) A depiction of how "d_i" is calculated, where d_i is the displacement between the position of individual snap-shot images of beam foci (*A*,*B*,*C*,…) and the average position (unperturbed beam position), *M*. (b) The standard deviation in the displacement of focused Gaussian and Bessel beams in water, bead phantoms and fresh mouse esophagus tissues. Each set of data contains 100 successive snap-shot images of a beam focus. Error bars represent the variability between five sets of data. Bead phantoms 1, 2, and 3 are at concentrations of 0.25 mg/mL, 0.50 mg/mL and 1.00 mg/mL, respectively. This figure was initially published in [30].

The motion of these Gaussian and Bessel beam foci was quantified in MATLAB [30]. **Figure 3.5 (a)** illustrated the calculation of "beam motion", which was the standard deviation in the random "displacement" of *n* snap-shot images of a focused beam taken at different times. The "displacement" referred to the distance between the centroid of each image snap shot and the centroid of an unperturbed beam. The centroids were determined in MATLAB with the "WeightedCentroid" measurement in the "regionprops" function. For example, $A(x_1, y_1)$, $B(x_2, y_2)$,

and $C(x_3, y_3)$ were the centroid coordinates of a focused beam imaged at different times. $M(\bar{x}, \bar{y})$ represented the average centroid position (the unperturbed beam location) from *n* images of the same focused beam, in which *n* images was sufficient to capture the fully randomized motion of the beam. The distance between point $M(\bar{x}, \bar{y})$ (the unperturbed beam location) and each individual centroid position (x_i, y_i) was calculated as [30]:

$$d_i = \sqrt{\left(x_i - \bar{x}\right)^2 + \left(y_i - \bar{y}\right)^2} \tag{2}$$

The standard deviation of the individual displacements for a set of *n* images was therefore calculated as [30]:

$$SD_{displacements} = \sqrt{\frac{1}{n}\sum_{i=1}^{n}(d_i)^2} \tag{3}$$

Figure 3.5 (b) displayed the average beam displacement of focused Gaussian and Bessel beams in water, heterogeneous silica-bead phantoms at 0.25 mg/mL, 0.50 mg/mL and 1.00 mg/mL concentration, as well as fresh mouse esophagus tissues. When imaging beam foci within phantoms and fresh tissues, the motions of the Bessel beams were significantly reduced as compared to the Gaussian beams, indicating that Bessel beams were less sensitive to the heterogeneity-induced beam steering generated by these samples. The beam motions observed for water samples were due to mechanical vibrations from the environment.

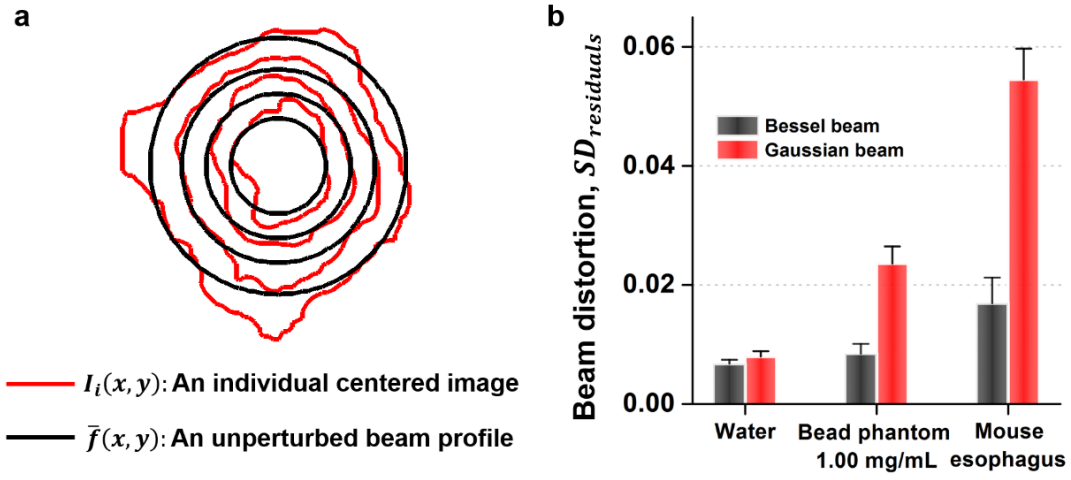

Figure 3.6. Quantification of beam distortion. (a) Contour plots (irradiance isolines) of an unperturbed beam focus (black), and one individual image (red) that is centered with respect to the unperturbed beam. See Methods section for additional details. (b) The standard deviation in the "distortion residual," r_i, which quantifies the beam distortion of focused Gaussian and Bessel beams in water, bead phantoms and fresh mouse esophagus tissues. Each set of data contains 100 successive snap-shot images of a beam focus. Error bars represent the variability between five sets of data. This figure was initially published in [30].

Similarly, we quantified the distortion of the main lobe of the focused Gaussian and Bessel beams in different media (water, heterogeneous phantoms containing silica beads of various concentrations, and fresh mouse esophagus tissues) [30]. Here, "beam distortion" was defined as the standard deviation of a "distortion residual" between each snap-shot image of a beam with respect to an unperturbed beam profile (**Figure 3.6 (a)**), as described below:

1. For each individual image of a focused beam, a 2D Gaussian fit was performed utilizing a least-squares fitting algorithm. Here, we assumed an isotropic Gaussian beam since this fitting function was intended to model an ideal focused beam in the absence of heterogeneity-induced distortions. The fitting function was expressed as:

$$f_i(x,y) = f_0 e^{\left(-\left(\frac{(x-\mu_x)^2+(y-\mu_y)^2}{2\sigma_i^2}\right)\right)} \quad (4)$$

The three fitting parameters in this function were: the centroid location (x and y coordinates) of the focused beam, (μ_x, μ_y), and the isotropic beam width, σ_i.

2. For each set of n images, an average "best-fit" Gaussian surface, $\overline{f}(x,y)$, was used to approximate an unperturbed beam based on the average beam width, $\overline{\sigma}$:

$$\overline{f}(x,y) = e^{\left(-\left(\frac{(x-\mu_x)^2+(y-\mu_y)^2}{2\overline{\sigma}^2}\right)\right)}, \text{ with } \overline{\sigma} = \frac{\sum_{i=1}^{n}\sigma_i}{n} \quad (5)$$

3. Each image (from a set of n individual images) was normalized by dividing the original pixel intensities by f_0 (determined from step 1) to form a new normalized image, $I_i(x,y)$. Since each image, $I_i(x,y)$, had a unique position (center coordinate) due to beam steering, we aligned each image such that the center coordinate of each image snapshot, $I_i(x,y)$, matched the center coordinate of the unperturbed beam, $\overline{f}(x,y)$, as depicted in **Figure 3.6 (a).**

4. By subtracting $\overline{f}(x,y)$ from $I_i(x,y)$, a two-dimensional matrix ($\boldsymbol{R_i}$) was created to represent the absolute value of the difference ("residual") between $I_i(x,y)$ and $\overline{f}(x,y)$ on a pixel-by-pixel basis.

5. A region of interest (ROI), defined by the full-width-at-10%-maximum irradiance of $f_i(x,y)$, was applied for both Gaussian and Bessel beams in order to focus our analysis on the main lobe itself and to reject beam distortions due to system noise and side-lobe aberrations. The distortion quantification was not strongly dependent on our choice of the threshold.

6. For each individual image, a "distortion residual" metric, r_i, was calculated by averaging all elements in matrix $\boldsymbol{R_i}$ within the ROI.

7. The standard deviation of the distortion residuals was calculated as:

$$SD_{residuals} = \sqrt{\frac{1}{n}\sum_{i=1}^{n}(r_i)^2} \quad (6)$$

As shown in **Figure 3.6 (b)**, focused Gaussian beams exhibited more distortion than focused Bessel beams. The beam distortions observed for water samples were due to aberrations and mechanical vibrations [30].

In summary, this study focused on characterizing the "self-reconstructing" property of Bessel beams in heterogeneous media in comparison with conventional Gaussian beams [30]. We designed several experiments to characterize two parameters that were of particular importance for certain imaging applications: the positional stability and distortion of a focused Bessel beam, in comparison to a focused Gaussian beam, when propagating through heterogeneous media. In addition to imaging the foci of low-NA beams in heterogeneous tissues, we defined two metrics to quantify beam steering and beam distortion, respectively. By analyzing the beam steering and distortion of low-NA focused Gaussian and Bessel beams in different media, results suggested that Bessel illumination was superior for maintaining the position and shape of a focused beam, which could have implications for laser-scanning microscopy within highly scattering and inhomogeneous samples.

3.3 A DAC MICROSCOPE WITH GAUSSIAN- VS. BESSEL-BEAM ILLUMINATION

As mentioned in Chapter 1.1, one of the challenges facing laser-scanning microscopy of biological specimens is that refractive heterogeneities due to micro-architectural structures - such as nuclei, organelles, glands, and vasculature - can cause spatial variations of optical beam foci in terms of shape (aberrations / distortions) and position (beam steering) [23, 35-39, 126]. In particular, the

tissue-imaging performance of a DAC microscope (Chapter 2.1) is highly sensitive to the effects of refractive heterogeneities because of its reliance on two beam paths (illumination and collection) that must intersect at their foci. For example, it has been shown that the in-focus signal collected by a DAC microscope was significantly decreased when the alignment of the illumination and collection beams was spatially modulated at the micron scale [127, 128]. In addition, as shown in previous studies with tissue phantoms and through *in vivo* imaging experiments of human epidermis [32, 95], refractive heterogeneities in tissues led to a degradation in spatial resolution for DAC microscopy, with a concomitant loss in sensitivity (signal-to-noise ratio, SNR) and contrast (signal-to-background ratio, SBR) [30].

The preliminary studies (Chapter 3.2) have shown that in media with refractive heterogeneities, the irradiance profile of a focused Bessel beam exhibited superior positional stability and beam quality (in the main lobe of the Bessel beam) compared with a focused Gaussian beam, which suggested that Bessel beams could be conducive to maintain resolution in DAC microscopy of tissues [30]. In order to validate this hypothesis, this study utilized both Gaussian and Bessel illumination in a point-scanned DAC microscope in order to quantify the resultant degradation of resolution when imaging in phantoms with tissue-like heterogeneities, as well as when imaging fresh biological tissues. Experimental results were compared with realistic simulations exploiting a novel fractal propagation method (FPM) [129] that we have recently developed. Results indicated that the use of Bessel beam illumination in DAC microscopy of tissues resulted in less degradation in resolution compared to conventional Gaussian beam illumination. This study has been published in [34]. Reprint permission has been obtained from the publisher.

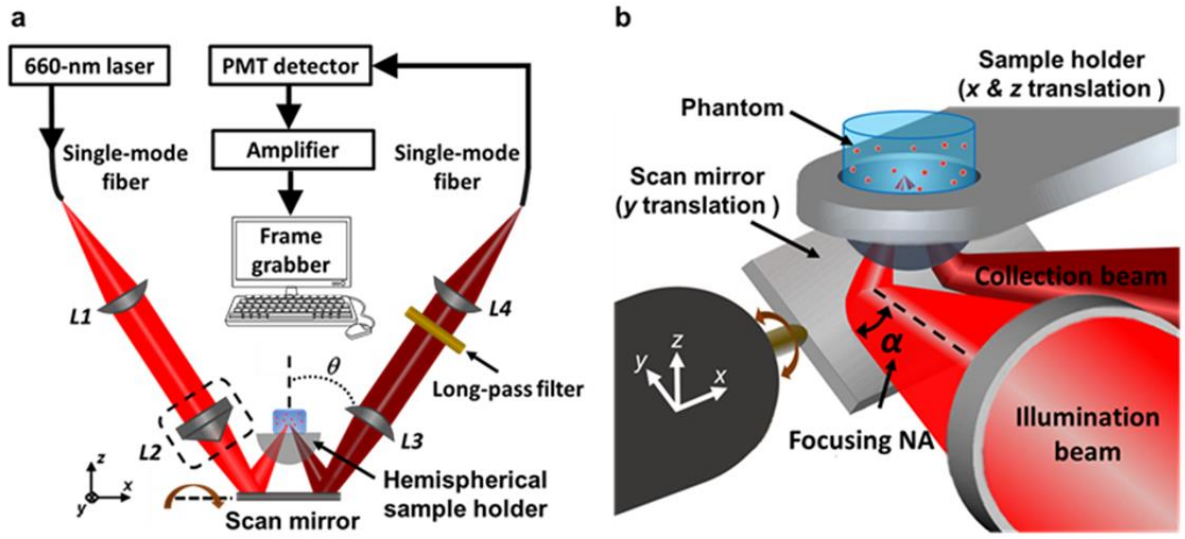

Figure 3.7. (a) The schematic of a point-scanned DAC microscope. The focusing element along the illumination path, *L2*, was either a standard aspheric focusing lens, or an axicon, which generated a Bessel beam. (b) Zoomed-in view of the DAC microscope near the sample. A galvanometric scanning mirror was used to scan the dual-axis beams along the *y* axis (1-kHz fast axis) while the sample holder was scanned along the *z* dimension for vertical imaging at 2 frames/sec. The sample holder was also scanned in the *x* dimension for 3D imaging. This figure was initially published in [34].

Figure 3.7 provided the schematic of a point-scanned fluorescence DAC microscope, which has previously been published in [84, 85]. The light source was a single-mode fiber-coupled diode laser at a wavelength of 660 nm (OBIS FP 660LX, Coherent, CA, USA). For illumination, the Gaussian point source of light emanating from the tip of a single-mode fiber ($1/e^2$ focusing NA (α) of 0.12) was collimated and focused into the sample without magnification at an angle, θ = 30 deg, with respect to the tissue's normal direction, through a pair of matched aspheric lenses, *L1* and *L2* (18.4-mm focal lengths, KGA280-B-MT, Newport Corporation, CA, USA). An axicon (AX2520-A, Thorlabs, NJ, USA) with a 20-degree base angle, as shown in the dash box in **Figure 3.7 (a)**, was utilized instead of the second aspheric lens (*L2*) in the illumination path to create a Bessel beam with nearly identical spatial resolutions as the Gaussian beam. Specimens were positioned on top of a hemispherical solid immersion lens (SIL, QU-HS-6, ISP Optics, NY, USA),

which provided index matching to allow the focused beams to enter the samples with minimal aberration and increases the NA of the beams by a factor of ~1.4 (index of fused silica) [84, 85]. Fluorescence signal from the specimen was collected off-axis (θ = 30 deg with respect to the tissue's normal direction), transmitted through a 664-nm long-pass fluorescence filter (LP02-664RU, Semrock, NY, USA) and coupled into a single-mode fiber, which served as the pinhole for spatially filtering (rejecting) the out-of-focus and multiply scattered light. The collection beam path utilized the same pair of aspheric lenses (*L1* = *L3* = *L4*) as the Gaussian illumination optics. A PMT detector (H7422-40, Hamamatsu, NJ, USA) in conjunction with a transimpedence amplifier (DHPCA-100, FEMTO, Berlin, Germany) converted the detected photons into a voltage signal. This voltage single was digitized and assembled into an image by a custom framegrabber written in LabVIEW (National Instruments, TX, USA) [84, 85].

This benchtop DAC microscope [34, 84, 85] performed vertical sectioning by utilizing a galvanometric mirror to scan both the illumination and collection beams in the *y*-direction at a rate of 1 kHz while a linear piezoelectric actuator was used to scan the specimens in the vertical direction (*z*) at a rate of 2 Hz, which defined the frame rate of the microscope (2 frames/second in the *y*-*z* plane). For volumetric microscopy, a motorized actuator was utilized to translate the sample holder in the third dimension (*x* direction). With the focusing angle (α = 0.12) and half beam-crossing angle (θ = 30 deg) utilized for this DAC microscope, the theoretical FWHM spatial resolutions were: Δx = 1.42 µm; Δy = 1.23 µm; Δz = 2.45 µm [34, 84, 85].

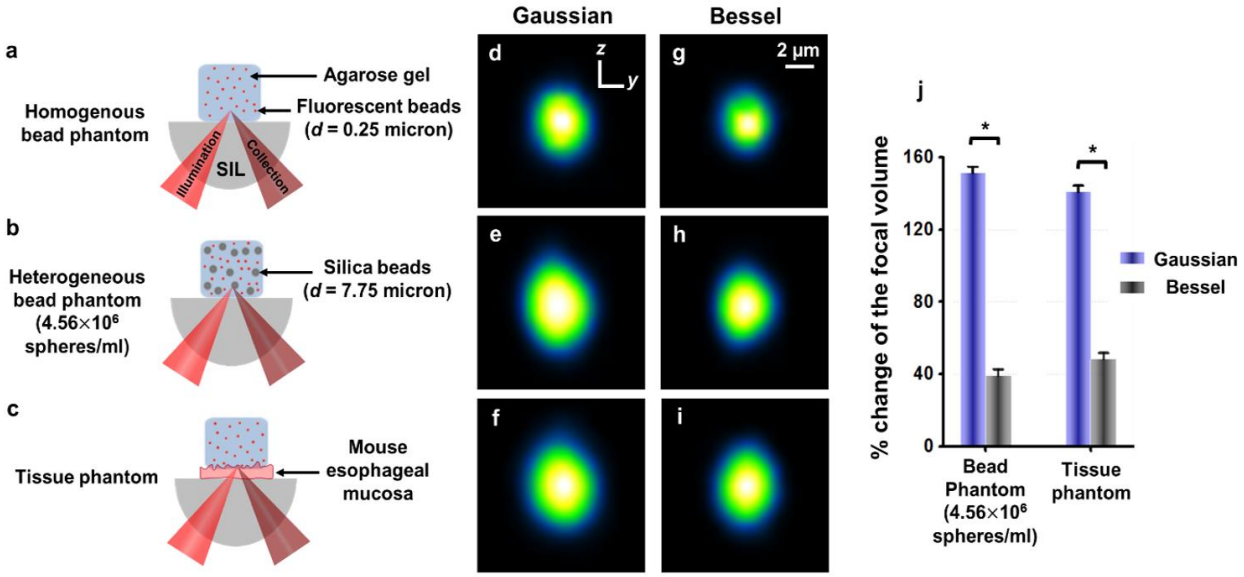

Figure 3.8. Panels (a)-(c) illustrated three different types of optical phantoms (homogenous fluorescent-bead phantom, heterogeneous silica-bead phantom, and fresh-tissue phantom) utilized for experimental PSF measurements. Panels (d)-(f) were self-normalized *y*-*z* cross sections of the average PSFs for a DAC microscope when imaging within these three phantoms using Gaussian illumination. Panels (g)-(i) were the corresponding average PSFs when using Bessel illumination. Panel (j) showed a plot of the degradation in the size of the focal volume for a DAC microscope when imaging within the heterogeneous silica-bead phantom and tissue phantom (compared to the unperturbed focal volume in the homogeneous phantom). * P-value < 0.001. This figure was originally published in [34].

Sub-resolution (0.25-μm diameter) fluorescent beads ($\lambda_{Ex/Em}$ = 660/680) were evenly distributed into a 2% w/v agarose solution to create a homogenous optical phantom (**Figure 3.8 (a)**) for the measurement of an unperturbed point-spread function (PSF) [34]. To quantify the effect of refractive heterogeneities on resolution, we developed silica-bead phantoms with a heterogeneous refractive-index distribution. These silica-bead phantoms (**Figure 3.8 (b)**) were prepared by mixing both the sub-micron fluorescent beads (targets for PSF measurements) at a concentration of 0.50% v/v, and monodisperse silica microspheres (7.75-μm diameter, 2.28×10^9 spheres per gram) at various concentrations within the agarose gel. The silica-bead concentration depicted in **Figure 3.8 (b)** ($\sim 4.56\times10^6$ spheres/ml) was the optimal concentration for mimicking the aberrating properties of fresh tissues. Finally, a tissue phantom was also fabricated (**Figure 3.8 (c)**) by placing a thin layer of fresh biological tissue (mouse esophageal mucosa, ~100 μm-thick)

before the homogeneous agarose phantom that contained sub-micron fluorescent beads for PSF measurements [34].

All phantoms (**Figures 3.8 (a) to (c)**) were imaged volumetrically, using a DAC microscope with Gaussian or Bessel illumination [34]. Vertical sections (*y*-*z*) were acquired and stored at 2 frames/second, while the specimen was translated in the third dimension (*x* direction) at a constant velocity to obtain serial sections separated by 0.7 μm. We sampled 25 discrete sub-resolution fluorescence beads in each volumetric imaging dataset to determine an average 3D PSF of the microscope. **Figure 3.8 (d)** to **(i)** displayed the vertical (*y*-*z*) cross-sections of the average 3D PSF of a DAC microscope when imaging within the fluorescent-bead phantom, silica-bead phantom, and fresh-tissue phantom, respectively. The overall resolution degradation was quantified as the percentage change in the volume ($v = \frac{4}{3}\pi \cdot \overline{\Delta x} \cdot \overline{\Delta y} \cdot \overline{\Delta z}$) of the measured PSFs when imaging within heterogeneous phantoms (**Figures 3.8 (b)** and **(c)**) compared to an unperturbed PSF when imaging within a homogenous phantom (**Figure 3.8 (a)**), where $\overline{\Delta x}$, $\overline{\Delta y}$ and $\overline{\Delta z}$ are the FWHM spatial dimensions of each average 3D PSF.

In addition to the phantom study, we performed *ex vivo* fluorescence DAC microscopy of mouse liver vasculature to compare the image resolution when using Gaussian vs. Bessel illumination. **Figure 3.9** displayed the average-intensity projections of a small z-stack of images (thickness = 5 μm) vs. a large z-stack of images (thickness = 50 μm) of mouse liver vasculature, acquired at a moderate depth of ~100 μm [34]. The average-intensity projection (**Figure 3.9**) showed the mean intensity from each vertical column of pixels in a 3D dataset and projected it as a 2D (*x*-*y*) image (the projection is in the *z*-direction). Even though the diffraction side lobes of a Bessel beam contributed out-of-focus background that deteriorates image contrast (signal-to-

background ratio), the image projections obtained with Bessel illumination (**Figures 3.9 (b)** and **(d)**) exhibited better resolution than the images obtained with Gaussian illumination (**Figures 3.9 (a)** and **(c)**), especially for the 50-µm thick image stack.

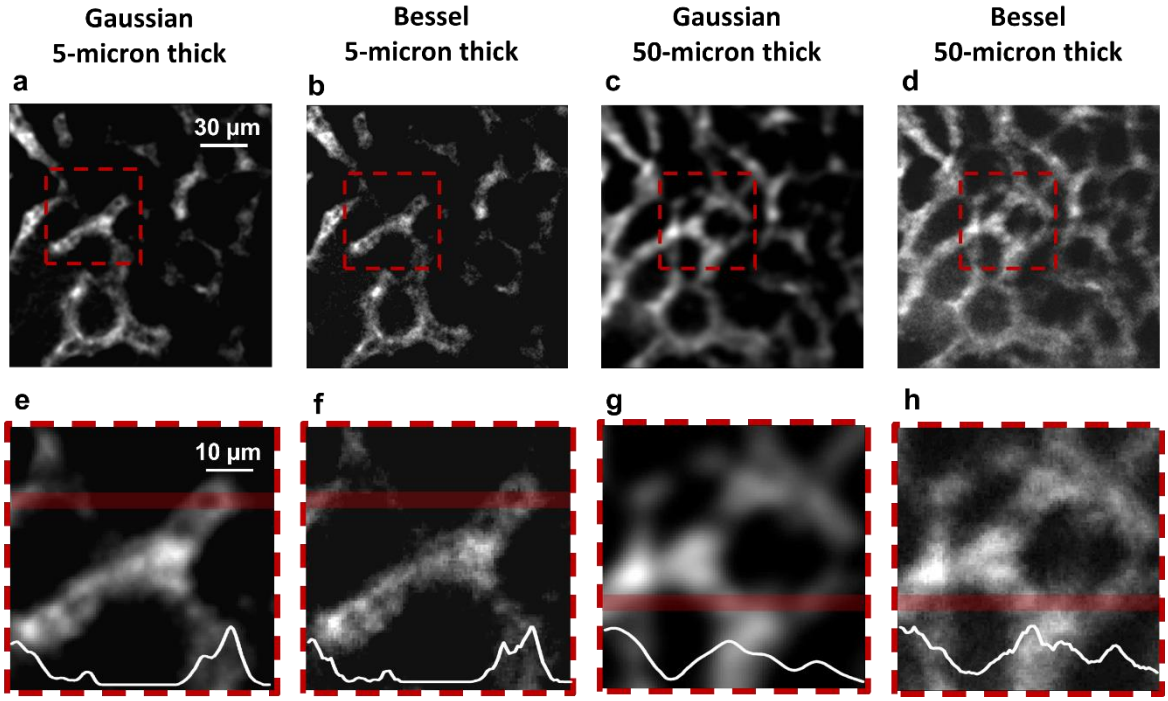

Figure 3.9. Panels (a) and (b) displayed average-intensity projections of a stack of DAC microscopy images of mouse liver vasculature, collected over a small range of depths: $z = 100 \pm 2.5$ µm. Panels (c) and (d) displayed the average-intensity projections of a stack of images collected over a moderate range of depths: $z = 100 \pm 25.0$ µm. Panels (a) and (c) were obtained with Gaussian illumination whereas panels (b) and (d) were obtained with Bessel illumination. The zoomed-in views of the regions outlined in (a)–(d) were presented in panels (e)–(h), respectively. Average line profiles from the highlighted region in (e)–(h) were shown at the bottom of each panel. This figure was originally published in [34].

Our hypothesis was that due to the superior propagation stability of a Bessel illumination beam, there was less random motion and uncertainty in the position of the focal volume as it is raster scanned in 3D within a thick tissue (to collect a volumetric image) [34]. As a result, the average-intensity depth projections were less blurred when using Bessel illumination compared to Gaussian illumination, in which the position of each image voxel is less stable (with respect to the position of other voxels) due to refractive beam steering. This hypothesis was validated through

optical simulations using a novel fractal propagation method (FPM) that was recently developed by us [129]. It has been shown that the FPM could accurately and efficiently model scattering, diffraction and refractive aberrations in three dimensions, as was relevant for optical microscopy of tissues [129]. The FPM was used to simulate a focused Gaussian or Bessel beam propagating in a realistic tissue with refractive heterogeneities.

These simulations were performed using the same parameters as the *ex vivo* imaging experiments, where λ = 661 nm, and the diffraction-limited FWHM resolution of the focused Gaussian and Bessel beams was 1.42 µm (**Figures 3.10 (a)** and **(d)**). Individual irradiance profiles of focused Gaussian and Bessel beams were simulated over a range of focal depths within a fractal medium (a realistic model of mouse liver tissue). We then calculated the average Gaussian and Bessel beam irradiance profiles over a range of focal depths, either from approximately 100 ± 2.5 µm (**Figures 3.10 (b)** and **(e)**), or from approximately 100 ± 25 µm (**Figures 3.10 (c)** and **(f)**). **Figure 3.10** showed the self-normalized irradiance profile of a diffraction-limited beam focus (in a homogeneous medium), as well as the average-intensity projections for a single focused Gaussian or Bessel beam propagating through simulated mouse liver tissue. The focus of a Gaussian beam in tissue demonstrated more severe resolution degradation (**Figure 3.10 (b)**) and beam steering (**Figure 3.10 (c)**) than the main lobe of a focused Bessel beam (**Figures 3.10 (e)** and **(f)**). These simulations were similar to the experimental DAC images (**Figure 3.9**) in showing that averaging the irradiance profiles of a Gaussian beam focus over a large range of focal depths (50 µm) caused significant broadening of the profile due to distortion as well as the accumulated beam steering effects. However, the main lobe of a Bessel beam was less sensitive to such effects.

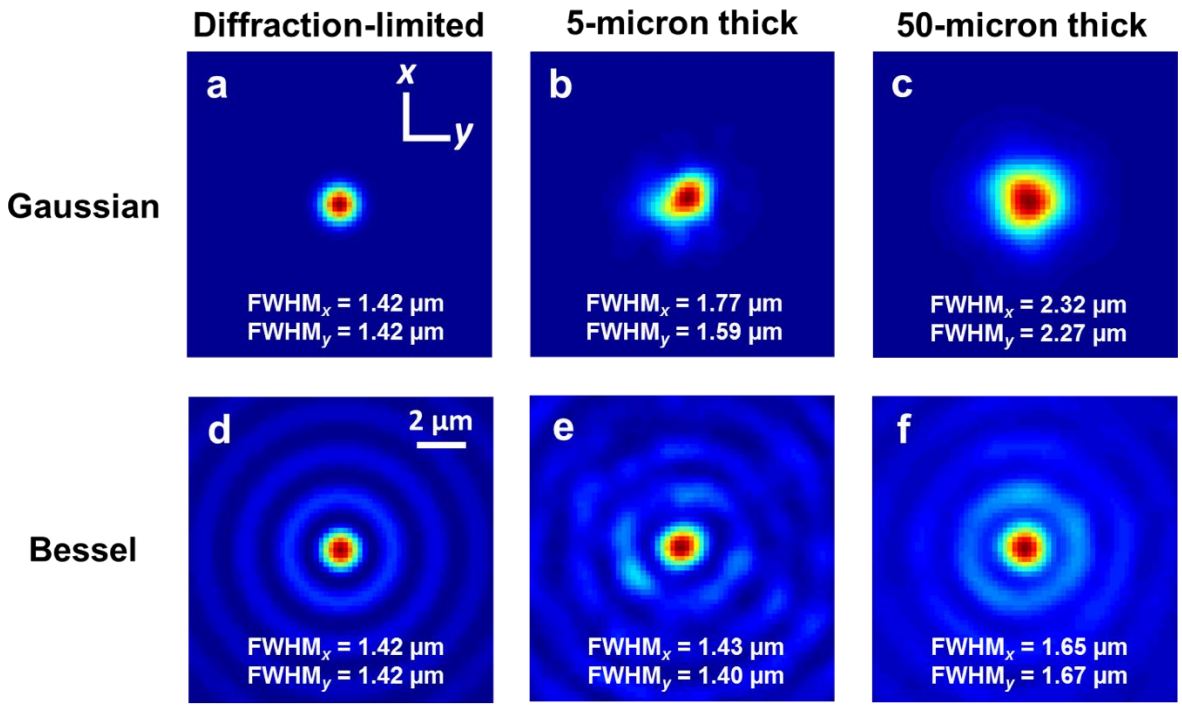

Figure 3.10. The self-normalized irradiance profiles of simulated Gaussian and Bessel beam foci. Panels (a) and (d) were the profiles of diffraction-limited beam foci (Gaussian and Bessel, respectively). Panels (b) and (e) were average-intensity projections, over a limited range of depths (z = 100 ± 2.5-µm deep), of the irradiance profiles of a focused Gaussian and Bessel beam, respectively. Panels (c) and (f) were average-intensity projections, over a larger range of depths (z = 100 ± 25.0-µm deep), of the irradiance profiles of a focused Gaussian and Bessel beam, respectively. Due to greater beam steering and distortion of the Gaussian beam as it propagates in tissue, the Gaussian beam focus was significantly enlarged when viewing a 50-µm thick average-intensity projection vs. a 5-µm thick average-intensity projection of the irradiance profiles. This figure was originally published in [34].

Previous studies (Chapter 2) have shown that the DAC microscope configuration provides superior optical-sectioning contrast (SBR) compared to conventional single-axis confocal microscopes when imaging within homogeneous scattering media [91, 92]. However, biological tissues often contain refractive heterogeneities at sub-micron to mesoscopic scales, which cause beam steering and aberrations that can reduce the resolution and sensitivity of all laser-scanning microscopes, and DAC microscopes in particular [95, 127, 128]. This study [34] focused on quantifying the degradation in resolution that occurred when performing DAC microscopy within realistic phantoms and fresh tissues using either Gaussian or Bessel beam illumination. Preliminary experiments (Chapter 3.2) have demonstrated that Bessel illumination was superior for

maintaining pointing accuracy and beam quality in realistic tissues [30]. This study further demonstrated that these characteristics of Bessel beams make them particularly beneficial for DAC microscopy, where the positional stability and high beam quality were critical for its unique off-axis illumination and collection architecture that required two beams to intersect precisely at their foci [34]. A trade-off that must be noted, as shown in the *ex vivo* images, was that the diffraction side lobes of a Bessel beam contribute out-of-focus background that reduced image contrast (signal-to-background ratio). Future study will have to focus on balancing this trade-off and achieving an optimal balance between image contrast and resolution for various biomedical applications of DAC microscopy [34].

Chapter 4. RAPID PATHOLOGY OF LUMPECTOMY MARGINS WITH AN OPEN-TOP LIGHT-SHEET (OTLS) MICROSCOPE

4.1 MOTIVATION

As mentioned in Chapter 1.2, according to a recent report, approximately 268,600 new cases of invasive breast cancer are expected to be diagnosed within the United States in 2019, along with 62,930 new cases of non-invasive (*in situ*) breast cancer [130]. For these patients who are diagnosed with early-stage invasive breast cancer or carcinoma *in situ* every year, breast-conserving surgery (BCS), also called lumpectomy or partial (segmental) mastectomy, is a standard intervention [47, 48]. It has been demonstrated that the overall or disease-free survival rates between patients treated with whole-breast mastectomy vs. BCS with postoperative radiation are comparable [49, 50]. However, about 20% to 60% of the patients still undergo additional surgery when post-operative histopathology confirms that the resection margins are positive for tumor [53-55]. Re-excision surgeries are costly, inconvenient for patients, may lead to poor aesthetic results, as well as result in delayed adjuvant therapies with inferior patient outcomes [53-55, 81].

After surgery, excised specimens submitted for post-operative histopathological examination are first grossly prepared as 3- to 5-mm thick serial slices, from which suspicious regions are further processed into FFPE blocks [81, 131]. In current practice, a 4-μm-thick histology section is obtained from each tissue block and mounted on a glass slide, where each slide displays a cross-section of the specimen from the inked margin surface down towards the core of the sample (**Figures 4.1 and 4.2**) [81, 131].

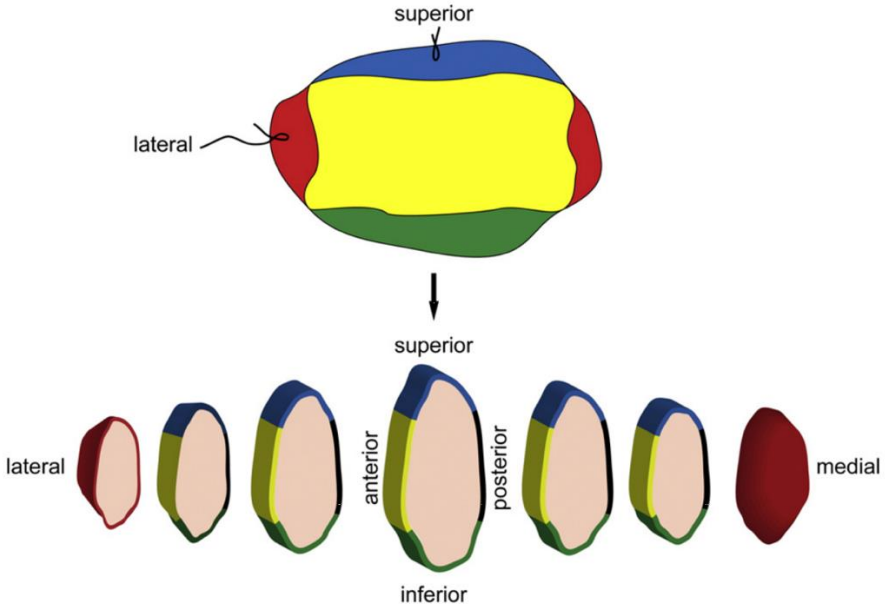

Figure 4.1. The orientation of a lumpectomy specimen can be identified through the use of two sutures and five different painting colors (anterior, yellow; posterior (deep), black; superior, blue; inferior, green; medial and lateral, red) [131].

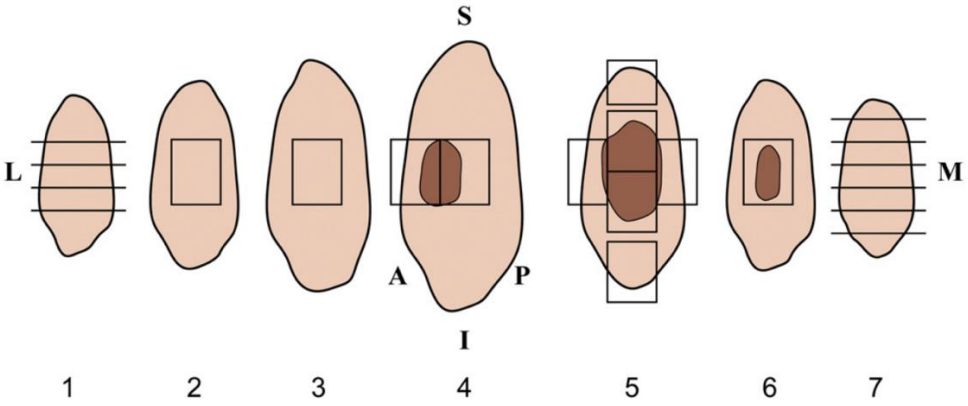

Figure 4.2. The sampling criterion of a lumpectomy specimen. If the specimen is too large to be placed into a cassette in its entirety, the largest cross section of the tumor should be submitted for further processing. In addition, according to this study[131], tissues adjacent to the tumor and at least one cross section of each margin should be submitted for microscopic examination. For close margins, multiple cross sections can be submitted. For the medial and lateral slices, cross sections should be cut perpendicularly to the inked surfaces for the assessment of the surgical margins. Here, the rectangular boxes present the sections. L indicates lateral; M, medial; S, superior; I, inferior; A, anterior; P, posterior (deep) [131].

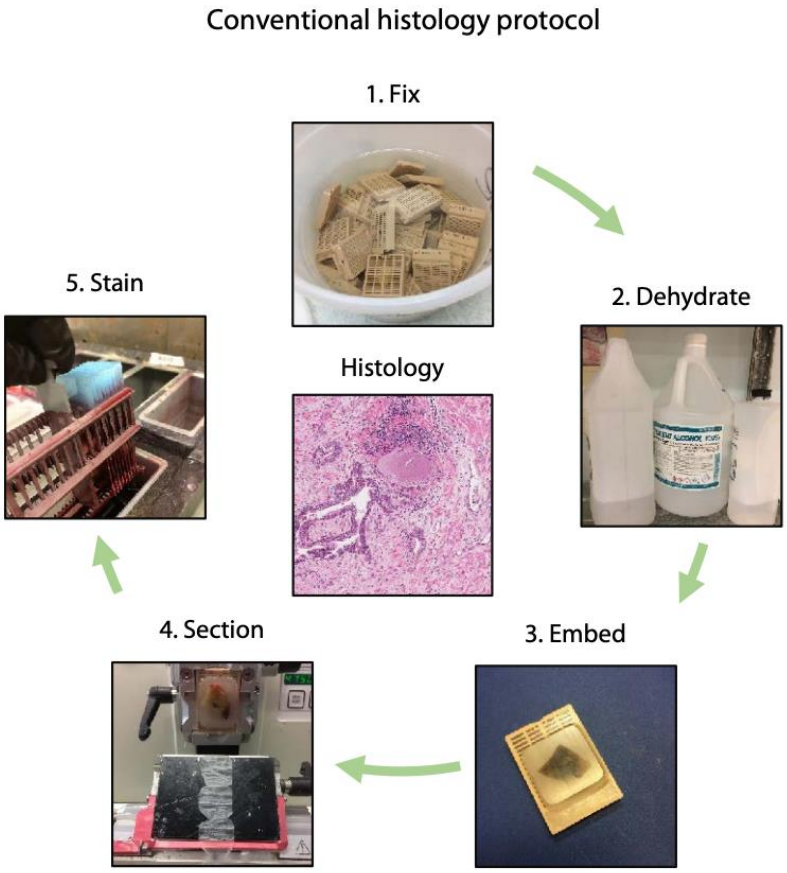

Figure 4.3. Conventional histology protocol. This figures was published in [46].

Over the past century, histopathology has remained as the "gold standard" for the diagnosis of diseases [65-69]. Microscopic observation of micron-scale features from thin-sectioned tissues mounting on glass slides has been widely accepted by the medical community as the most reliable method for examining tissue biopsies and surgically excised specimens [65-69, 81]. Unfortunately, specimen preparation for conventional histopathology has been time-consuming and labor-intensive (**Figure 4.3**), which requires: 1) fixing specimens, 2) embedding specimens in paraffin, 3) sectioning tissues with a microtome or cryotome, 4) elaborating protocols for dehydrating, blocking, or staining the tissues [46]. Artifacts that are being introduced during these heavy tissue processing procedures may include specimen degradation, shrinkage, or destructiveness of

molecular and genomic components [46]. These artifacts may impair morphological or molecular interpretation, and thereby compromise the precision and accuracy of histopathologic diagnosis [46]. Another major limitation facing conventional histopathology is the sampling error caused by selective imaging of thin sections within a large tissue specimen. For example, it has been estimated that < 1% of the margin surface is being examined by conventional pathology [65, 66]. Wide-area *en face* (horizontal) imaging of the surgical margin surface may eliminate these sampling errors and improve the sensitivity of tumor detection at the margin surfaces of a specimen.

4.2 ALTERNATIVE APPROACHES FOR INTRAOPERATIVE LUMPECTOMY GUIDANCE

As discussed in our recent publication [81], frozen section histology, which becomes a rapid intraoperative alternative to slow post-operative histology, may be performed to guide certain tumor-removal procedures [53, 70, 71]. However, frozen section histology is not ideal for breast tissues due to their high lipid content, which causes significant artifacts [62, 70, 71, 132-134]. In addition, because of the technical challenges of preparing adequate numbers of frozen sections within an acceptable intraoperative time frame (< 30 minutes [135]), frozen section histology suffers from more-severe sampling limitations than post-operative slide-based histology. Finally, frozen sectioning leads to tissue destruction that can negatively affect the accuracy of post-operative archival pathology [46, 81]. Alternative technologies (**Table 4.1**) for nondestructive intraoperative lumpectomy guidance include touch preparation cytology [72, 73], ultrasound [74-76], specimen radiography [77, 78], radiofrequency spectroscopy [79, 80], optical coherence tomography [16], photoacoustics [136], confocal/nonlinear microscopy [6, 40, 41], SIM [44, 45, 137], microscopy with UV surface excitation (MUSE) [42, 43, 138-140], and molecular imaging

with topically applied agents [141-144]. Although many of these methods are in various stages of research development or clinical adoption (such as ultrasound and specimen X-ray), the reliability of these tools typically falls short of gold-standard histology due to various factors such as limited spatial resolution, surface sampling, and contrast [81].

Table 4.1. Some of current solutions for intraoperative guidance of lumpectomy.

	Advantages	Disadvantages	References
Frozen section histology	Provides rapid pathology	Sampling error; tissue destruction (especially for lipid content)	[53, 70, 71]
Touch preparation cytology	Provides reliable cellular details	Limited utility with fibrous lesions; loss of tissue that may limit ancillary testing	[72, 73]
Specimen radiography	Provides large penetration depth	2D interpretation; very limited information about soft tissues	[77, 78]
Radiofrequency spectroscopy	Ease-of-use	Limited resolution & sensitivity	[79, 80]

4.3 ADVANTAGES OF OTLS MICROSCOPY

We have discussed the advantages of exploiting OTLS microscopy to image fresh clinical specimens in our recent publications [46, 81].

Amongst the alternative methods described in Chapter 4.2, optical-sectioning microscopy offers the potential for robust and rapid microscopic inspection of lumpectomy margins that approaches the image quality of gold-standard histology without requiring destructive physical sectioning [80]. While early systems and studies suffered from limited fields of view (< 1 x 1 mm) [145-148], in recent decades, wide-area imaging of large surgically excised specimens has been achieved with a variety of optical-sectioning techniques such as confocal microscopy [6, 7, 110, 149], nonlinear microscopy [10, 40, 150], SIM [15, 44, 151-153], and MUSE [42, 43, 138-140]. Confocal and nonlinear microscopy systems have limited imaging speed since they often require a tightly focused laser beam to be raster scanned in two-dimensions over a large tissue surface [81]. SIM and MUSE can rapidly obtain 2D images of tissue surfaces with a detector array and are relatively cost-effective technologies compared with confocal and nonlinear microscopy [81]. However, image contrast is dependent upon the axial optical-sectioning thickness of these technologies (SIM and MUSE), which is tunable with SIM but tissue-dependent with MUSE (~10 to 25 μm according to previous reports [42]).

Besides, a major limitation for these 2D optical imaging techniques is the use of a single-axis configuration for both illumination and collection. For such a configuration, high-NA optics are necessary to achieve sub-nuclear resolution (1-2 μm), but this results in a narrow depth of focus (<5 μm) [81]. The narrow depth of focus can be an impediment for rapid imaging of freshly cut tissue specimens, where surface irregularities cause defocusing throughout the imaging field (**Figure 4.4**) [46, 81]. Although specimens can be flattened, another technical challenge is to align

the tissue surface to be perfectly parallel to the focal plane of the microscope [46, 81, 152, 154]. Elaborate flattening and alignment techniques are possible to mitigate the effects of these surface irregularities and sample-tilt issues [152, 154]. However, they are logistically difficult and time-consuming for pathologists to implement in routine practice [152, 154]. In reality, it is also difficult to completely clean up tissue debris that can obscure the margin surface [42, 46, 81]. These challenges may ultimately hamper the clinical translation of these optical imaging techniques based on single-axis illumination and collection [46, 81]. To overcome these limitations, the illumination and collection paths may be separated to form a confocal-theta or a light-sheet microscope (LSM) with an extended depth of focus based on a low-NA illumination [155].

When image freshly excised tissues, this extended depth of focus (due to low-NA illumination) of a scanning LSM system allows for in-focus imaging of the irregular tissue surface over large field of view. As a result, it is possible to continuously obtain depth-resolved *en face* images of the whole tissue surface [46, 81]. While there have been limited investigations into the feasibility of using LSM to image thick and highly-scattered samples, previous simulation study [155] has shown that LSM can provide high-contrast images up to an imaging depth of about 50 micron, which is equivalent to about 12 physical histology sections (4-micron thick per tissue section). This volumetric information obtained at superficial depths may be useful for certain biomedical applications, such as pathologic assessment of surgical margins or rapid cancer triaging [46].

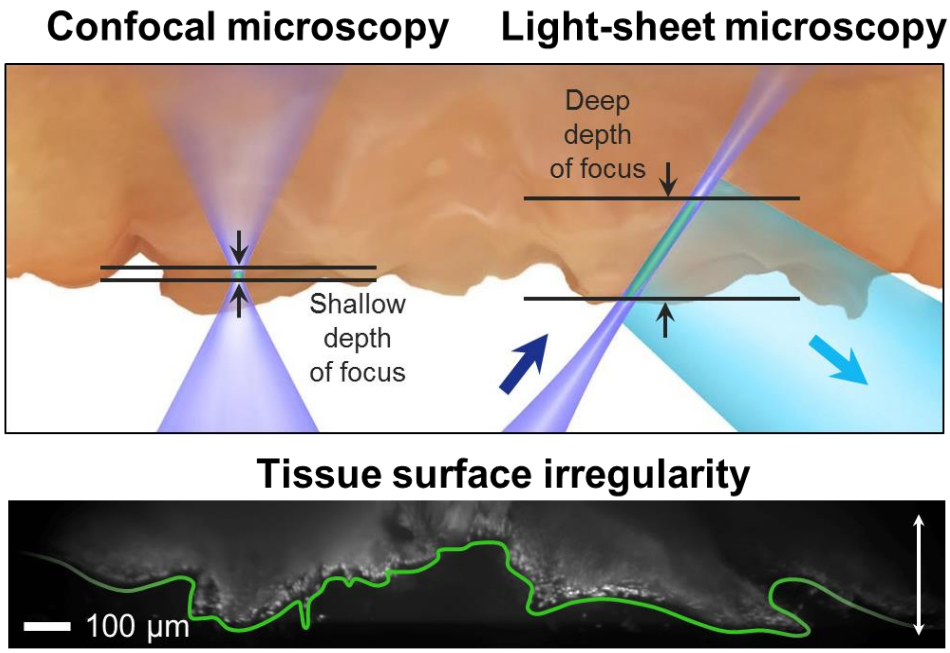

Figure 4.4. The depth of focus of a conventional confocal microscope vs. a light-sheet microscope. With LSM, a 3D volume was imaged by scanning the tissue in one 1 dimension. One advantage of this was that an irregular tissue surface may be digitally flattened or "segmented out" without elaborate mechanical tissue-flattening and alignment mechanisms [46].

4.4 AN OTLS MICROSCOPE OPTIMIZED FOR RAPID DUAL-CHANNEL FLUORESCENCE IMAGING

In an attempt to overcome some of the technical challenges encountered by previous microscopy systems (Chapter 4.3), we have developed an OTLS microscopy system for rapid, wide-area, microscopic imaging of large clinical specimens [46, 81].

In general, light-sheet microscopy achieves optical sectioning by employing thin "selective" illumination of tissues and orthogonal collection of fluorescence signal [12, 13, 125, 156-158]. However, previous light-sheet microscopy systems were designed to image small model organisms rather than to accommodate large specimens of arbitrary geometry [12, 13, 125, 156-

161]. While conventional LSM systems utilize a “horizontal-orthogonal” illumination and collection arrangement for imaging relatively transparent samples sitting in a cylindrical sample holder, we have exploited a 45 degree “tilted” or “oblique” arrangement [162-164] that achieves light-sheet imaging of turbid samples sitting on a flat glass sample holder [46, 81]. Such an arrangement is similar to the inverted selective plane illumination microscope (iSPIM [162]) but differs in that the illumination and collection optics are located underneath of the sample holder [46, 81]. This "open-top" architecture can be useful for imaging large clinical samples [46, 81, 160]. However, as described by McGorty *et al.*, the open-top geometry still introduced several challenges, as the illumination and collection optics were no longer directly index-matched into the tissue sample through air or water-immersion [160].

Based on our experience in designing DAC microscopy (Chapter 2), we have developed a wavefront- and index-matching unit for the OTLS microscope. In brief, this unit consisted of a hemispherical lens (i.e. solid immersion lens, SIL [84, 85]) and an index-matched oil layer to allow for aberration-free imaging. The SIL provided wavefront matching of an illumination and collection beam as they transitioned from air into the higher-index material of the SIL (fused silica, n ~ 1.46). The two beams were then index matched into the tissue sample through a thin oil film (n ~ 1.46), followed by a fused silica plate (n ~ 1.46) on which the sample was placed. Altogether, this unique open-top configuration can be convenient for clinical use with essentially no constraints on specimen geometry [46, 81].

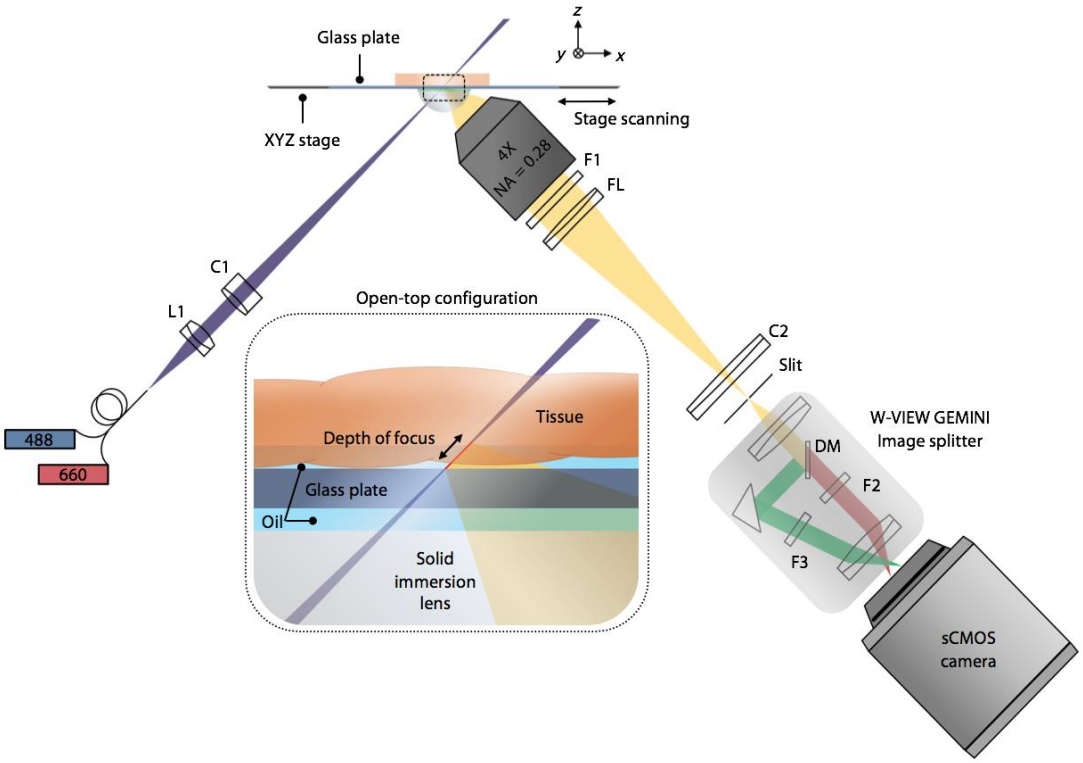

Figure 4.5. Schematic of an open-top light-sheet (OTLS) microscope. The OTLS microscope utilized a solid immersion lens (SIL) and thin oil film to provide wavefront- and index-matching of the illumination and collection beam paths into tissue at a 45-deg angle of incidence. This unique open-top configuration (inset) was versatile for imaging diverse clinical specimens with minimal constraints on size and geometry. The 0.03 illumination NA provided an extended depth of focus (~ 400 μm) to accommodate for tissue-surface irregularities, specimen tilt, and tissue debris. This image was published in [81].

The optical schematic of an OTLS microscope were shown in **Figure 4.5** [81]. The microscope design has been published in [46, 81]. Reprint permission has been obtained from the publisher. Illumination was provided by two fiber-coupled diode lasers (Coherent, OBIS^{TM} Laser System) at 488 nm and 660 nm, which were combined into one single-mode optical fiber ($1/e^2$ focusing NA = 0.12, Core Diameter = 2.5 μm) and collimated using lens, *L1* (*f* = 25 mm). The collimated beam transmitted through a cylindrical lens, *C1* (NA = 0.03), creating a 2-mm-wide light-sheet ($1/e^2$) with a FWHM thickness of ~7 μm at the beam waist. This was the diffraction-limited FWHM resolution in the worst dimension (along the collection axis) of the OTLS

microscope at 660 nm. The 0.03 illumination NA has provided the OTLS system with a depth-of-focus (confocal parameter, $2Z_R$) of ~ 400 µm. This depth-of-focus (~ 400 µm) has provided our OTLS microscope with the versatility to image diverse clinical specimens that have various degrees of pliability and surface irregularity.

As mentioned at the beginning, the OTLS system was equipped with a novel specimen interface (Fig. 1 inset) [46, 81], which was comprised of a 7.5-mm-radius fused-silica solid immersion lens (SIL, BMW Optics, n =1.46), a 0.5-mm thick oil layer (Cargille Labs, Cat.No:19571), and a 1-mm-thick fused-silica glass plate, which served as the sample holder (ESCO Optics, 10×10 cm^2). When performing scanned imaging of the specimen, the thin oil layer at the top surface of the SIL, which did not evaporate, provided an index-matched interface between the stationary SIL and the horizontally translated glass-plate sample holder. Both of the illumination and collection beams were positioned below the glass-plate sample holder, allowing the OTLS microscope to accommodate human tissues of arbitrary size and thickness without physically interfering with the illumination and collection optics. The custom SIL (with a radius of 7.5 mm) was truncated with a reduced center thickness of 6 mm such that the beam waist (optimal focus) of both light beams was located right above the glass plate. Tissue specimens were placed on the glass-plate sample holder along with a thin layer of index-matching oil to prevent the specimens from drying out and also to improve the index matching between the glass plate and the tissue surface [46, 81].

Fluorescence emission was collected using a 4× objective lens, *L2* (f_{L2} = 43.47 mm, NA = 0.28), filtered through an emission filter, *F1* (Semrock, FF01-496/LP-25), and focused using a tube lens, *FL* (f_{FL} = 150 mm). A dual-channel image-splitting module (Hamamatsu, W-VIEW GEMINI) was used to focus the two fluorescent channels onto two halves of a high-speed scientific

complementary metal-oxide–semiconductor (sCMOS) camera chip (PCO, pco.edge 4.2). To avoid spectral cross-talk between the two image channels (SYBR Gold and ATTO 655 NHS ester), the image-splitting module contained a dichroic mirror, *DM* (Semrock, Di03-R594-t1-25×36), and two separate emission filters, *F2* and *F3* (Semrock, FF01-685/LP-25 and SP01-561RU-25). A low-power cylindrical lens, *C2* (*f* = 2000 mm) was placed before the camera to provide final correction for astigmatism induced by a slight refractive-index mismatch at the oil-tissue interface. There was a total of 5× magnification between the specimen and the camera ($1.46 \times f_{FL}/f_{L2} = 5$), in which the SIL provided an additional magnification factor that was equivalent to its refractive index of ~1.46 [84, 85].

The collection objective (Olympus, XLFLUOR 4×, NA = 0.28) provided a practical field of view of ~ 1.25 mm and a measured lateral resolution (within the plane of the illumination light-sheet) of ~ 2.0 μm. As the illumination light sheet was scanned through the sample, a series of dual-channel light-sheet images were captured at an oblique 45-degree angle with an image width, *w*, and adjustable image height, *h* (**Figures 4.6 (a)** and **(b)**). The image width was limited by the 1.25-mm field of view of the detection objective (**Figure 4.6 (b)**). The combined dual-channel image height (**Figure 4.6 (a)**) recorded by the camera was 128 vertical camera pixels tall (64 pixels per channel, which is ~ 80 μm in tissues). This reduced crop size was chosen to maximize the imaging speed while still accommodating for any tissue irregularities/tilt/debris at the surfaces of the lumpectomy specimens. As shown in **Figure 4.6 (b)**, the distance between images along the scan dimension, *x*, was set as 1.25 μm, which matched the sampling density of the sCMOS camera in the *y* and *h* directions (1.25 μm per pixel).

The optimized image acquisition and processing pipeline of an OTLS microscope has been published in [81]. Adjacent volumetric OTLS image strips (1.25-mm wide), as shown in **Figure**

4.6 (b), were acquired in succession (with 1-mm spacing) using a serpentine scanning pattern to cover the entire surface of each specimen up to a maximum size of ~10×10 cm^2 with a high-speed motorized stage (Thorlabs, MLS-203-1). For a raw image size of 1000 pixels (width) by 128 pixels (height), along with a 500-μs camera exposure time, the highest imaging speed of the system was about 1.5 cm^2/minute. In this study, the dual-channel raw image frames (1000 pixels by 128 pixels in 16-bit TIFF formats) were acquired at a streaming rate of 1000 pixels × 128 pixels × 2.0 Byte × 2000 fps = 0.51 GB/s to a dedicated workstation containing a high-speed Redundant Array of Independent Disks (RAID) 0 controller with a PCI CameraLink interface. To synchronize the stage-scanning mechanism with the image acquisition, a custom LABVIEW program was developed.

In an initial LABVIEW design, raw image frames (1000 pixels by 128 pixels) were first buffered to the computer memory as a 1D array (with a total of 128,000 pixels). This 1D array was then reshaped into a 2D array for real-time image display. However, when using the NI Vision Development Module (NI-IMAQ Write File) to write each 2D array to disk as a TIFF file, the write speed was limited to ~ 0.25 GB/s due to the overhead involved in creating, opening, and closing each TIFF file. This slow process was not suitable for time-limited applications, such as intraoperative guidance. To overcome this limitation, the Technical Data Management Streaming (TDMS) file format (National Instruments) was utilized for high-speed data streaming in LABVIEW. In summary, after buffering each raw light-sheet image to the computer memory as a 1D array and reshaping this buffer into a 2D array for real-time image display, consecutive 2D arrays were concatenated into a pre-initialized TDMS 3D data cube. At the end of each volumetric image strip (*x*- direction scan of the sample with respect to the light sheet, as shown in **Figure 4.6**

(b)), this TDMS file (3D data cube) was saved to disk all at once, which allowed us to maintain the full data streaming speed of 0.51 GB/s.

Our light-sheet images were obtained at an oblique 45-deg angle of incidence with respect to the specimen surface. However, when stored digitally, these images were arranged as a rectangular data cube. Therefore, to restore the correct tissue geometry, the data cubes must be sheared by 45 deg in the x-z plane to create a trapezoidal data volume (**Figure 4.6 (c)**). A custom Python code was written to convert the TDMS file into TIFF images as well as to perform the image shearing.

After shearing, an extended-depth of field (EDF) algorithm [165] was applied in ImageJ to the cytoplasmic channel, which exhibited more-complete surface staining compared with the nuclear channel, to extract the “best-focus" surface (i.e. tissue surface) from each 3D image strip. Once the “best-focus" surface was defined, both of nuclear and cytoplasmic channels at this surface were then used in a false-coloring algorithm to mimic H&E histology. This custom false-coloring code was a modified version of an algorithm described in a recent publication [166] (**Figure 4.6 (d)**). Adjacent pseudo-colored image strips were then registered and stitched to adjacent image strips using the ImageJ grid-stitching algorithm [167] (**Figure 4.6 (e)**).

The total image processing time (from image-shearing to false-coloring) for a 1-cm by 1-cm sample (~20.4 GB of data) was ~15 min. Since this was not ideal for time-limited clinical applications, we have been working on optimizing our image processing code, including the use of GPUs. It should also be noted that if the “best-focus" surface of the tissue has been defined prior to image processing, only a few minutes was required to fully process the OTLS images at one imaging depth.

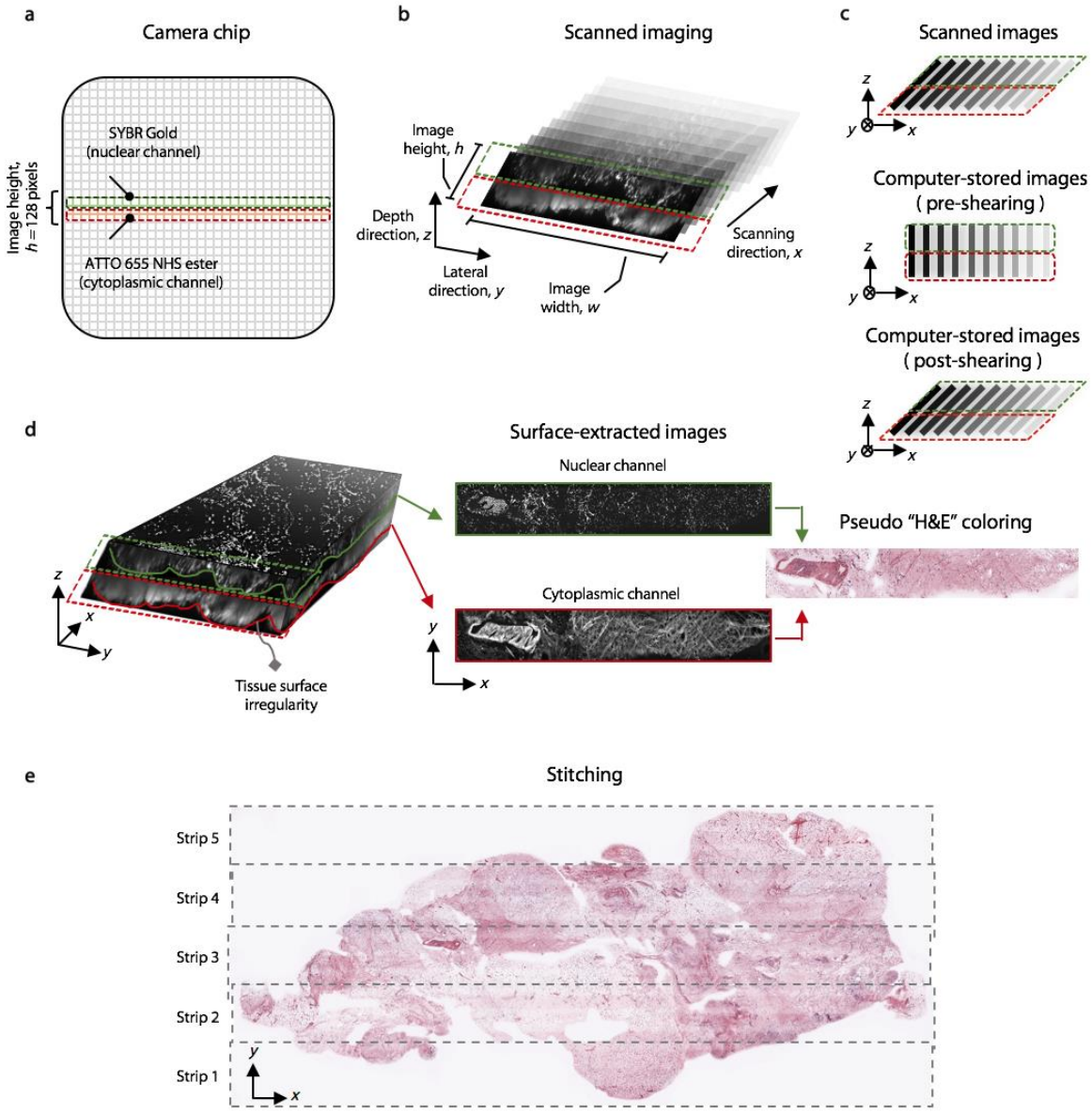

Figure 4.6. The image acquisition and processing pipeline of OTLS microscopy published in [81]. (a) The dual-channel (nuclear and cytoplasmic channel) OTLS images occupied a combined height (*h*) of 128 vertical camera pixels (64 pixels per channel, or ~ 80 µm in tissues). The image height, *h* = 128 pixels, was adjustable and selected in this case to optimize the image speed while accommodating for surface irregularities, specimen tilt, and tissue debris. (b) Oblique (45-deg) light-sheet images were captured in succession at a sampling pitch of 1.25 µm along the primary tissue-scanning direction, *x*. The horizontal dimension of each image strip was *w* = 1.25 mm. (c) The raw light-sheet images were initially stored in a rectangular data cube. During post-processing, this data cube was sheared by 45 deg in the *x*-*z* plane to transform the data cube into a trapezoidal data volume, which accurately represented the geometry of the imaged tissue volume. (d) An extended-depth-of-field (EDF) algorithm [165] was applied to extract the irregular surface of the specimen. The two-channel surface-extracted image was then false-colored to resemble H&E histology using an algorithm modified from a recent publication [166]. (e) After false-color processing, adjacent image strips were registered and stitched using an ImageJ grid-stitching algorithm [167].

4.5 AN INNOVATIVE TWO-COLOR FLUORESCENT ANALOG OF H&E STAINING

In our preliminary study, an initial publication demonstrated the basic feasibility of achieving rapid intraoperative pathology of the surfaces of freshly excised specimens with OTLS microscopy, using a single-channel acridine orange stain [46]. In the same study, we have exploited a fluorescent analog of H&E staining for fixed biopsy samples, consisting of DRAQ5 as a fluorescent analog of hematoxylin (excited at 660 nm) and eosin, which naturally fluoresces under 488-nm excitation [46]. While this "D&E" staining method allowed for dual-channel fluorescence imaging that could be false-colored to mimic gold-standard H&E-stained tissue sections, it only performed well for staining fixed, dehydrated samples [46]. Our group and others [10, 46, 150, 168] have found that when staining fresh, hydrated specimens, eosin leaked out of the tissue during imaging due to poor binding to tissue structures, which created an unwanted background signal that limits image contrast.

Our study of developing an innovative two-color fluorescent analog of H&E staining has been published in [81]. Reprint permission has been obtained from the publisher. SYBR Gold ($\lambda_{Ex}/_{Em}$ = 495/537, Thermo Fisher, Cat. No: S11494) was utilized as the nuclear stain while ATTO 655 NHS ester ($\lambda_{Ex}/_{Em}$ = 655/680, Sigma-Aldrich, Cat. No: 76245) was utilized as an eosin-mimicking cytoplasmic/stromal stain. SYBR Gold labels dsDNA, ssDNA and RNA in both fresh and fixed tissues [169]. NHS esters have been widely-used amine-reactive functional groups for covalent labeling of primary amines [170] and have been commonly used to conjugate antibodies to fluorophores and nanoparticles [171-174]. We hypothesized that an NHS-ester-functionalized fluorophore could be used as a more robust fluorescent analog to eosin, which also stained cytoplasmic proteins indiscriminately, but tended to leach out due to weak noncovalent binding. An additional benefit of this approach has been that since many commercially available

fluorophores have been available as NHS esters, it has been straightforward to select fluorophores that can avoid spectral cross-talk for dual-channel fluorescence imaging, such as SYBR Gold and ATTO 655.

The following parameters have been optimized to achieve high-contrast OTLS images of lumpectomy margins with the SYBR Gold and ATTO 655 NHS ester stain (**Figures 4.7, 4.8 and 4.9**): (1) pH of the staining solution (from pH = 6.5 to pH = 9.5), which has been known to affect the reactivity of NHS ester [170]; (2) staining concentration (from 100 nM to 10 μM), which can affect imaging sensitivity/speed; and (3) rinsing duration (from 30 sec to 120 sec), which can affect image contrast (signal-to-background ratio). As a control experiment (**Figures 4.10)**, hydrolyzed (inactivated) ATTO 655 NHS ester was applied to tissue surfaces to verify that the image contrast provided by reactive (non-hydrolyzed) ATTO 655 NHS ester was due to covalent labeling rather than non-covalent binding of the dye to the specimen. In this study, our optimized 2.5-minute tissue-staining and rinsing protocol utilized a cocktail containing a 1:15,000 v/v dilution of SYBR Gold and 1 μM ATTO 655 NHS ester in 1× Phosphate-Buffered Saline (PBS, Gibco, Cat. No: 10010023) at pH 8.0 to stain fresh tissue surfaces for 1 minute, followed by three 30-sec rinse steps in 1× PBS at pH 7.4.

Figure 4.11 showed a comparison of the image quality between OTLS microscopy of eosin-stained vs. ATTO 655 NHS-ester-stained fresh breast tissues. The purple arrowhead in **Figures 4.11 (a)** indicated that eosin was weakly bound within fresh, unfixed breast tissues, which caused the eosin to leak out even after multiple rinse steps. This phenomenon has been seen in other reports in the past [10, 46, 150, 168]. Various tissue structures selected from **Figures 4.10 (a)** and **(b)** were compared to similar tissue structures from both frozen-section and FFPE histology with eosin staining (**Figures 4.10 (c)** and **(d)**). Inspection of selected micro-architectural features

indicated that the ATTO 655 NHS ester stain provided higher-contrast visualization of specific structures, such as collagen fibers, than eosin does in fresh, hydrated specimens. Finally, it has been apparent that nondestructive OTLS microscopy preserved the architecture of the fibro-adipose tissue, in a manner comparable to archival FFPE histology, whereas underlying architecture of the breast tissue was heavily distorted in frozen-section histology (yellow arrowhead).

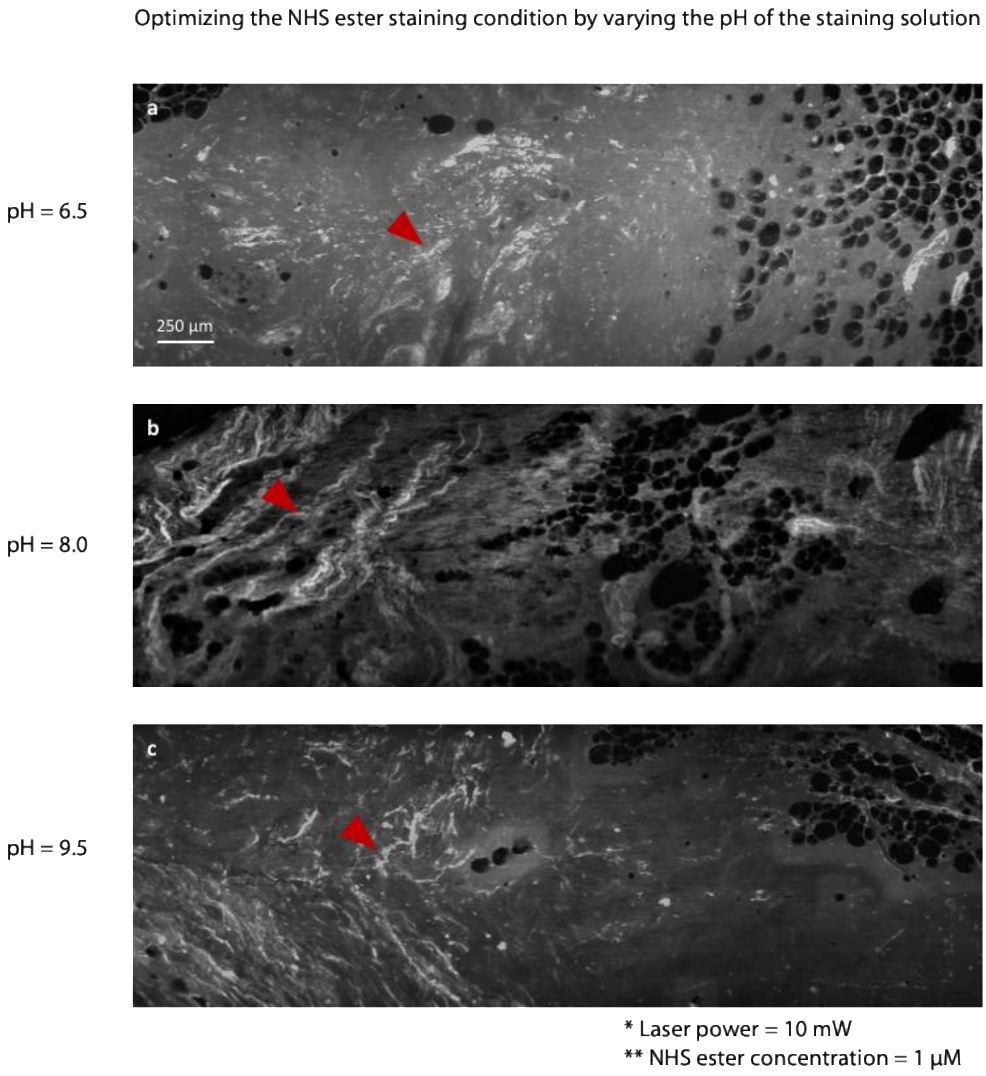

Figure 4.7. (a), (b) and (c) showed NHS ester staining results at different pH conditions (from pH = 6.5 to pH = 9.5). Arrows indicated the collagen fibers within the breast tissues. These results have indicated that a slightly alkaline NHS-ester staining condition (pH = 8) yielded the optimal image contrast.

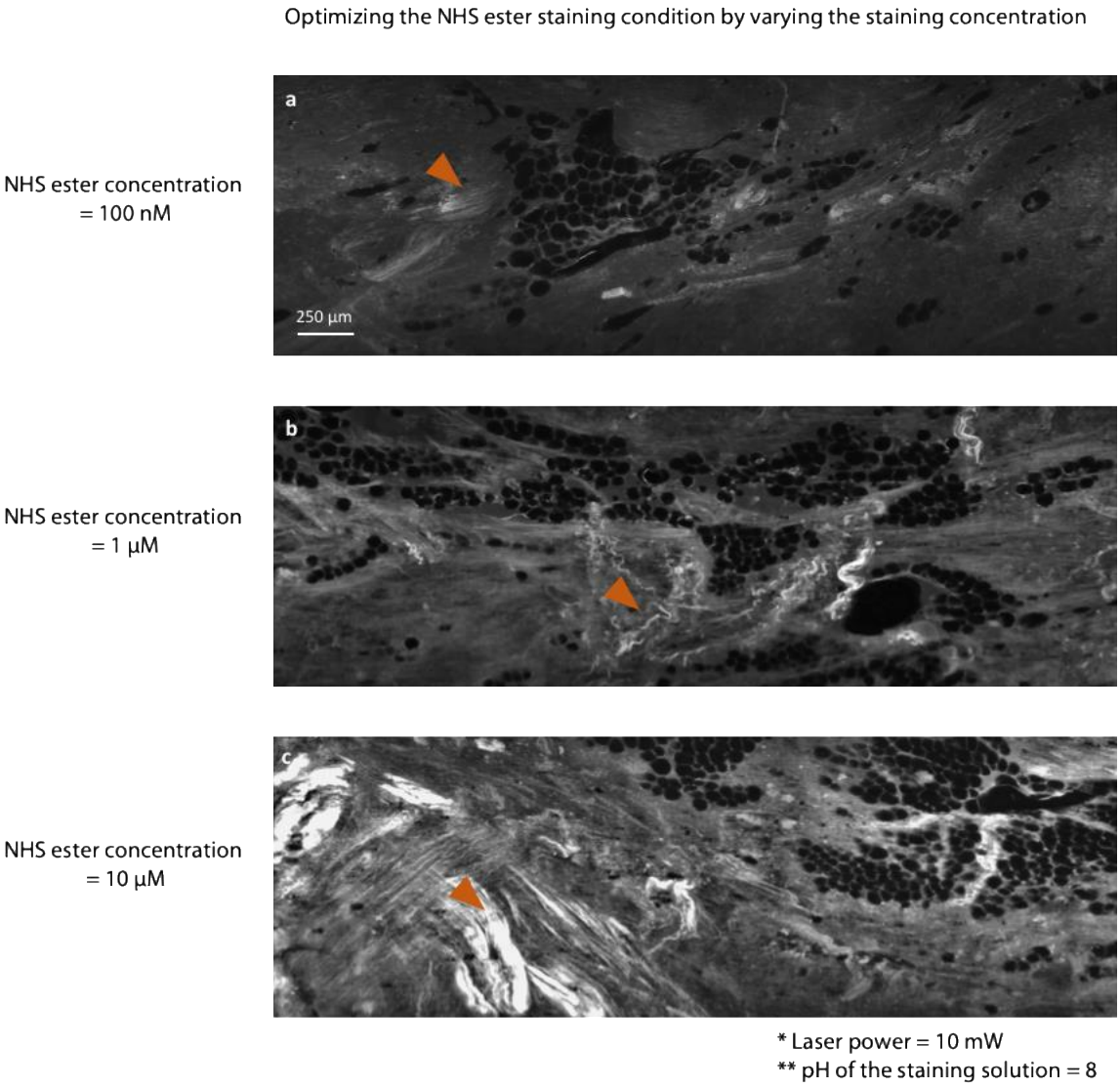

Figure 4.8. (a), (b) and (c) showed NHS ester staining results at different staining concentrations (from 100 nM to 10 µM). When performing OTLS microscopy at high imaging speed (40 sec/cm^2), the 100-nM NHS-ester staining concentration did not provide adequate sensitivity to visualize tissue structures (arrow in (a)). However, increasing the NHS-ester staining concentration to 10 µM caused saturation (arrow in (c)), which deteriorated the image quality. The 1 µM NHS-ester concentration provided the optimal image sensitivity.

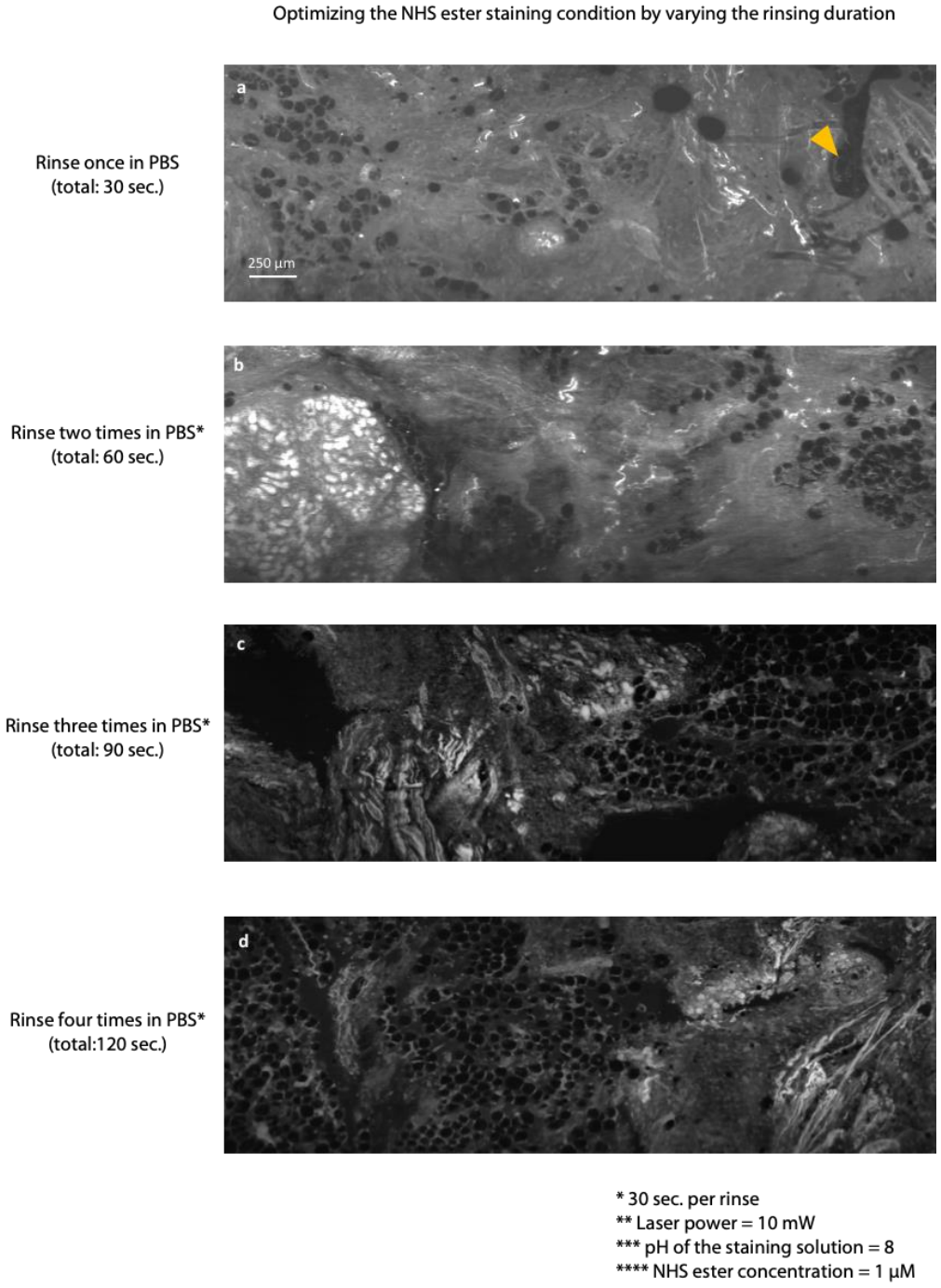

Figure 4.9. (a), (b), (c) and (d) were OTLS microscopy images of NHS-ester stained breast tissues after applying various rinsing steps. Rinsing 1X in saline for 30 second was insufficient to remove all of the unbound NHS ester (arrow in **(a)**). The image contrast (signal-to-background ratio) was improved when rinsing the specimens in saline for a longer duration. In this study, we chose 3 rinse steps in saline for a total of 90 second (30 sec. per rinse) to achieve the optimal image signal-to-background ratio with a sufficiently rapid staining protocol.

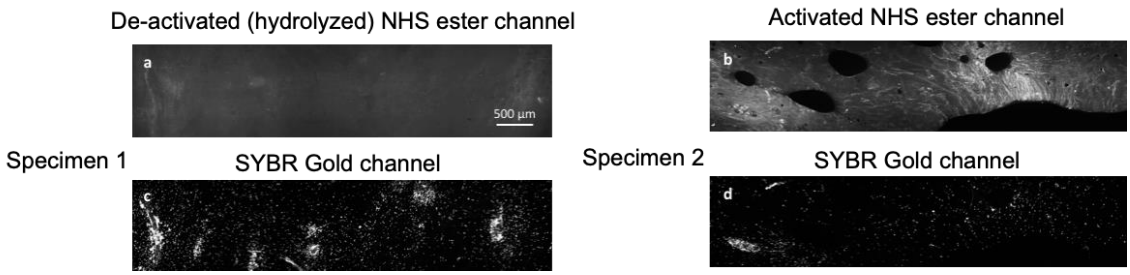

Figure 4.10. Hydrolyzed (de-activated) NHS ester was applied to a tissue surface (a) to confirm that the image contrast provided by reactive (non-hydrolyzed) NHS ester (b) was due to specific chemical binding rather than nonspecific accumulation. For each specimen, the corresponding SYBR Gold channel was shown to outline the tissue structure.

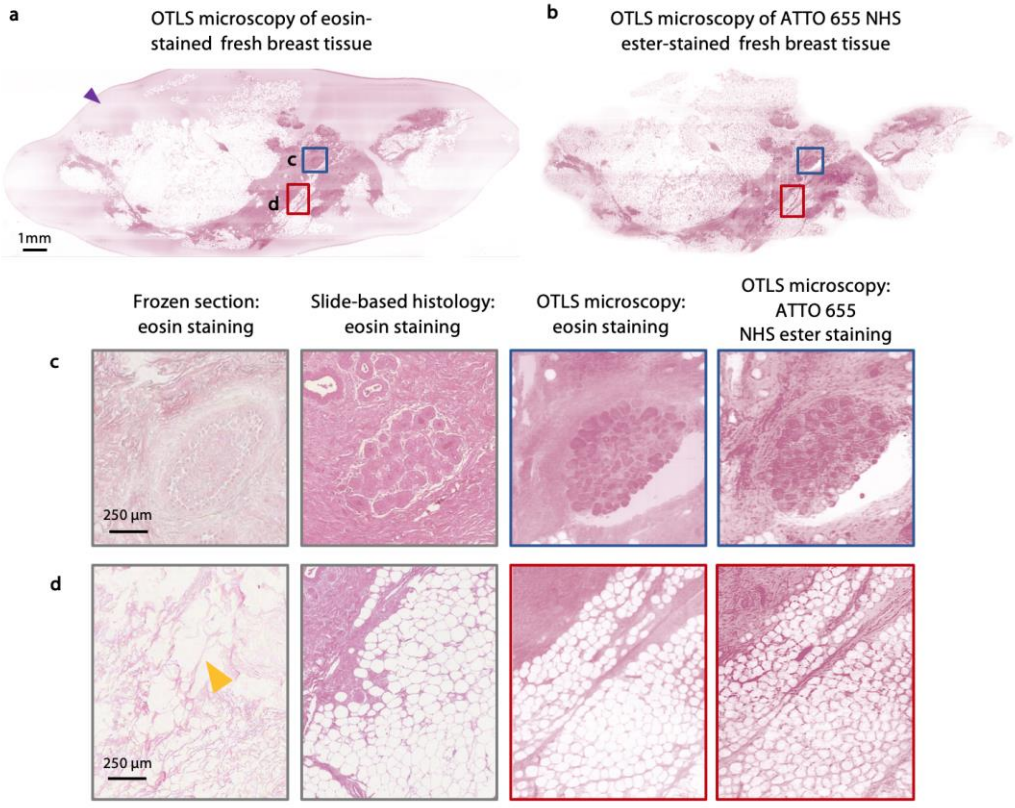

Figure 4.11. A comparison of the image quality between OTLS microscopy of eosin-stained (a) and ATTO 655 NHS-ester-stained (b) fresh breast tissue surfaces. When staining fresh specimens, eosin was not stably bound within the tissue and leaks out of the tissue during imaging (purple arrow), which generated a high background that can deteriorate the image contrast. The image panels in (c) and (d) provided image quality comparisons between frozen-section histology with eosin staining, archival FFPE histology with eosin staining, OTLS microscopy with eosin staining, and OTLS microscopy with ATTO 655 NHS-ester staining. Results showed that the ATTO 655 NHS ester provided improved contrast for visualizing tissue structures, such as collagen fibers, in comparison to eosin in fresh unfixed tissues. Adipocytes and strands of fibrous tissue with stromal cells remained intact after OTLS microscopy and slide-based "H&E" histology. However, the same tissue structures were heavily distorted in frozen-section "H&E" histology ((d), yellow arrow). This figure was published in [81].

4.6 OTLS SURFACE IMAGES FOR FRESH, UNFIXED, SURGICALLY-EXCISED BREAST SPECIMENS

To demonstrate rapid pathology of human breast tissues with an OTLS microscope, discarded surgically excised breast specimens were obtained fresh from patients undergoing lumpectomies and mastectomies at the University of Washington medical center, under informed consent. All human tissues were collected and de-identified by the NorthWest BioTrust (NWBT), a tissue banking resource at the UW, with approval by the UW Human Subjects Division. This study has been described in our recent publication [81]. Reprint permission has been obtained from the publisher.

Fresh surgically excised breast specimens were obtained for our imaging experiments immediately after surgery. After inking all exterior surfaces, each specimen was bisected such that the two adjacent cut-surfaces were mirror images of each other. One half of the specimen (control specimen) underwent routine histological evaluation (H&E histology and IHC), including formalin fixation and paraffin embedding (FFPE). The other half (experimental specimen) was stained with SYBR Gold and ATTO 655 N-hydroxysuccinimide ester (NHS ester) followed by OTLS microscopy (for < 30 minutes). After OTLS microscopy, the specimen was submitted for the same histological evaluation performed on its counterpart. As shown in **Figure 4.12**, these experiments enabled two comparisons: 1) the OTLS surface images were compared to gold-standard H&E histological images to demonstrate that the image quality of our technique can approximate that of archival H&E histology of FFPE tissues; 2) the histology results (H&E and IHC) from experimental specimens (used for OTLS microscopy) were compared to the histology results from corresponding control specimens (untouched by OTLS microscopy methods) to show

that our staining and imaging methods do not interfere with routine post-operative H&E histology and IHC analysis.

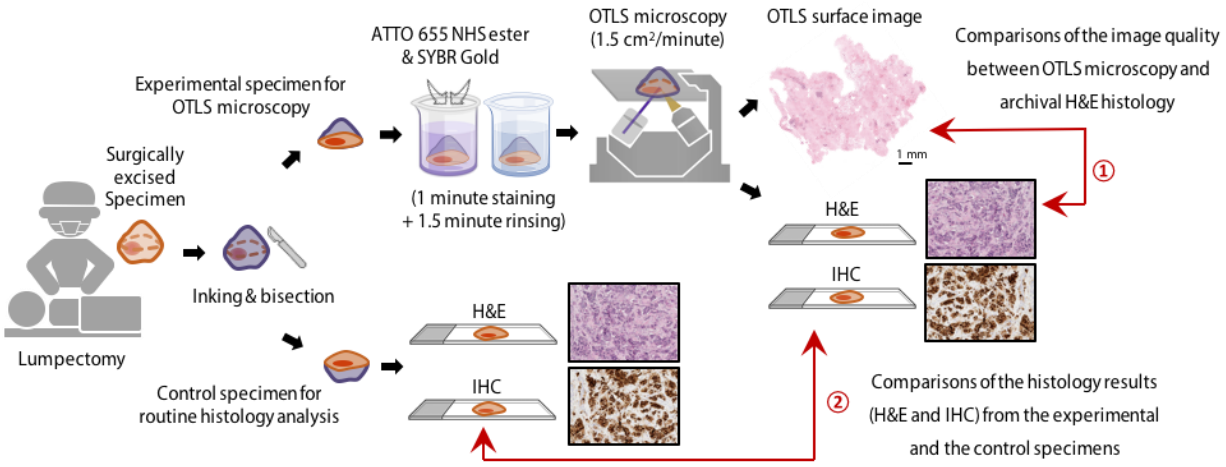

Figure 4.12. Study design. Freshly excised human breast tissues were inked and bisected immediately after lumpectomy procedures. The bisected surface from one half of the specimen (control specimen) was processed for routine histology (H&E and IHC). The bisected surface from the other half (experimental specimen) was stained and imaged with OTLS microscopy (< 30 minutes), before being processed for routine histology. OTLS surface images were compared to archival H&E histology. In addition, histology images from the experimental and control specimens were compared to show that our tissue-staining and imaging techniques would not interfere with downstream H&E histology and IHC. This figure was published in [81].

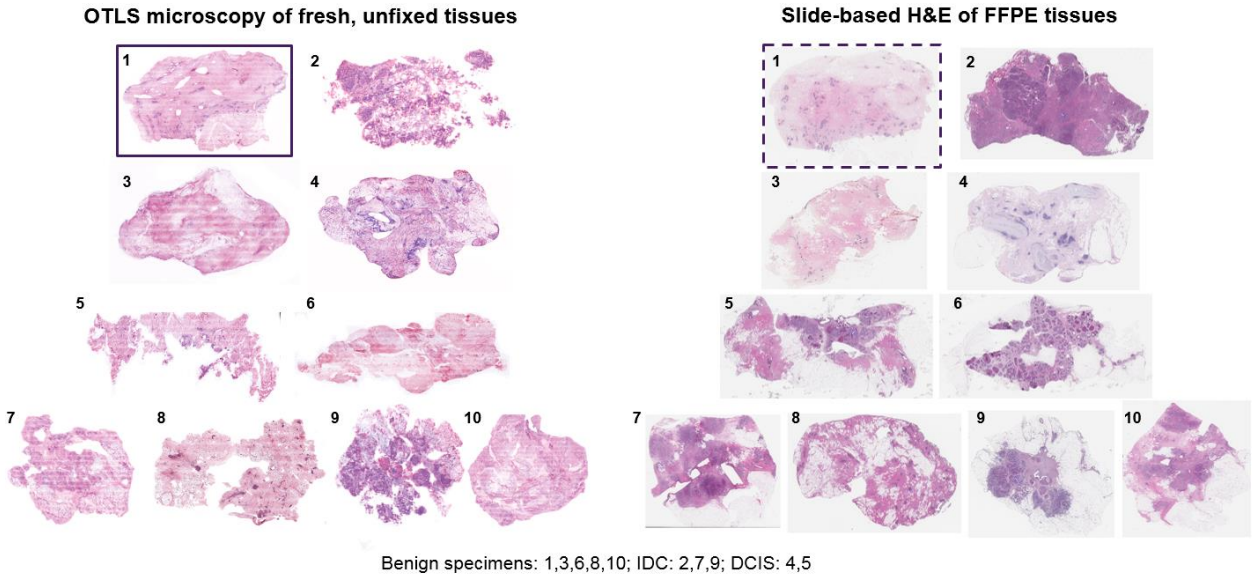

Figure 4.13. Open-top light-sheet microscopy of N = 10 human lumpectomy samples. The surface-extracted OTLS images were on the left and slide-scanned H&E images of the same tissue surface were on the right. The highlighted box denoted the benign breast specimen shown in Figure 4.14.

First of all, we have imaged 10 surgically-excised breast specimens, including benign and cancer samples (**Figure 4.13**). The OTLS surface image of a fresh benign breast specimen (1 cm by 1 cm by 0.5 cm) (**Figure 4.14**) has demonstrated that OTLS microscopy can achieve rapid histologic imaging (1.5 cm^2/minute) of the surface of a large surgical specimen. Important breast structures, such as the breast lobules (**Figure 4.14 (d)**), a duct (**Figure 4.14 (e)**) and a blood vessel within the adipose tissue (**Figure 4.14 (f)**), were identified in the OTLS surface image. The OTLS images in **Figure 4.14** were compared to corresponding slide-based H&E images of the same specimen after formalin fixation and paraffin embedding.

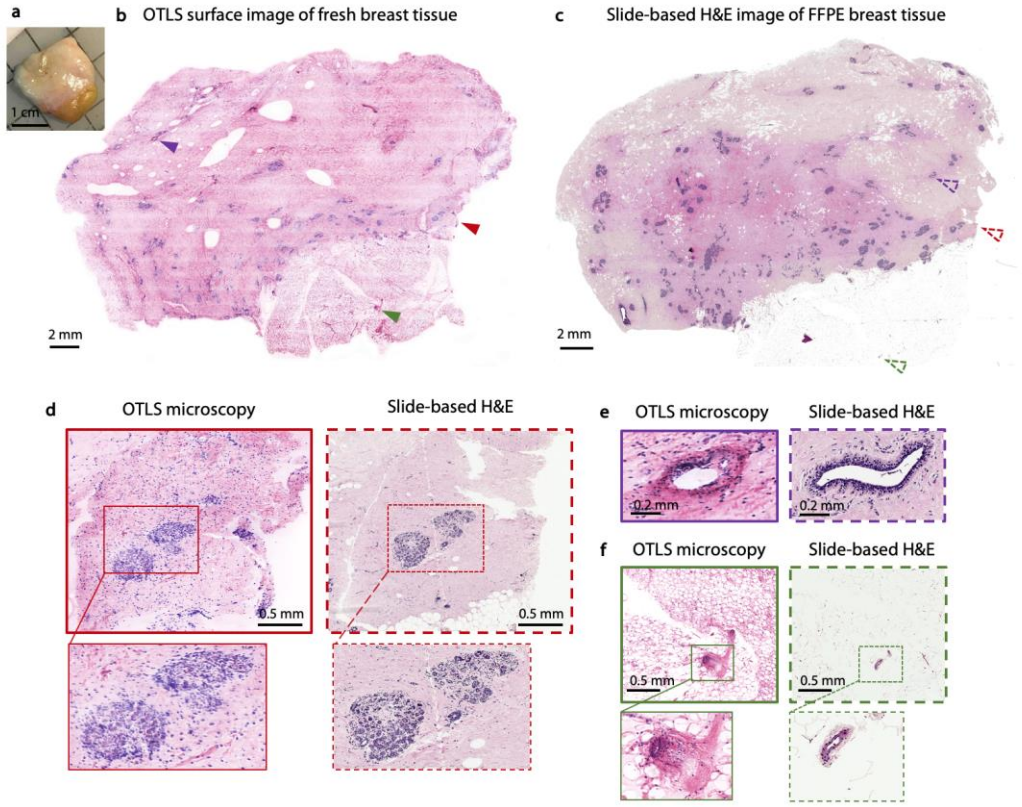

Figure 4.14. A fresh breast specimen (1 cm by 1cm by 0.5 cm, (a)) was first stained with SYBR Gold and ATTO 655 NHS ester followed by surface imaging with an OTLS microscope, (b). After OTLS microscopy, the same piece of tissue was submitted for archival FFPE histology (H&E), (c). Panels (d), (e) and (f) showed benign breast lobules (red arrow), a duct (purple arrow) and a blood vessel within the adipose tissue (green arrow) that were identified from the OTLS surface image, respectively. The corresponding gold-standard H&E images displaying the same tissue features demonstrated that OTLS microscopy with the SYBR Gold and ATTO 655 NHS ester tissue-staining method can enable rapid and high-quality pathology (1.5 cm^2/minute) of a large surgical specimen surface. This figure was published in [81].

Figure 4.15 displayed various microarchitectural features (selected from the 10 specimens listed in **Figure 4.13**) imaged with both OTLS microscopy and conventional slide-based histology. **Figure 4.15 (a)** showed a benign breast lobule with insets showing individual acini with identifiable lumens. Invasive ductal carcinoma (IDC) with Nottingham grade I (**Figure 4.15 (b)**) and Nottingham grade II (**Figure 4.15 (c)**) were characterized by tumor cells penetrating the basement membrane of the duct and infiltrating the surrounding connective tissues. **Figure 4.15 (d)** was an example of ductal carcinoma *in situ* with comedonecrosis. Overall, the quality of our OTLS surface images is similar to that of conventional slide-based H&E images of FFPE tissues, but with slight differences.

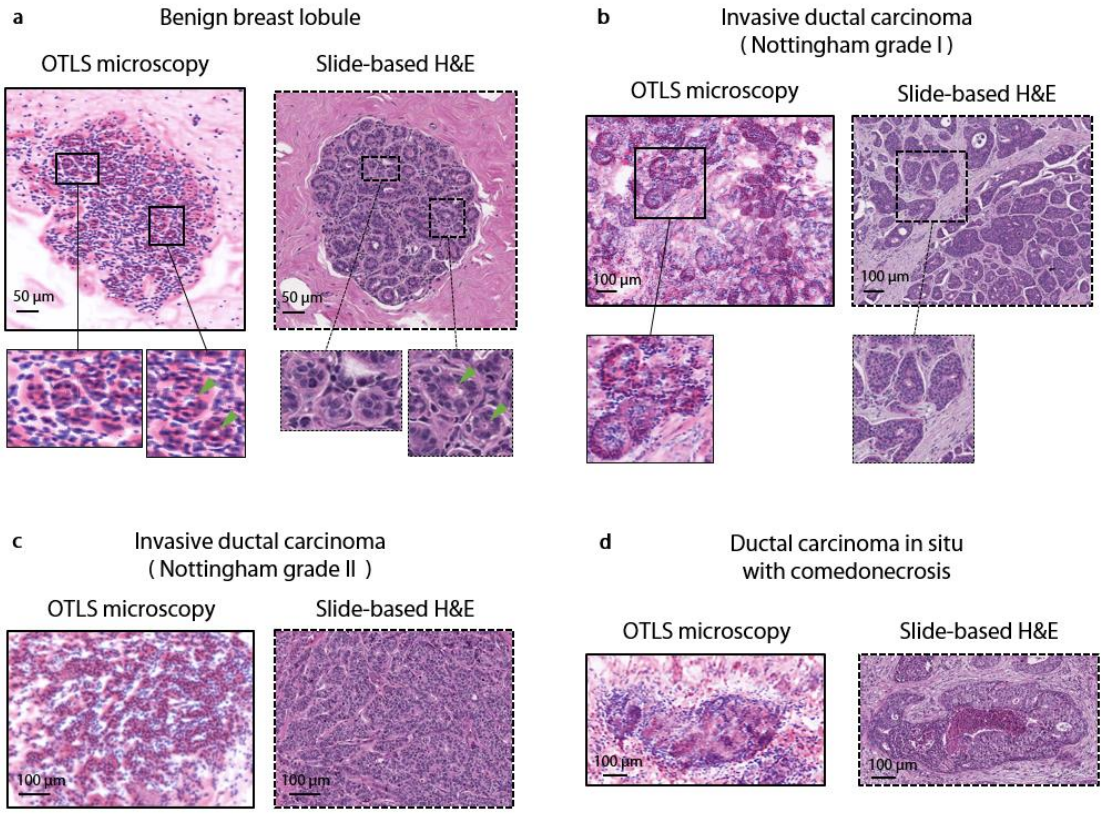

Figure 4.15. Various microarchitectural features were identified from the OTLS images, including (a) a benign breast lobule where the inset showed individual acini with identifiable lumens, (b) invasive ductal carcinoma (IDC) with Nottingham grade I and (c) IDC with Nottingham grade II, d) ductal carcinoma *in situ* with comedonecrosis. This figure was published in [81].

Some of these differences may be attributed to the use of a fluorescent analog of H&E in which the staining characteristics were not chemically identical to conventional H&E. In addition, the topology and cellular contents at the surfaces of grossly cut tissues were likely to be different when compared to microtome-sectioned breast tissues that were formalin fixed and embedded in paraffin (**Figure 4.14**). For example, grossly cut tissue surfaces were likely to contain few, if any, cells that were physically cut open, and may also show slightly different glandular components, such as the acini shown in **Figures 4.14 (d)** and **4.15 (a)**. In addition, grossly cut specimens may contain tissue debris, irregular or soft surfaces that can deform when being flattened and placed on the microscope sample holder, while FFPE tissues were rigidly embedded in wax and sectioned without deformation. For example, the OTLS images of a duct and a blood vessel shown in **Figures 4.14 (e)** and **(f)** appeared to be flattened and sheared such that some of the luminal surfaces are exposed. Further, the adipose tissue (**Figures 4.14 (f)**) showed stronger staining with our ATTO 655 NHS staining protocol compared to routine H&E staining of tissue sections. We hypothesized that this may be due to: (1) ATTO 655 NHS ester covalently binding to cytoplasmic proteins in the fat cells while eosin being weakly bound to the tissue; (2) the 4-μm-thick FFPE tissue sections being thinner than the optical-sectioning thickness (~ 7 μm) of the OTLS microscope system utilized in this particular study, which made the FFPE tissue sections appeared lighter in color. Future OTLS systems with higher resolution have been under development and may help to mitigate some of these issues.

Finally, routine H&E histology and IHC analysis (ER, PR, and HER2 expression) were performed on both control specimens (without OTLS microscopy) and OTLS-microscopy-processed specimens. **Figure 4.16** showed that the H&E and IHC results from the control specimens were qualitatively indistinguishable from the OTLS-microscopy-processed specimens,

suggesting that our OTLS methods would not interfere with downstream post-operative H&E histology and IHC analyses. It is worth mentioning that fluorescent histological assays, such as fluorescence *in situ* hybridization (FISH), have become powerful tools for diagnosing breast cancer [175, 176]. It is possible that the use of fluorescent dyes (ATTO 655 and SYBR Gold) in our proposed tissue-staining protocol may interfere with downstream FISH assays. However, these fluorescent dyes may most likely be bleached and/or washed away by various harsh chemicals (e.g. xylenes and alcohols) during the histology process for FISH.

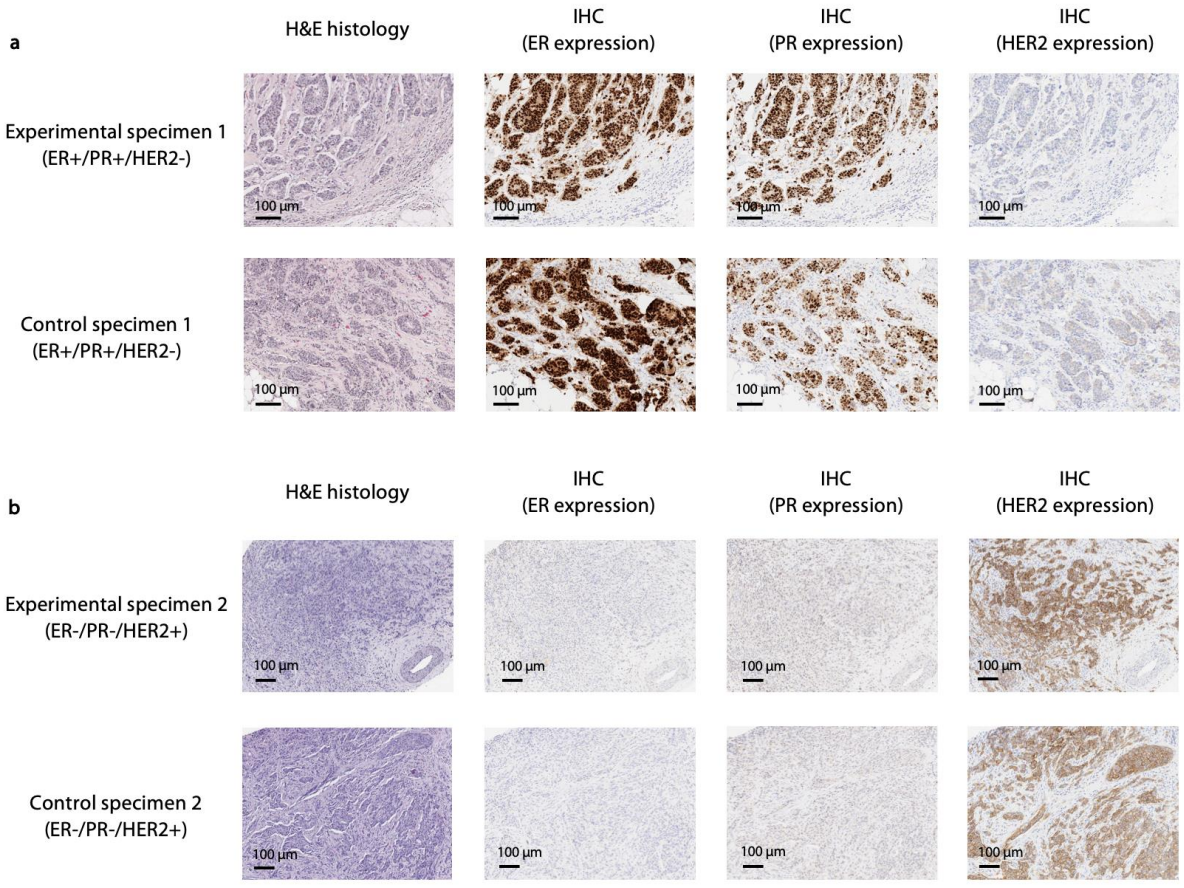

Figure 4.16. (a) H&E histology and (b) IHC results (ER, PR, and HER2 expression) from different control specimens (untouched by OTLS microscopy methods) as compared to those from OTLS microscopy-processed counterparts, showing that the OTLS methods did not interfere with downstream post-operative H&E histology and IHC analysis. This figure was published in [81].

Chapter 5. CONCLUSIONS AND DISCUSSIONS

5.1 MONTE-CARLO SIMULATIONS OF CONFOCAL MICROSCOPES

As described in Chapter 2, we first performed Monte-Carlo simulations to assess the tissue-imaging performance of various confocal microscopes, including dual-axis confocal (DAC) and single-axis confocal (SAC) architectures operating in both point-scanning (PS) and line-scanning (LS) modes [92]. These simulations enabled a direct quantitative comparison between different microscope configurations and are of value for evaluating the relative strengths and weaknesses of each imaging approach [92]. Further, we applied the same models to characterize the optical-sectioning performance (contrast) of DAC-PS and DAC-LS configurations in reflectance mode as a function of θ and α. These results can be exploited for guiding the optimal designs of DAC-PS and DAC-LS microscopes [91].

In both studies, Monte-Carlo simulations were performed via a commercially available optical simulation software (FRED). While this method provided simulation results that were consistent with experimental validations [87, 95], the FRED software was not well-equipped to simulate fluorescence microscopy in an efficient way. Therefore, only reflectance-based tissue-imaging was modeled in previous studies [91, 92]. An alternative Monte-Carlo method would be needed to simulate the performance of fluorescence-based imaging systems. For example, a recent study in our group focused on utilizing an adjoint Monte-Carlo simulation method to more-accurately and efficiently model the fluorescence illumination and detection of light-sheet microscopy in highly scattering tissues [155].

As mentioned in Chapter 2.3, traditional Monte-Carlo simulations do not account for polarization, diffraction and absorption, nor do they model other scattering events in real tissue,

such as refractive beam steering and lensing effects introduced by micro-architectural tissue structures. While these issues are not as important for low-resolution imaging applications, they limit the accuracy of this traditional method for investigating the realistic light-tissue interactions when imaging biological specimens at high resolution. Other simulation methods that have been frequently used for accurately modeling light-tissue interactions at finer scales include finite-difference time-domain (FDTD) [177], pseudo-spectral time-domain (PSTD) [178] or beam propagation methods (BPM)[36]. However, these methods are often computationally intensive and time consuming (such as FDTD or PSTD), or still not truly representative of light scattering in real heterogeneous tissues (such as BPM) [129]. Therefore, we have recently developed a novel fractal propagation method (FPM) [129], for realistic microscopy simulations in tissues. The FPM has incorporated (1) a beam propagation model, which is a simplified numerical technique for modeling light transport in media with weak variations in refractive index, along with (2) a fractal model of the refractive-index turbulence seen in real biological tissues [129]. Compared to standard simulation methods (e.g., Monte Carlo or FDTD), we have shown that this novel FPM can accurately simulate the diffraction effects of weakly (low-NA) focused beams in 3D, as well as the effects of multi-scale refractive heterogeneities in biological tissues that are known to cause scattering, beam steering, and the distortion/aberration of beam foci [30]. Details about the FPM have been described in Glaser *et al*. [129].

5.2 DAC MICROSCOPY WITH BESSEL ILLUMINATION

Bessel beams have recently been investigated as a means of improving deep-tissue microscopy in highly scattering and heterogeneous media [35-39]. It has been suggested that the extended depth-of-field and self-reconstructing properties of a Bessel beam can provide an increased penetration depth of the focused beam in tissues compared to a conventional Gaussian beam [22, 35-39].

However, a study is needed to better quantify the magnitude of the beam steering as well as the distortion of focused Gaussian and Bessel beams in tissues with microscopic heterogeneities.

At first, we developed an imaging method and quantitative metrics to evaluate the motion and distortion of low- NA Gaussian and Bessel beams focused in water, heterogeneous phantoms, and fresh mouse esophagus tissues [30]. This study showed that low-NA Bessel beams exhibited reduced beam-steering artifacts and distortions compared to Gaussian beams, and were therefore potentially useful for microscopy applications in which pointing accuracy and beam quality are critical, such as DAC microscopy [30]. As a result, we implemented both Gaussian and Bessel illumination in a point-scanned DAC microscope and quantified the resultant degradation in resolution when imaging heterogeneous optical phantoms and fresh tissues. Results suggested that DAC microscopy with Bessel illumination exhibited reduced resolution degradation from microscopic tissue heterogeneities compared to DAC microscopy with conventional Gaussian illumination [34].

Our motivation for performing these studies was the observation that DAC microscopy imaging performance is sensitive to positional changes and distortions at the foci of the two low-NA beams utilized in an off-axis arrangement [127, 128]. For example, in previous studies with tissue-like phantoms, our group and others have observed that heterogeneity-induced beam steering has caused a degradation in spatial resolution in DAC microscope [32, 95]. However, a single-axis illumination and collection architecture (e.g. optical coherence tomography [179] and conventional confocal microscopy [84, 85]) may be less sensitive to tissue heterogeneities due to the common path traversed by the incoming and outgoing ballistic photons.

In the *ex vivo* imaging experiments [34], we noticed that the diffraction side lobes of a Bessel beam contribute out-of-focus background that decreases image contrast. In addition, since

each of these diffraction side lobes carry approximately the same amount of energy as the Bessel main lobe [118-120], Bessel illumination usually requires higher laser power than Gaussian illumination [34]. Intense laser irradiation can cause photodamage and photobleaching throughout the specimen [180, 181], which may limit the use of Bessel-illumination for certain biomedical applications [34]. Different approaches have been investigated by others to alleviate these trade-offs (e.g. two-photon excitation, structured illumination, deconvolution, sectioned Bessel beams, energy-efficient low-Fresnel-number Bessel beams, etc.) [21, 35, 38, 123, 125, 182]. Similar approaches will need to be explored in the future to obtain an optimal balance among image contrast, resolution and photon budget for various imaging applications of DAC microscopy. For example, for *in vivo* and *ex vivo* clinical applications of DAC microscopy, the ability to image with high resolution and contrast at depths of hundreds of microns within tissues could be valuable for early disease detection, surgical guidance, post-operative pathology, and biopsy guidance [6, 40, 41, 183-186].

5.3 OTLS MICROSCOPY FOR RAPID PATHOLOGY OF LUMPECTOMY MARGINS

In Chapter 4.6, we have showcased preliminary results to evaluate the feasibility of translating OTLS microscopy into clinical practice. As discussed in [81], upcoming versions of the OTLS microscope should realistically be able to fit within the size of a laser printer. Future clinical systems should also contain an enclosure to protect the optical hardware as well as to reduce ambient light such that the OTLS microscope may be used in a standard pathology lab or surgical facility. In terms of clinical translation, the OTLS microscope presented in our recent study [81] could benefit from the following improvements:

First, the current two-channel OTLS imaging speed (1.5 cm^2/ minute) has been limited by the highest frame rate of a state-of-the-art sCMOS camera. As higher-speed detectors become available, imaging speeds may be further improved. In the current system, there has been a tradeoff between the height of the imaging volume acquired by the sCMOS camera and imaging speed. For imaging breast tissues, which are pliable and therefore can sit relatively flat on the glass-plate sample holder, a relatively shallow image size of 1000-pixels wide by 128-pixels high has been used (64 pixels per channel, which corresponds to ~80 μm in spatial dimension), which was sufficient to account for most surface irregularities, specimen tilt, and tissue debris [46, 81]. However, when imaging stiff tissues with highly irregular surfaces, such as fresh radical prostatectomy specimens, it may be necessary to increase the image height to accommodate for surface irregularities. Yet, our study [46] has shown that changing the image height directly affected the OTLS imaging speed. Second, data storage will present another challenge for clinical translation. For example, a two-channel OTLS dataset of a 2 cm by 2 cm specimen requires ~81.6 GB of hard drive space. We have been exploring the use of methods [187] to compress the OTLS datasets without significant image degradation. Finally, our current multi-step data acquisition and processing pipeline has not been well-suited for routine clinical practice. A simpler consolidated software package with improved efficiency is needed. Meanwhile, larger-scale clinical studies are also needed to fully examine these and other clinical-workflow challenges.

On the other hand, the spatial resolution of the OTLS system can be further increased to provide better imaging of subcellular features, such as nucleoli. However, there will be trade-offs between imaging speed and resolution that may not be desired for certain applications, such as intraoperative guidance, where imaging speed would be of primary concern. In particular, since post-operative slide-based histopathology can still be utilized after nondestructive OTLS

microscopy, the sensitivity and specificity requirements of OTLS microscopy may not be as stringent as what is desired for primary diagnosis and grading.

In summary, we have improved and optimized an OTLS system, along with a reliable and fast two-color staining method (2.5 minutes), to generate H&E false-colored images of fresh breast tissue surfaces within time frames that can be conducive to intraoperative use (1.5 cm^2/minute). Our results have provided the first comparison between a pseudo-H&E OTLS microscopy strategy and both frozen-section and archival FFPE histology. In addition, preliminary results have suggested that our nondestructive imaging method is compatible with downstream archival H&E histology and IHC analyses, which are currently relied upon for definitive clinical diagnoses. While we have described important technical advances in OTLS microscopy and have assessed the basic feasibility of our system for rapid pathology of lumpectomy margins in [46, 81], rigorous clinical validation is still required to assess the ability to accurately identify various breast pathologies, such as *in situ* carcinoma, within intraoperative time frames.

In recent years, multidisciplinary efforts in artificial intelligence, genomics and immunology have been leveraged and combined to address unmet needs in biology and medicine. In the future, OTLS microscopy may be synergistic with these fast-growing disciplines, to accelerate scientific or medical breakthroughs.

BIBLIOGRAPHY

1. V. Ntziachristos, "Going deeper than microscopy: the optical imaging frontier in biology," Nat Methods **7**, 603-614 (2010).
2. D. L. Dickensheets and G. S. Kino, "Micromachined scanning confocal optical microscope," Opt Lett **21**, 764-766 (1996).
3. G. J. Tearney, R. H. Webb, and B. E. Bouma, "Spectrally encoded confocal microscopy," Opt Lett **23**, 1152-1154 (1998).
4. Y. G. Patel, M. Rajadhyaksha, and C. A. Dimarzio, "Optimization of pupil design for point-scanning and line-scanning confocal microscopy," Biomed Opt Express **2**, 2231-2242 (2011).
5. J. T. Liu, N. O. Loewke, M. J. Mandella, R. M. Levenson, J. M. Crawford, and C. H. Contag, "Point-of-care pathology with miniature microscopes," Anal Cell Pathol (Amst) **34**, 81-98 (2011).
6. E. F. Brachtel, N. B. Johnson, A. E. Huck, T. L. Rice-Stitt, M. G. Vangel, B. L. Smith, G. J. Tearney, and D. Kang, "Spectrally encoded confocal microscopy for diagnosing breast cancer in excision and margin specimens," Lab Invest **96**, 459-467 (2016).
7. J. Eschbacher, N. L. Martirosyan, P. Nakaji, N. Sanai, M. C. Preul, K. A. Smith, S. W. Coons, and R. F. Spetzler, "In vivo intraoperative confocal microscopy for real-time histopathological imaging of brain tumors," J Neurosurg **116**, 854-860 (2012).
8. J. K. Karen, D. S. Gareau, S. W. Dusza, M. Tudisco, M. Rajadhyaksha, and K. S. Nehal, "Detection of basal cell carcinomas in Mohs excisions with fluorescence confocal mosaicing microscopy," Br J Dermatol **160**, 1242-1250 (2009).
9. N. J. Durr, C. T. Weisspfennig, B. A. Holfeld, and A. Ben-Yakar, "Maximum imaging depth of two-photon autofluorescence microscopy in epithelial tissues," J Biomed Opt **16**, 026008 (2011).
10. M. G. Giacomelli, T. Yoshitake, L. C. Cahill, H. Vardeh, L. M. Quintana, B. E. Faulkner-Jones, J. Brooker, J. L. Connolly, and J. G. Fujimoto, "Multiscale nonlinear microscopy and widefield white light imaging enables rapid histological imaging of surgical specimen margins," Biomed Opt Express **9**, 2457-2475 (2018).
11. Y. H. Lai, S. Y. Lee, C. F. Chang, Y. H. Cheng, and C. K. Sun, "Nonlinear photoacoustic microscopy via a loss modulation technique: from detection to imaging," Opt Express **22**, 525-536 (2014).
12. J. Huisken and D. Y. Stainier, "Even fluorescence excitation by multidirectional selective plane illumination microscopy (mSPIM)," Opt Lett **32**, 2608-2610 (2007).
13. F. O. Fahrbach, F. F. Voigt, B. Schmid, F. Helmchen, and J. Huisken, "Rapid 3D light-sheet microscopy with a tunable lens," Opt Express **21**, 21010-21026 (2013).
14. K. Patorski, M. Trusiak, and T. Tkaczyk, "Optically-sectioned two-shot structured illumination microscopy with Hilbert-Huang processing," Opt Express **22**, 9517-9527 (2014).
15. M. Wang, H. Z. Kimbrell, A. B. Sholl, D. B. Tulman, K. N. Elfer, T. C. Schlichenmeyer, B. R. Lee, M. Lacey, and J. Q. Brown, "High-Resolution Rapid Diagnostic Imaging of Whole Prostate Biopsies Using Video-Rate Fluorescence Structured Illumination Microscopy," Cancer Res **75**, 4032-4041 (2015).
16. F. T. Nguyen, A. M. Zysk, E. J. Chaney, J. G. Kotynek, U. J. Oliphant, F. J. Bellafiore, K. M. Rowland, P. A. Johnson, and S. A. Boppart, "Intraoperative evaluation of breast tumor margins with optical coherence tomography," Cancer Res **69**, 8790-8796 (2009).
17. J. Polans, D. Cunefare, E. Cole, B. Keller, P. S. Mettu, S. W. Cousins, M. J. Allingham, J. A. Izatt, and S. Farsiu, "Enhanced visualization of peripheral retinal vasculature with wavefront sensorless adaptive optics optical coherence tomography angiography in diabetic patients," Opt Lett **42**, 17-20 (2017).
18. K. I. Willig, B. Harke, R. Medda, and S. W. Hell, "STED microscopy with continuous wave beams," Nat Methods **4**, 915-918 (2007).
19. E. Betzig, G. H. Patterson, R. Sougrat, O. W. Lindwasser, S. Olenych, J. S. Bonifacino, M. W. Davidson, J. Lippincott-Schwartz, and H. F. Hess, "Imaging intracellular fluorescent proteins at nanometer resolution," Science **313**, 1642-1645 (2006).
20. M. J. Rust, M. Bates, and X. Zhuang, "Sub-diffraction-limit imaging by stochastic optical reconstruction microscopy (STORM)," Nat Methods **3**, 793-795 (2006).

21. F. O. Fahrbach, V. Gurchenkov, K. Alessandri, P. Nassoy, and A. Rohrbach, "Self-reconstructing sectioned Bessel beams offer submicron optical sectioning for large fields of view in light-sheet microscopy," Opt Express **21**, 11425-11440 (2013).
22. T. Vettenburg, H. I. Dalgarno, J. Nylk, C. Coll-Llado, D. E. Ferrier, T. Cizmar, F. J. Gunn-Moore, and K. Dholakia, "Light-sheet microscopy using an Airy beam," Nat Methods **11**, 541-544 (2014).
23. B. C. Chen, W. R. Legant, K. Wang, L. Shao, D. E. Milkie, M. W. Davidson, C. Janetopoulos, X. S. Wu, J. A. Hammer, 3rd, Z. Liu, B. P. English, Y. Mimori-Kiyosue, D. P. Romero, A. T. Ritter, J. Lippincott-Schwartz, L. Fritz-Laylin, R. D. Mullins, D. M. Mitchell, J. N. Bembenek, A. C. Reymann, R. Bohme, S. W. Grill, J. T. Wang, G. Seydoux, U. S. Tulu, D. P. Kiehart, and E. Betzig, "Lattice light-sheet microscopy: imaging molecules to embryos at high spatiotemporal resolution," Science **346**, 1257998 (2014).
24. R. Tomer, L. Ye, B. Hsueh, and K. Deisseroth, "Advanced CLARITY for rapid and high-resolution imaging of intact tissues," Nat Protoc **9**, 1682-1697 (2014).
25. W. Li, R. N. Germain, and M. Y. Gerner, "Multiplex, quantitative cellular analysis in large tissue volumes with clearing-enhanced 3D microscopy (Ce3D)," Proc Natl Acad Sci U S A **114**, E7321-E7330 (2017).
26. C. Pan, R. Cai, F. P. Quacquarelli, A. Ghasemigharagoz, A. Lourbopoulos, P. Matryba, N. Plesnila, M. Dichgans, F. Hellal, and A. Erturk, "Shrinkage-mediated imaging of entire organs and organisms using uDISCO," Nat Methods **13**, 859-867 (2016).
27. G. M. Cooper and R. E. Hausman, *The Cell: A Molecular Approach* (ASM Press, 2007).
28. S. Johnsen and E. A. Widder, "The physical basis of transparency in biological tissue: ultrastructure and the minimization of light scattering," J Theor Biol **199**, 181-198 (1999).
29. I. J. Bigio and S. G. Bown, "Spectroscopic sensing of cancer and cancer therapy: current status of translational research," Cancer Biol Ther **3**, 259-267 (2004).
30. Y. Chen and J. T. Liu, "Characterizing the beam steering and distortion of Gaussian and Bessel beams focused in tissues with microscopic heterogeneities," Biomed Opt Express **6**, 1318-1330 (2015).
31. T. Biwas and A. Gupta, "Retrieval of true color of the internal organ of CT images and attempt to tissue characterization by refractive index : Initial experience," **12**, 169-178 (2002).
32. P. J. Dwyer, C. A. DiMarzio, J. M. Zavislan, W. J. Fox, and M. Rajadhyaksha, "Confocal reflectance theta line scanning microscope for imaging human skin in vivo," Opt Lett **31**, 942-944 (2006).
33. M. Rajadhyaksha, "Confocal microscopy of skin cancers: translational advances toward clinical utility," Conf Proc IEEE Eng Med Biol Soc **2009**, 3231-3233 (2009).
34. Y. Chen, A. Glaser, and J. T. Liu, "Bessel-beam illumination in dual-axis confocal microscopy mitigates resolution degradation caused by refractive heterogeneities," J Biophotonics **10**, 68-74 (2017).
35. M. Zhao, H. Zhang, Y. Li, A. Ashok, R. Liang, W. Zhou, and L. Peng, "Cellular imaging of deep organ using two-photon Bessel light-sheet nonlinear structured illumination microscopy," Biomedical optics express **5**, 1296-1308 (2014).
36. F. O. Fahrbach, P. Simon, and A. Rohrbach, "Microscopy with self-reconstructing beams," Nature Photonics **4**, 780-785 (2010).
37. S. B. Purnapatra, S. Bera, and P. P. Mondal, "Spatial filter based Bessel-like beam for improved penetration depth imaging in fluorescence microscopy," Scientific reports **2**, 692 (2012).
38. T. A. Planchon, L. Gao, D. E. Milkie, M. W. Davidson, J. A. Galbraith, C. G. Galbraith, and E. Betzig, "Rapid three-dimensional isotropic imaging of living cells using Bessel beam plane illumination," Nature methods **8**, 417-423 (2011).
39. F. O. Fahrbach and A. Rohrbach, "Propagation stability of self-reconstructing Bessel beams enables contrast-enhanced imaging in thick media," Nature communications **3**, 632 (2012).
40. Y. K. Tao, D. Shen, Y. Sheikine, O. O. Ahsen, H. H. Wang, D. B. Schmolze, N. B. Johnson, J. S. Brooker, A. E. Cable, J. L. Connolly, and J. G. Fujimoto, "Assessment of breast pathologies using nonlinear microscopy," Proceedings of the National Academy of Sciences **111**, 15304-15309 (2014).
41. H. Tu, Y. Liu, D. Turchinovich, M. Marjanovic, J. K. Lyngsø, J. Lægsgaard, E. J. Chaney, Y. Zhao, S. You, W. L. Wilson, B. Xu, M. Dantus, and S. A. Boppart, "Stain-free histopathology by programmable supercontinuum pulses," Nature Photonics **10**, 534 (2016).
42. T. Yoshitake, M. G. Giacomelli, L. M. Quintana, H. Vardeh, L. C. Cahill, B. E. Faulkner-Jones, J. L. Connolly, D. Do, and J. G. Fujimoto, "Rapid histopathological imaging of skin and breast cancer surgical specimens using immersion microscopy with ultraviolet surface excitation," Sci Rep **8**, 4476 (2018).
43. F. Fereidouni, Z. T. Harmany, M. Tian, A. Todd, J. A. Kintner, J. D. McPherson, A. D. Borowsky, M. Lechpammer, J. Bishop, S. G. Demos, and R. Levenson, "Microscopy with ultraviolet surface excitation for rapid slide-free histology," Nat Biomed Eng **1**, 957-966 (2017).

44. T. C. Schlichenmeyer, M. Wang, K. N. Elfer, and J. Q. Brown, "Video-rate structured illumination microscopy for high-throughput imaging of large tissue areas," Biomed Opt Express **5**, 366-377 (2014).
45. M. Wang, D. B. Tulman, A. B. Sholl, H. Z. Kimbrell, S. H. Mandava, K. N. Elfer, S. Luethy, M. M. Maddox, W. Lai, B. R. Lee, and J. Q. Brown, "Gigapixel surface imaging of radical prostatectomy specimens for comprehensive detection of cancer-positive surgical margins using structured illumination microscopy," Scientific Reports **6**, 27419 (2016).
46. A. K. Glaser, N. P. Reder, Y. Chen, E. F. McCarty, C. Yin, L. Wei, Y. Wang, L. D. True, and J. T. C. Liu, "Light-sheet microscopy for slide-free non-destructive pathology of large clinical specimens," Nat Biomed Eng **1**(2017).
47. C. DeSantis, J. Ma, L. Bryan, and A. Jemal, "Breast cancer statistics, 2013," CA Cancer J Clin **64**, 52-62 (2014).
48. N. Hou and D. Huo, "A trend analysis of breast cancer incidence rates in the United States from 2000 to 2009 shows a recent increase," Breast Cancer Res Treat **138**, 633-641 (2013).
49. B. Fisher, S. Anderson, J. Bryant, R. G. Margolese, M. Deutsch, E. R. Fisher, J. H. Jeong, and N. Wolmark, "Twenty-year follow-up of a randomized trial comparing total mastectomy, lumpectomy, and lumpectomy plus irradiation for the treatment of invasive breast cancer," N Engl J Med **347**, 1233-1241 (2002).
50. J. A. Jacobson, D. N. Danforth, K. H. Cowan, T. d'Angelo, S. M. Steinberg, L. Pierce, M. E. Lippman, A. S. Lichter, E. Glatstein, and P. Okunieff, "Ten-year results of a comparison of conservation with mastectomy in the treatment of stage I and II breast cancer," N Engl J Med **332**, 907-911 (1995).
51. I. Gage, S. J. Schnitt, A. J. Nixon, B. Silver, A. Recht, S. L. Troyan, T. Eberlein, S. M. Love, R. Gelman, J. R. Harris, and J. L. Connolly, "Pathologic margin involvement and the risk of recurrence in patients treated with breast-conserving therapy," Cancer **78**, 1921-1928 (1996).
52. K. C. Horst, M. C. Smitt, D. R. Goffinet, and R. W. Carlson, "Predictors of local recurrence after breast-conservation therapy," Clin Breast Cancer **5**, 425-438 (2005).
53. L. Jacobs, "Positive margins: the challenge continues for breast surgeons," Ann Surg Oncol **15**, 1271-1272 (2008).
54. J. F. Waljee, E. S. Hu, L. A. Newman, and A. K. Alderman, "Predictors of re-excision among women undergoing breast-conserving surgery for cancer," Ann Surg Oncol **15**, 1297-1303 (2008).
55. R. Jeevan, D. A. Cromwell, M. Trivella, G. Lawrence, O. Kearins, J. Pereira, C. Sheppard, C. M. Caddy, and J. H. van der Meulen, "Reoperation rates after breast conserving surgery for breast cancer among women in England: retrospective study of hospital episode statistics," BMJ **345**, e4505 (2012).
56. N. Q. Mirza, G. Vlastos, F. Meric, T. A. Buchholz, N. Esnaola, S. E. Singletary, H. M. Kuerer, L. A. Newman, F. C. Ames, M. I. Ross, B. W. Feig, R. E. Pollock, M. McNeese, E. Strom, and K. K. Hunt, "Predictors of locoregional recurrence among patients with early-stage breast cancer treated with breast-conserving therapy," in *Ann Surg Oncol*, (2002), pp. 256-265.
57. C. C. Park, M. Mitsumori, A. Nixon, A. Recht, J. Connolly, R. Gelman, B. Silver, S. Hetelekidis, A. Abner, J. R. Harris, and S. J. Schnitt, "Outcome at 8 years after breast-conserving surgery and radiation therapy for invasive breast cancer: influence of margin status and systemic therapy on local recurrence," in *J Clin Oncol*, (2000), pp. 1668-1675.
58. F. A. Vicini, L. Kestin, R. Huang, and A. Martinez, "Does local recurrence affect the rate of distant metastases and survival in patients with early-stage breast carcinoma treated with breast-conserving therapy?," in *Cancer*, (2003), pp. 910-919.
59. M. S. Moran, S. J. Schnitt, A. E. Giuliano, J. R. Harris, S. A. Khan, J. Horton, S. Klimberg, M. Chavez-MacGregor, G. Freedman, N. Houssami, P. L. Johnson, M. Morrow, O. Society of Surgical, and O. American Society for Radiation, "Society of Surgical Oncology-American Society for Radiation Oncology consensus guideline on margins for breast-conserving surgery with whole-breast irradiation in stages I and II invasive breast cancer," J Clin Oncol **32**, 1507-1515 (2014).
60. B. J. Adams, C. K. Zoon, C. Stevenson, P. Chitnavis, L. Wolfe, and H. D. Bear, "The role of margin status and reexcision in local recurrence following breast conservation surgery," in *Ann Surg Oncol*, (2013), pp. 2250-2255.
61. H. A. Jones, N. Antonini, A. A. M. Hart, J. L. Peterse, J.-C. Horiot, F. Collin, P. M. Poortmans, S. B. Oei, L. Collette, H. Struikmans, W. F. Van den Bogaert, A. Fourquet, J. J. Jager, D. A. X. Schinagl, C. C. Wárlám-Rodenhuis, and H. Bartelink, "Impact of pathological characteristics on local relapse after breast-conserving therapy: a subgroup analysis of the EORTC boost versus no boost trial," in *J Clin Oncol*, (2009), pp. 4939-4947.

62. R. G. Pleijhuis, M. Graafland, J. de Vries, J. Bart, J. S. de Jong, and G. M. van Dam, "Obtaining adequate surgical margins in breast-conserving therapy for patients with early-stage breast cancer: current modalities and future directions," in *Ann Surg Oncol*, (2009), pp. 2717-2730.
63. S. E. Singletary, "Surgical margins in patients with early-stage breast cancer treated with breast conservation therapy," in *Am J Surg*, (2002), pp. 383-393.
64. G. Zavagno, E. Goldin, R. Mencarelli, G. Capitanio, P. Del Bianco, R. Marconato, S. Mocellin, G. Marconato, V. Belardinelli, F. Marcon, and D. Nitti, "Role of resection margins in patients treated with breast conservation surgery," in *Cancer*, (2008), pp. 1923-1931.
65. K. Coffey, D. D'Alessio, D. M. Keating, and E. A. Morris, "Second-Opinion Review of Breast Imaging at a Cancer Center: Is It Worthwhile?," AJR Am J Roentgenol **208**, 1386-1391 (2017).
66. N. Cabioglu, K. K. Hunt, A. A. Sahin, H. M. Kuerer, G. V. Babiera, S. E. Singletary, G. J. Whitman, M. I. Ross, F. C. Ames, B. W. Feig, T. A. Buchholz, and F. Meric-Bernstam, "Role for intraoperative margin assessment in patients undergoing breast-conserving surgery," Ann Surg Oncol **14**, 1458-1471 (2007).
67. T. M. Bydlon, W. T. Barry, S. A. Kennedy, J. Q. Brown, J. E. Gallagher, L. G. Wilke, J. Geradts, and N. Ramanujam, "Advancing optical imaging for breast margin assessment: an analysis of excisional time, cautery, and patent blue dye on underlying sources of contrast," PLoS One **7**, e51418 (2012).
68. E. Weinberg, C. Cox, E. Dupont, L. White, M. Ebert, H. Greenberg, N. Diaz, V. Vercel, B. Centeno, A. Cantor, and S. Nicosia, "Local recurrence in lumpectomy patients after imprint cytology margin evaluation," Am J Surg **188**, 349-354 (2004).
69. A. J. Guidi, J. L. Connolly, J. R. Harris, and S. J. Schnitt, "The relationship between shaved margin and inked margin status in breast excision specimens," Cancer **79**, 1568-1573 (1997).
70. J. M. Jorns, D. Visscher, M. Sabel, T. Breslin, P. Healy, S. Daignaut, J. L. Myers, and A. J. Wu, "Intraoperative frozen section analysis of margins in breast conserving surgery significantly decreases reoperative rates: one-year experience at an ambulatory surgical center," Am J Clin Pathol **138**, 657-669 (2012).
71. F. H. Barakat, I. Sulaiman, and M. A. Sughayer, "Reliability of frozen section in breast sentinel lymph node examination," Breast Cancer **21**, 576-582 (2014).
72. A. J. Creager, J. A. Shaw, P. R. Young, and K. R. Geisinger, "Intraoperative Evaluation of Lumpectomy Margins by Imprint Cytology With Histologic Correlation," Archives of Pathology & Laboratory Medicine **126**, 846-848 (2002).
73. E. K. Valdes, S. K. Boolbol, J. M. Cohen, and S. M. Feldman, "Intra-operative touch preparation cytology; does it have a role in re-excision lumpectomy?," Ann Surg Oncol **14**, 1045-1050 (2007).
74. H. Eggemann, T. Ignatov, A. Beni, S. D. Costa, O. Ortmann, and A. Ignatov, "Intraoperative Ultrasound in the Treatment of Breast Cancer," Geburtshilfe und Frauenheilkunde **73**, 1028-1034 (2013).
75. M. Moschetta, M. Telegrafo, T. Introna, L. Coi, L. Rella, V. Ranieri, A. Cirilli, A. S. Ianora, and G. Angelelli, "Role of specimen US for predicting resection margin status in breast conserving therapy," Il Giornale di Chirurgia **36**, 201-204 (2015).
76. M. Ramos, J. C. Díaz, T. Ramos, R. Ruano, M. Aparicio, M. Sancho, and J. M. González-Orús, "Ultrasound-guided excision combined with intraoperative assessment of gross macroscopic margins decreases the rate of reoperations for non-palpable invasive breast cancer," The Breast **22**, 520-524 (2013).
77. R. A. Graham, M. J. Homer, C. J. Sigler, H. Safaii, C. H. Schmid, D. J. Marchant, and T. J. Smith, "The efficacy of specimen radiography in evaluating the surgical margins of impalpable breast carcinoma," American Journal of Roentgenology **162**, 33-36 (1994).
78. W. P. Weber, S. Engelberger, C. T. Viehl, R. Zanetti-Dallenbach, S. Kuster, S. Dirnhofer, D. Wruk, D. Oertli, and W. R. Marti, "Accuracy of frozen section analysis versus specimen radiography during breast-conserving surgery for nonpalpable lesions," World J Surg **32**, 2599-2606 (2008).
79. M. Thill, K. Baumann, and J. Barinoff, "Intraoperative assessment of margins in breast conservative surgery--still in use?," J Surg Oncol **110**, 15-20 (2014).
80. S. A. Boppart, J. Q. Brown, C. S. Farah, E. Kho, L. Marcu, C. M. Saunders, and H. Sterenborg, "Label-free optical imaging technologies for rapid translation and use during intraoperative surgical and tumor margin assessment," J Biomed Opt **23**, 1-10 (2017).
81. Y. Chen, W. Xie, A. K. Glaser, N. P. Reder, C. Mao, S. M. Dintzis, J. C. Vaughan, and J. T. C. Liu, "Rapid pathology of lumpectomy margins with open-top light-sheet (OTLS) microscopy," Biomedical Optics Express **10**, 1257-1272 (2019).
82. R. H. Webb, "Confocal optical microscopy," Reports on Progress in Physics **59**, 427 (1996).
83. J. B. Pawley, *Handbook of Biological Confocal Microscopy* (Springer, 1995).

84. J. T. Liu, M. J. Mandella, J. M. Crawford, C. H. Contag, T. D. Wang, and G. S. Kino, "Efficient rejection of scattered light enables deep optical sectioning in turbid media with low-numerical-aperture optics in a dual-axis confocal architecture," Journal of biomedical optics **13**, 034020-034020-034011 (2008).
85. J. T. Liu, M. J. Mandella, S. Friedland, R. Soetikno, J. M. Crawford, C. H. Contag, G. S. Kino, and T. D. Wang, "Dual-axes confocal reflectance microscope for distinguishing colonic neoplasia," Journal of biomedical optics **11**, 054019-054019-054010 (2006).
86. L. Wei, C. Yin, and J. T. C. Liu, "Dual-Axis Confocal Microscopy for Point-of-Care Pathology," IEEE Journal of Selected Topics in Quantum Electronics **25**, 1-10 (2019).
87. D. Wang, Y. Chen, Y. Wang, and J. Liu, "Comparison of line-scanned and point-scanned dual-axis confocal microscope performance," Optics letters **38**, 5280-5283 (2013).
88. Y. Chen, D. Wang, A. Khan, Y. Wang, S. Borwege, N. Sanai, and J. T. Liu, "Video-rate in vivo fluorescence imaging with a line-scanned dual-axis confocal microscope," Journal of biomedical optics **20**, 106011-106011 (2015).
89. P. J. Dwyer, C. A. DiMarzio, and M. Rajadhyaksha, "Confocal theta line-scanning microscope for imaging human tissues," Applied optics **46**, 1843-1851 (2007).
90. B. Simon and C. A. DiMarzio, "Simulation of a theta line-scanning confocal microscope," Journal of biomedical optics **12**, 064020-064020-064029 (2007).
91. Y. Chen and J. T. Liu, "Optimizing the performance of dual-axis confocal microscopes via Monte-Carlo scattering simulations and diffraction theory," J Biomed Opt **18**, 066006 (2013).
92. Y. Chen, D. Wang, and J. T. Liu, "Assessing the tissue-imaging performance of confocal microscope architectures via Monte Carlo simulations," Opt Lett **37**, 4495-4497 (2012).
93. L. G. Henyey and J. L. Greenstein, "Diffuse radiation in the galaxy," The Astrophysical Journal **93**, 70-83 (1941).
94. W.-F. Cheong, S. A. Prahl, and A. J. Welch, "A review of the optical properties of biological tissues," IEEE journal of quantum electronics **26**, 2166-2185 (1990).
95. D. Wang, Y. Chen, and J. T. Liu, "A liquid optical phantom with tissue-like heterogeneities for confocal microscopy," Biomed Opt Express **3**, 3153-3160 (2012).
96. J. T. Liu, M. J. Mandella, N. O. Loewke, H. Haeberle, H. Ra, W. Piyawattanametha, O. Solgaard, G. S. Kino, and C. H. Contag, "Micromirror-scanned dual-axis confocal microscope utilizing a gradient-index relay lens for image guidance during brain surgery," J Biomed Opt **15**, 026029 (2010).
97. K. Carlson, M. Chidley, K. B. Sung, M. Descour, A. Gillenwater, M. Follen, and R. Richards-Kortum, "In vivo fiber-optic confocal reflectance microscope with an injection-molded plastic miniature objective lens," Appl Opt **44**, 1792-1797 (2005).
98. R. T. Kester, T. S. Tkaczyk, M. R. Descour, T. Christenson, and R. Richards-Kortum, "High numerical aperture microendoscope objective for a fiber confocal reflectance microscope," Opt Express **15**, 2409-2420 (2007).
99. M. Kyrish and T. S. Tkaczyk, "Achromatized endomicroscope objective for optical biopsy," Biomed Opt Express **4**, 287-297 (2013).
100. B. H. Zinselmeyer, J. N. Lynch, X. Zhang, T. Aoshi, and M. J. Miller, "Video-rate two-photon imaging of mouse footpad - a promising model for studying leukocyte recruitment dynamics during inflammation," Inflamm Res **57**, 93-96 (2008).
101. M. Akiba and K. P. Chan, "In vivo video-rate cellular-level full-field optical coherence tomography," J Biomed Opt **12**, 064024 (2007).
102. I. Veilleux, J. A. Spencer, D. P. Biss, D. Cote, and C. P. Lin, "In Vivo Cell Tracking With Video Rate Multimodality Laser Scanning Microscopy," IEEE Journal of Selected Topics in Quantum Electronics **14**, 10-18 (2008).
103. C. Halin, J. R. Mora, C. Sumen, and U. H. von Andrian, "In vivo imaging of lymphocyte trafficking," Annu Rev Cell Dev Biol **21**, 581-603 (2005).
104. M. Rajadhyaksha, R. R. Anderson, and R. H. Webb, "Video-rate confocal scanning laser microscope for imaging human tissues in vivo," Appl Opt **38**, 2105-2115 (1999).
105. C. L. Arrasmith, D. L. Dickensheets, and A. Mahadevan-Jansen, "MEMS-based handheld confocal microscope for in-vivo skin imaging," Opt Express **18**, 3805-3819 (2010).
106. K. Loewke, D. Camarillo, W. Piyawattanametha, D. Breeden, and K. Salisbury, *Real-time image mosaicing with a hand-held dual-axes confocal microscope*, SPIE BiOS (SPIE, 2008), Vol. 6851.

107. R. Kiesslich, J. Burg, M. Vieth, J. Gnaendiger, M. Enders, P. Delaney, A. Polglase, W. McLaren, D. Janell, S. Thomas, B. Nafe, P. R. Galle, and M. F. Neurath, "Confocal laser endoscopy for diagnosing intraepithelial neoplasias and colorectal cancer in vivo," Gastroenterology **127**, 706-713 (2004).
108. D. Wang, D. Meza, Y. Wang, L. Gao, and J. T. Liu, "Sheet-scanned dual-axis confocal microscopy using Richardson-Lucy deconvolution," Opt Lett **39**, 5431-5434 (2014).
109. M. C. Zhong, X. B. Wei, J. H. Zhou, Z. Q. Wang, and Y. M. Li, "Trapping red blood cells in living animals using optical tweezers," Nat Commun **4**, 1768 (2013).
110. N. Sanai, L. A. Snyder, N. J. Honea, S. W. Coons, J. M. Eschbacher, K. A. Smith, and R. F. Spetzler, "Intraoperative confocal microscopy in the visualization of 5-aminolevulinic acid fluorescence in low-grade gliomas," J Neurosurg **115**, 740-748 (2011).
111. J. T. Liu, D. Meza, and N. Sanai, "Trends in fluorescence image-guided surgery for gliomas," Neurosurgery **75**, 61-71 (2014).
112. N. Sanai, J. Eschbacher, G. Hattendorf, S. W. Coons, M. C. Preul, K. A. Smith, P. Nakaji, and R. F. Spetzler, "Intraoperative confocal microscopy for brain tumors: a feasibility analysis in humans," Neurosurgery **68**, 282-290; discussion 290 (2011).
113. C. Yin, A. K. Glaser, S. Y. Leigh, Y. Chen, L. Wei, P. C. Pillai, M. C. Rosenberg, S. Abeytunge, G. Peterson, C. Glazowski, N. Sanai, M. J. Mandella, M. Rajadhyaksha, and J. T. Liu, "Miniature in vivo MEMS-based line-scanned dual-axis confocal microscope for point-of-care pathology," Biomed Opt Express **7**, 251-263 (2016).
114. L. Wei, C. Yin, Y. Fujita, N. Sanai, and J. T. C. Liu, "Handheld line-scanned dual-axis confocal microscope with pistoned MEMS actuation for flat-field fluorescence imaging," Opt Lett **44**, 671-674 (2019).
115. O. Brzobohaty, T. Cizmar, and P. Zemanek, "High quality quasi-Bessel beam generated by round-tip axicon," Opt Express **16**, 12688-12700 (2008).
116. N. Chattrapiban, E. A. Rogers, D. Cofield, I. I. I. W. T. Hill, and R. Roy, "Generation of nondiffracting Bessel beams by use of a spatial light modulator," Optics Letters **28**, 2183-2185 (2003).
117. V. V. Kotlyar, A. A. Kovalev, R. V. Skidanov, O. Y. Moiseev, and V. A. Soifer, "Diffraction of a finite-radius plane wave and a Gaussian beam by a helical axicon and a spiral phase plate," J. Opt. Soc. Am. A **24**, 1955-1964 (2007).
118. J. Durnin, J. J. Miceli, Jr., and J. H. Eberly, "Comparison of Bessel and Gaussian beams," Opt Lett **13**, 79 (1988).
119. Y. Lin, W. Seka, J. Eberly, H. Huang, and D. Brown, "Experimental investigation of Bessel beam characteristics," Applied optics **31**, 2708-2713 (1992).
120. R. Arimoto, C. Saloma, T. Tanaka, and S. Kawata, "Imaging properties of axicon in a scanning optical system," Appl Opt **31**, 6653-6657 (1992).
121. L. Gao, L. Shao, C. D. Higgins, J. S. Poulton, M. Peifer, M. W. Davidson, X. Wu, B. Goldstein, and E. Betzig, "Noninvasive imaging beyond the diffraction limit of 3D dynamics in thickly fluorescent specimens," Cell **151**, 1370-1385 (2012).
122. E. Baumgart and U. Kubitscheck, "Scanned light sheet microscopy with confocal slit detection," Opt Express **20**, 21805-21814 (2012).
123. F. O. Fahrbach and A. Rohrbach, "A line scanned light-sheet microscope with phase shaped self-reconstructing beams," Opt Express **18**, 24229-24244 (2010).
124. P. Piksarv, D. Marti, T. Le, A. Unterhuber, L. H. Forbes, M. R. Andrews, A. Stingl, W. Drexler, P. E. Andersen, and K. Dholakia, "Integrated single- and two-photon light sheet microscopy using accelerating beams," Sci Rep **7**, 1435 (2017).
125. F. O. Fahrbach, V. Gurchenkov, K. Alessandri, P. Nassoy, and A. Rohrbach, "Light-sheet microscopy in thick media using scanned Bessel beams and two-photon fluorescence excitation," Opt. Express **21**, 13824-13839 (2013).
126. L. Gao, L. Shao, B.-C. Chen, and E. Betzig, "3D live fluorescence imaging of cellular dynamics using Bessel beam plane illumination microscopy," Nature Protocols **9**, 1083 (2014).
127. S. Y. Leigh, Y. Chen, and J. T. Liu, "Modulated-alignment dual-axis (MAD) confocal microscopy for deep optical sectioning in tissues," Biomedical optics express **5**, 1709-1720 (2014).
128. S. Y. Leigh, Y. Chen, and J. T. C. Liu, "Modulated-Alignment Dual-Axis (MAD) Confocal Microscopy Optimized for Speed and Contrast," IEEE Transactions on Biomedical Engineering **63**, 2119-2124 (2016).
129. A. K. Glaser, Y. Chen, and J. T. Liu, "Fractal propagation method enables realistic optical microscopy simulations in biological tissues," Optica **3**, 861-869 (2016).
130. R. L. Siegel, K. D. Miller, and A. Jemal, "Cancer statistics, 2018," CA Cancer J Clin **68**, 7-30 (2018).

131. L. Huo, "A practical approach to grossing breast specimens," Ann Diagn Pathol **15**, 291-301 (2011).
132. J. C. Cendan, D. Coco, and E. M. Copeland, 3rd, "Accuracy of intraoperative frozen-section analysis of breast cancer lumpectomy-bed margins," J Am Coll Surg **201**, 194-198 (2005).
133. T. Osako, R. Nishimura, Y. Nishiyama, Y. Okumura, R. Tashima, M. Nakano, M. Fujisue, Y. Toyozumi, and N. Arima, "Efficacy of intraoperative entire-circumferential frozen section analysis of lumpectomy margins during breast-conserving surgery for breast cancer," Int J Clin Oncol **20**, 1093-1101 (2015).
134. S. J. Schnitt and M. Morrow, "Should intraoperative frozen section evaluation of breast lumpectomy margins become routine practice?," Am J Clin Pathol **138**, 635-638 (2012).
135. H. Jaafar, "Intra-operative frozen section consultation: concepts, applications and limitations," The Malaysian journal of medical sciences : MJMS **13**, 4-12 (2006).
136. T. T. W. Wong, R. Zhang, P. Hai, C. Zhang, M. A. Pleitez, R. L. Aft, D. V. Novack, and L. V. Wang, "Fast label-free multilayered histology-like imaging of human breast cancer by photoacoustic microscopy," Science Advances **3**(2017).
137. D. M. McClatchy, B. W. Maloney, E. J. Rizzo, K. D. Paulsen, W. A. Wells, and B. W. Pogue, "Spatial and Spectral Analysis of in-Situ Tumor-Normal Interfaces in Freshly Resected Lumpectomy Slices using Multispectral Structured Light Imaging," in *Biophotonics Congress: Biomedical Optics Congress 2018 (Microscopy/Translational/Brain/OTS)*, OSA Technical Digest (Optical Society of America, 2018), CTu4B.3.
138. R. Levenson, F. Fereidouni, Z. Harmany, A. Todd, L. Brandi, and S. Demos, "Microscopy with UV Surface Excitation (MUSE): Rapid, Simple, Slide-Free Histology," in *Optics in the Life Sciences Congress*, OSA Technical Digest (online) (Optical Society of America, 2017), NW3C.5.
139. R. Levenson and F. Fereidouni, "MUSE: A New, Fast, Simple Microscopy Method for Slide-Free Histology and Surface Topography," in *The FASEB Journal*, (2016).
140. F. Fereidouni, A. D. Mitra, S. Demos, and R. Levenson, "Microscopy with UV Surface Excitation (MUSE) for slide-free histology and pathology imaging," in *SPIE BiOS*, (SPIE, 2015), 6.
141. Y. Wang, S. Kang, A. Khan, G. Ruttner, S. Y. Leigh, M. Murray, S. Abeytunge, G. Peterson, M. Rajadhyaksha, S. Dintzis, S. Javid, and J. T. Liu, "Quantitative molecular phenotyping with topically applied SERS nanoparticles for intraoperative guidance of breast cancer lumpectomy," Sci Rep **6**, 21242 (2016).
142. S. C. Davis, S. L. Gibbs, J. R. Gunn, and B. W. Pogue, "Topical dual-stain difference imaging for rapid intra-operative tumor identification in fresh specimens," Opt Lett **38**, 5184-5187 (2013).
143. S. Kang, Y. W. Wang, X. Xu, E. Navarro, K. M. Tichauer, and J. T. C. Liu, "Microscopic investigation of" topically applied nanoparticles for molecular imaging of fresh tissue surfaces," J Biophotonics **11**, e201700246 (2018).
144. Y. W. Wang, N. P. Reder, S. Kang, A. K. Glaser, Q. Yang, M. A. Wall, S. H. Javid, S. M. Dintzis, and J. T. C. Liu, "Raman-Encoded Molecular Imaging with Topically Applied SERS Nanoparticles for Intraoperative Guidance of Lumpectomy," Cancer Res **77**, 4506-4516 (2017).
145. V. Krishnaswamy, A. M. Laughney, K. D. Paulsen, and B. W. Pogue, "Dark-field scanning in situ spectroscopy platform for broadband imaging of resected tissue," Opt Lett **36**, 1911-1913 (2011).
146. A. M. Laughney, V. Krishnaswamy, E. J. Rizzo, M. C. Schwab, R. J. Barth, B. W. Pogue, K. D. Paulsen, and W. A. Wells, "Scatter spectroscopic imaging distinguishes between breast pathologies in tissues relevant to surgical margin assessment," Clin Cancer Res **18**, 6315-6325 (2012).
147. J. Skoch, A. Dunn, B. T. Hyman, and B. J. Bacskai, "Development of an optical approach for noninvasive imaging of Alzheimer's disease pathology," J Biomed Opt **10**, 11007 (2005).
148. V. Venugopal, M. Park, Y. Ashitate, F. Neacsu, F. Kettenring, J. V. Frangioni, S. P. Gangadharan, and S. Gioux, "Design and characterization of an optimized simultaneous color and near-infrared fluorescence rigid endoscopic imaging system," J Biomed Opt **18**, 126018 (2013).
149. H. Inoue, S.-e. Kudo, and A. Shiokawa, "Technology Insight: laser-scanning confocal microscopy and endocytoscopy for cellular observation of the gastrointestinal tract," Nature Clinical Practice Gastroenterology &Amp; Hepatology **2**, 31 (2005).
150. L. C. Cahill, M. G. Giacomelli, T. Yoshitake, H. Vardeh, B. E. Faulkner-Jones, J. L. Connolly, C.-K. Sun, and J. G. Fujimoto, "Rapid virtual hematoxylin and eosin histology of breast tissue specimens using a compact fluorescence nonlinear microscope," Laboratory Investigation **98**, 150 (2017).
151. E. S. Flores, M. Cordova, K. Kose, W. Phillips, A. Rossi, K. Nehal, and M. Rajadhyaksha, "Intraoperative imaging during Mohs surgery with reflectance confocal microscopy: initial clinical experience," Journal of biomedical optics **20**, 061103-061103 (2015).

152. S. Abeytunge, Y. Li, B. Larson, G. Peterson, E. Seltzer, R. Toledo-Crow, and M. Rajadhyaksha, "Confocal microscopy with strip mosaicing for rapid imaging over large areas of excised tissue," Journal of biomedical optics **18**, 061227-061227 (2013).
153. S. Abeytunge, Y. Li, B. Larson, R. Toledo-Crow, and M. Rajadhyaksha, "Rapid confocal imaging of large areas of excised tissue with strip mosaicing," Journal of Biomedical Optics **16**, 050504 (2011).
154. S. Abeytunge, B. Larson, G. Peterson, M. Morrow, M. Rajadhyaksha, and M. P. Murray, "Evaluation of breast tissue with confocal strip-mosaicking microscopy: a test approach emulating pathology-like examination," J Biomed Opt **22**, 34002 (2017).
155. A. K. Glaser, Y. Wang, and J. T. Liu, "Assessing the imaging performance of light sheet microscopies in highly scattering tissues," Biomed Opt Express **7**, 454-466 (2016).
156. J. Huisken, J. Swoger, F. Del Bene, J. Wittbrodt, and E. H. K. Stelzer, "Optical Sectioning Deep Inside Live Embryos by Selective Plane Illumination Microscopy," Science **305**, 1007-1009 (2004).
157. K. Greger, J. Swoger, and E. H. K. Stelzer, "Basic building units and properties of a fluorescence single plane illumination microscope," Review of Scientific Instruments **78**, 023705 (2007).
158. C. J. Engelbrecht, K. Greger, E. G. Reynaud, U. Kržic, J. Colombelli, and E. H. K. Stelzer, "Three-dimensional laser microsurgery in light-sheet based microscopy (SPIM)," Opt. Express **15**, 6420-6430 (2007).
159. J. Huisken and D. Y. R. Stainier, "Selective plane illumination microscopy techniques in developmental biology," Development **136**, 1963-1975 (2009).
160. R. McGorty, H. Liu, D. Kamiyama, Z. Dong, S. Guo, and B. Huang, "Open-top selective plane illumination microscope for conventionally mounted specimens," Opt. Express **23**, 16142-16153 (2015).
161. R. M. Power and J. Huisken, "Intraoperative histology: Lightning 3D histopathology," Nature Biomedical Engineering **1**, 0101 (2017).
162. Y. Wu, A. Ghitani, R. Christensen, A. Santella, Z. Du, G. Rondeau, Z. Bao, D. Colón-Ramos, and H. Shroff, "Inverted selective plane illumination microscopy (iSPIM) enables coupled cell identity lineaging and neurodevelopmental imaging in Caenorhabditis elegans," Proceedings of the National Academy of Sciences **108**, 17708-17713 (2011).
163. P. Strnad, S. Gunther, J. Reichmann, U. Krzic, B. Balazs, G. de Medeiros, N. Norlin, T. Hiiragi, L. Hufnagel, and J. Ellenberg, "Inverted light-sheet microscope for imaging mouse pre-implantation development," Nature methods **13**, 139-142 (2016).
164. M. B. Bouchard, V. Voleti, C. S. Mendes, C. Lacefield, W. B. Grueber, R. S. Mann, R. M. Bruno, and E. M. Hillman, "Swept confocally-aligned planar excitation (SCAPE) microscopy for high-speed volumetric imaging of behaving organisms," Nature photonics **9**, 113-119 (2015).
165. F. Aguet, D. Van De Ville, and M. Unser, "Model-based 2.5-d deconvolution for extended depth of field in brightfield microscopy," IEEE Trans Image Process **17**, 1144-1153 (2008).
166. M. G. Giacomelli, L. Husvogt, H. Vardeh, B. E. Faulkner-Jones, J. Hornegger, J. L. Connolly, and J. G. Fujimoto, "Virtual Hematoxylin and Eosin Transillumination Microscopy Using Epi-Fluorescence Imaging," PLoS One **11**, e0159337 (2016).
167. S. Preibisch, S. Saalfeld, and P. Tomancak, "Globally optimal stitching of tiled 3D microscopic image acquisitions," Bioinformatics **25**, 1463-1465 (2009).
168. K. N. Elfer, A. B. Sholl, M. Wang, D. B. Tulman, S. H. Mandava, B. R. Lee, and J. Q. Brown, "DRAQ5 and Eosin ('D&E') as an Analog to Hematoxylin and Eosin for Rapid Fluorescence Histology of Fresh Tissues," PLOS ONE **11**, e0165530 (2016).
169. R. S. Tuma, M. P. Beaudet, X. Jin, L. J. Jones, C. Y. Cheung, S. Yue, and V. L. Singer, "Characterization of SYBR Gold nucleic acid gel stain: a dye optimized for use with 300-nm ultraviolet transilluminators," Anal Biochem **268**, 278-288 (1999).
170. G. T. Hermanson, *Bioconjugate techniques* (Academic Press, San Diego, 1996).
171. Y. W. Wang, A. Khan, M. Som, D. Wang, Y. Chen, S. Y. Leigh, D. Meza, P. Z. McVeigh, B. C. Wilson, and J. T. Liu, "Rapid ratiometric biomarker detection with topically applied SERS nanoparticles," Technology (Singap World Sci) **2**, 118-132 (2014).
172. Y. Wang, S. Kang, J. D. Doerksen, A. K. Glaser, and J. T. Liu, "Surgical Guidance via Multiplexed Molecular Imaging of Fresh Tissues Labeled with SERS-Coded Nanoparticles," IEEE J Sel Top Quantum Electron **22**(2016).
173. Y. W. Wang, J. D. Doerksen, S. Kang, D. Walsh, Q. Yang, D. Hong, and J. T. Liu, "Multiplexed Molecular Imaging of Fresh Tissue Surfaces Enabled by Convection-Enhanced Topical Staining with SERS-Coded Nanoparticles," Small **12**, 5612-5621 (2016).

174. D. Wang, Y. Chen, S. Y. Leigh, H. Haeberle, C. H. Contag, and J. T. Liu, "Microscopic Delineation of Medulloblastoma Margins in a Transgenic Mouse Model Using a Topically Applied VEGFR-1 Probe," Transl Oncol **5**, 408-414 (2012).
175. S. Petroni, L. Caldarola, R. Scamarcio, F. Giotta, A. Latorre, A. Mangia, and G. Simone, "FISH testing of HER2 immunohistochemistry 1+ invasive breast cancer with unfavorable characteristics," Oncol Lett **12**, 3115-3122 (2016).
176. T. W. Jacobs, A. M. Gown, H. Yaziji, M. J. Barnes, and S. J. Schnitt, "Comparison of Fluorescence In Situ Hybridization and Immunohistochemistry for the Evaluation of HER-2/neu in Breast Cancer," **17**, 1974-1974 (1999).
177. D. Zhang, I. Capoglu, Y. Li, L. Cherkezyan, J. Chandler, G. Spicer, H. Subramanian, A. Taflove, and V. Backman, "Finite-difference time-domain-based optical microscopy simulation of dispersive media facilitates the development of optical imaging techniques," Journal of biomedical optics **21**, 65004-65004 (2016).
178. C. Liu, L. Bi, R. L. Panetta, P. Yang, and M. A. Yurkin, "Comparison between the pseudo-spectral time domain method and the discrete dipole approximation for light scattering simulations," Opt. Express **20**, 16763-16776 (2012).
179. B. Wang, J. E. Nevins, Z. Nadler, G. Wollstein, H. Ishikawa, R. A. Bilonick, L. Kagemann, I. A. Sigal, I. Grulkowski, J. J. Liu, M. Kraus, C. D. Lu, J. Hornegger, J. G. Fujimoto, and J. S. Schuman, "Reproducibility of in-vivo OCT measured three-dimensional human lamina cribrosa microarchitecture," PLoS One **9**, e95526 (2014).
180. V. Magidson and A. Khodjakov, "Circumventing photodamage in live-cell microscopy," Methods in cell biology **114**, 545-560 (2013).
181. R. K. Benninger and D. W. Piston, "Two-photon excitation microscopy for the study of living cells and tissues," Curr Protoc Cell Biol **Chapter 4**, Unit 4 11 11-24 (2013).
182. D. Lorenser, C. Christian Singe, A. Curatolo, and D. D. Sampson, "Energy-efficient low-Fresnel-number Bessel beams and their application in optical coherence tomography," Opt Lett **39**, 548-551 (2014).
183. K. Maslov, H. F. Zhang, S. Hu, and L. V. Wang, "Optical-resolution photoacoustic microscopy for in vivo imaging of single capillaries," Opt Lett **33**, 929-931 (2008).
184. A. Curatolo, M. Villiger, D. Lorenser, P. Wijesinghe, A. Fritz, B. F. Kennedy, and D. D. Sampson, "Ultrahigh-resolution optical coherence elastography," Opt Lett **41**, 21-24 (2016).
185. K. Wang, W. Sun, C. T. Richie, B. K. Harvey, E. Betzig, and N. Ji, "Direct wavefront sensing for high-resolution in vivo imaging in scattering tissue," Nat Commun **6**, 7276 (2015).
186. J. H. Park, W. Sun, and M. Cui, "High-resolution in vivo imaging of mouse brain through the intact skull," Proc Natl Acad Sci U S A **112**, 9236-9241 (2015).
187. B. Balazs, J. Deschamps, M. Albert, J. Ries, and L. Hufnagel, "A real-time compression library for microscopy images," 164624 (2017).

PUBLICATIONS

1. **Y. Chen**, W. Xie, A.K. Glaser, N.P. Reder, C. Mao, S.M. Dintzis, J.C. Vaughan, and J.T.C. Liu, "Rapid pathology of lumpectomy margins with open-top light-sheet (OTLS) microscopy," *Biomedical Optics Express* 10, 1257 (2019).
2. W. Xie, **Y. Chen**, Y. Wang, L. Wei, C. Yin, A.K. Glaser, M.E. Fauver, E.J. Seibel, S.M. Dintzis, J.C. Vaughan, N.P. Reder and J.T.C. Liu, "Microscopy with ultraviolet surface excitation for wide-area pathology of breast surgical margins," *Journal of Biomedical Optics* 24, 026501 (2019).
3. A.K. Glaser, **Y. Chen**, C. Yin, L. Wei, L.A. Barner, N.P. Reder, and J.T.C. Liu, "Multidirectional digital scanned light-sheet microscopy enables uniform fluorescence excitation and contrast-enhanced imaging," *Scientific Reports* 8, 13878 (2018).
4. A.K. Glaser, N. Reder, **Y. Chen**, E. McCarty, C. Yin, P. Wei, Y. Wang, L. True and J.T.C. Liu, "Panoramic light-sheet microscopy for slide-free non-destructive 3D pathology of human clinical specimens," *Nature Biomedical Engineering* 1, 0084 (2017).
5. L. Wei, **Y. Chen**, C. Yin, S. Borwege, N. Sanai, and J.T.C. Liu, "Optical-sectioning microscopy of protoporphyrin IX fluorescence in human gliomas: standardization and quantitative comparison with histology," *Journal of Biomedical Optics* 22, 046005 (2017).
6. **Y. Chen**, A.K. Glaser and J.T.C. Liu, "Bessel-beam illumination in dual-axis confocal microscopy mitigates resolution degradation caused by refractive heterogeneities," *Journal of Biophotonics* 10, 68(2017).
7. A. Glaser, **Y. Chen**, and J.T.C. Liu, "Fractal propagation method enables realistic optical microscopy simulations in biological tissues," *Optica* 3, 861 (2016).
8. C. Yin, A.K. Glaser, S.Y. Leigh, **Y. Chen**, Linpeng Wei, P.C.S. Pillai, M. Rosenberg, S. Abeytunge, G. Peterson, C. Glazowski, M.J. Mandella, M. Rajadhyaksha, and J.T.C. Liu, "A miniature *in vivo* MEMS-based line-scanned dual-axis confocal microscope for point-of-care pathology," *Biomedical Optics Express* 7, 251 (2016).
9. S.Y. Leigh, **Y. Chen**, and J.T.C. Liu, "Modulated-alignment dual-axis (MAD) confocal microscopy optimized for speed and contrast," *IEEE Transactions on Biomedical Engineering* 63, 2119 (2016).

10. **Y. Chen**, D. Wang, A. Khan, Y. Wang, S. Borwege, N. Sanai and J.T.C. Liu, "Video-rate *in vivo* fluorescence imaging with a line-scanned dual-axis confocal microscope," *Journal of Biomedical Optics* 20, 106011 (2015).
11. **Y. Chen** and J.T.C. Liu, "Characterizing the beam steering and distortion of Gaussian and Bessel beams focused in tissues with microscopic heterogeneities," *Biomedical Optics Express* 6, 1318 (2015).
12. Y. Wang, A. Khan, S.Y. Leigh, D. Wang, **Y. Chen**, D. Meza, and J.T.C. Liu, "Comprehensive spectral endoscopy of topically applied SERS nanoparticles in the rat esophagus," *Biomedical Optics Express* 5, 2883 (2014).
13. S.Y. Leigh, **Y. Chen**, and J.T.C. Liu, "Modulated-alignment dual-axis (MAD) confocal microscopy for deep optical sectioning in tissues," *Biomedical Optics Express* 5, 1709 (2014).
14. Y. Wang, A. Khan, M. Som; D. Wang, **Y. Chen**, S.Y. Leigh, D. Meza; P.Z. McVeigh, B.C. Wilson, and J.T.C. Liu, "Rapid ratiometric biomarker detection with topically applied SERS nanoparticles," *Technology* 2, 1-15 (2014).
15. D. Wang, **Y. Chen**, Y. Wang, and J.T.C. Liu, "Comparison of line-scanned and point-scanned dual-axis confocal (DAC) microscope performance," *Optics Letters* 38, 5280-5283 (2013).
16. **Y. Chen** and J.T.C. Liu, "Optimizing the performance of dual-axis confocal microscopes via Monte-Carlo scattering simulations and diffraction theory," *Journal of Biomedical Optics* 18, 066006 (2013).
17. D. Wang, **Y. Chen**, and J.T.C. Liu, "A liquid optical phantom with tissue-like heterogeneities for confocal microscopy," *Biomedical Optics Express* 12, 3153-3160 (2012).
18. **Y. Chen**, D. Wang, and J.T.C. Liu, "Assessing the tissue-imaging performance of confocal microscope architectures via Monte-Carlo scattering simulations," *Optics Letters* 37, 4495-4497 (2012).
19. D. Wang, **Y. Chen**, S.Y. Leigh, H. Haeberle, C.H. Contag, and J.T.C. Liu, "Microscopic delineation of medulloblastoma margins in a transgenic mouse model using a topically applied VEGFR-1 probe," *Translational Oncology* 5, 408-414 (2012).